Efficacy of the distortion compensation method for Selective Laser Melting specimens

EB van Wyk

orcid.org/0000-0003-1553-6783

Dissertation accepted in fulfilment of the requirements for the degree *Master of Engineering in Mechanical Engineering* at the Northwest University

Supervisor:	Mr CP Kloppers
Co-supervisor:	Dr J Fourie

Graduation:	May 2022
Student number:	25027972

ACKNOWLEDG EMENTS

Firstly, I would like to thank the Collaborative Program for Additive Manufacturing (CPAM) for funding this study and providing me with financial support throughout the duration of this study. Then a special thanks to Mr CP Kloppers and Dr Jaundrie Fourie for assisting me through the study with sample preparations, arising problems during the study and overall writing. The support and understanding Mr Kloppers and Dr Fourie gave me throughout the past two years did not know any bounds. There are people in one's life that will go as quickly as they came and some that will change your life forever by shaping new ideas and changing ideologies for the better.

Then I would like to thank the kind and hardworking employees of Rectecon word for the experimental data measurements of all the calibration and complex geometry used in this study. I would also like to thank the NWU for all the assistance, energy, and guidance throughout this study and the opportunities they create for young creative minds in south Africa.

I would like to thank my parents for every opportunity they gave me and the support throughout my life that led up to this point. Without their understanding, support, and encouragement, this study would not have been possible.

Lastly, I would like to thank Cheree du Plessis for all the emotional support and motivation throughout this time period, who was always willing to listen to the ideas and development of this study. I will always be grateful for your support, care and love.

ABSTRACT

As industry 4.0 has gained momentum, the need for accurate, fast, and customizable component prototyping and fabrication has risen drastically. Additive manufacturing provides the freedom and capability to fabricate complex and multipurpose components for various applications ranging from aerospace to dental applications. This manufacturing methods' basic principle is fabricating a component by adding material in layers and selectively melting the powder in a layer-by-layer fashion to complete the component. Additive manufacturing is known to induce thermal stress in the part as the component is repeatedly heated and cooled, leading to defects forming in the component. One of the most frequent defects resulting from thermal stress in additive manufacturing is the deformation of the component. In some instances, the deformation can occur to such an extent that the part will be rendered unusable due to dimensional inaccuracies and resulting in a loss of resources and time.

The use of calibrated software and hardware utilized to fabricate additive manufactured components makes it possible to calculate, predict, and compensate for any deformation the component will undergo during and after the fabrication process. This study aims to evaluate the efficacy of the distortion compensation method on selective laser melted specimens.

This distortion compensation method is implemented to alter the geometry of the designed component to minimize the deformation of the part. This study consists of three phases, which is essential for successfully implementing the distortion compensation method. The first is the calibration phase, which aims to calculate the corresponding Eigen strain tensor values that will enable the software to predict any deformation that can occur during and after fabrication. After which follows a validation phase to validate the calculated Eigen strain values that resulted from the calibration phase, ensuring the deformation predicted in the simulation correlates with the actual deformation of the part. Lastly, the distortion compensation phase will investigate the efficacy and accuracy of this method to decrease the distortion of components.

The findings of this study show a clear and accurate correlation between the theoretical and practical deformation of the samples. A predicted deformation tolerance accuracy of <2% during the simulation phase can be achieved by calibrating the software and hardware. As the distortion compensation algorithm is applied to the geometries, the predicted deformation accuracy decreases to a tolerance of $< 6\%$. Although the predicted deformation accuracy of the geometry subjected to the distortion compensation method is lower than the non-distortion compensated geometry, the overall total deformation of the geometry was still decreased by $< 4\%$. Thus, the

method of distortion compensation is a promising tool to decrease the distortion of additively manufactured parts.

Keywords

Additive manufacturing, Cobalt Chrome, deformation compensation, deformation prediction, finite element method, inherent strain method, metal additive manufacturing, powder bed fusion, residual stress calculation, Simufact additive

TABLE OF CONTENTS

LIST OF TABLES

LIST OF FIGURES

LIST OF EQUATIONS

LIST OF ABBREVIATIONS

A	
AAS	ANSYS additive suite
AM	Additive manufacturing
C	
CAD	Computer-aided design
CMM	Coordinate measuring machine
CoCr	Cobalt Chrome
D	
DCS	Double cantilever simulation
DED	Direct energy deposition
DMLS	Direct metal laser sintering
EBM	
EBM	Electron beam melting
F	
FDM	Fused deposition modelling
FE	Finite element
FEM	Finite element method
H	
HAZ	Heat affected zone
I	
ISM	Inherent strain method
L	
LBM	Laser beam melting
M	
MAM	Metal additive manufacturing
O	
OC	Orlas Creator
ODC	Orthotropic double cantilever
OSC	Orthotropic single cantilever
P	
PBF	Powder bed fusion
PFF	Powder feed fusion
R	
RPD	Removable partial denture
S	
SCS	Single cantilever simulation
SEM	Scanning electron microscopy
SL	Stereolithography
SLM	Selective laser melting
W	
WEDM	Wire electron discharge machine
WFF	Wire feed fusion

CHAPTER 1

INTRODUCTION AND BACKGROUND

1.1 Introduction and background

Over the past decade, the advancement in additive manufacturing (AM) has led to a broader range of materials and processes for AM use. The materials currently used for AM include polymers, ceramics, foams, gels, biomaterials and metals, to name but a few [1]. As useable materials increased, the development of various manufacturing processes that utilize these materials in the AM industry increased. These AM processes include binder jetting, direct energy deposition (DED), material extrusion processes, powder bed fusion (PBF), and sheet lamination [1] [2] [3].

The basic principle of AM can be described by a model that is generated using computer-aided design software (CAD), followed by the addition of material to the model in a layer upon layer fashion to fabricate a model [1]. Each layer that is created can be perceived as a cross-section of the original model that was generated using CAD software. The model information stored in the CAD file is then sliced[1] , and the g-code[2] is generated by the software that will be used by the AM machine to fabricate the model [4] [5] [6] [7].

Metal additive manufacturing (MAM) has created many opportunities in the field of manufacturing. These functional metal parts are utilized in the automobile, energy, and medical device industries. AM is widely used due to the flexibility of the process to manufacture parts with complex geometries while using functionally graded materials [8]. The PBF process involves a thin layer of feedstock material powder particles that are spread over a build plate. The height of the layers often depends on the properties of the metal powder, such as particle size distribution and shape, as well as the flowability of the material. The layer height will primarily vary between 20µm to 50µm depending on the material that is used in the PBF process [1]. The accuracy and surface quality of the component will significantly depend on the layer height that is used to fabricate the model. During fabrication, the first layer of the model is deposited onto the build plate and the next layer upon the previous, the result of the continuous stacking of layers [9] [10] [11].

Selective laser melting (SLM) and selective laser sintering (SLS) are subcategories in the PBF process. During the SLM process, a high-power density laser melts the powder particles to produce an approximation of the original part with near full density out of the feedstock material. During this process, some of these parts can have an absolute density of up to 99.5% [12]. As the high-power-density laser is highly localized, the steep heating and cooling gradient during the

[1] Slicing refers to the operation when the original CAD data is “sliced” into layers. The projection of each layer will be the cross-section at a specific height measured from the starting plane of the CAD model [16].

[2] G-code refers to the programming language used for computer numerical control (CNC) machines [81].

SLM process can produce non-uniform thermal expansion and contraction in the newly manufactured part, also known as thermal stress. The effect of thermal stress is a complicated distribution of residual stress in affected zones of the component. Residual stress could better be explained as the stress that would exist in a component if all the external loads were removed. As a result, the internal stress caused by thermal stress can lead to distortion, fatigue, and fracture of components [13].

AM is mainly used for prototyping and manufacturing custom components ranging from aerospace to dental applications. As AM is a relatively new manufacturing technology, defects and failed parts are frequently encountered. Defects such as warping, delamination, deformation and insufficient dimensional tolerance will result in failure of the component. With each failed component, the running cost of part production will exponentially increase the cost of production [9]. Failure of components and defects can potentially be prevented by using sophisticated methods such as predictive simulations. Such a method can also be implemented to effectively find parameters for the AM machine, which will yield a higher rate of component fabrication success and nullify a trial by error approach in the process.

With the use of computer software, it is possible to calculate, predict and compensate for defects such as deformation and decrease the residual stress in manufactured components [14]. By predicting and compensating for many of the defects that can occur during the AM process, the cost can significantly be decreased while improving the dimensional accuracy of the components that will be manufactured. Before any prediction and compensations can be made to increase the success rate of fabrication, the machine and simulation software must be calibrated to ensure the simulated values and the experimental values correlate with one another. By calibrating the parameters of the machine to the variables of the software, all prototyping can be done in a virtual manner saving cost on material, energy, and time.

1.2 Problem statement

In specialized fields such as engineering and medicine, the dimensional accuracy of components is of utmost importance. Due to the method of manufacturing used in AM, factors such as high thermal gradients and residual stress can potentially deform components to such an extent that the geometry of the part is no longer within the accepted dimensional tolerances. By simulating the components and using the predicted deformation results, the geometry can be altered to compensate for the distortion during manufacturing, ensuring successful components fabrication and limiting defects. With the use of the Finite element method or finite element analyses approach (FEM) and the inherent strain method (ISM), software programs can predict the resulting stress and deformation and compensate for the distortion that can occur as a result of

the fabrication method. The accuracy of predicted results should be investigated to ensure repeatable and acceptable deformation prediction and compensation.

1.2.1 Research questions

- How does the mesh size during calibration and simulation influence the predicted deformation and stress results?
- What dimensional tolerances can be achieved on an Orlas Creator?
- Does the deformation prediction correlate with experimental values?
- How will the deformation compensation influence the geometry of the component, and what tolerances are achievable using the deformation compensation functions?

1.3 Aim

This study aims to investigate the efficacy of the deformation prediction capabilities of simulation package Simufact additive and the viability of the distortion compensation method for components manufactured with Cobalt Chromium as feed stock material and the use of a PBF SLM additive process.

1.4 Objectives

The objectives to achieve the aim of this study are the following:

1.4.1 Calibration phase

The OC AM machine and the software that will be used for deformation prediction and compensation must first be calibrated to ensure that the theoretical and experimental values correlate.

1.4.2 Validation phase

To ensure that the calibrations were successful, the cantilever samples will be fabricated again at an angle of 45 degrees relative to the X-axis and Y-axis. Using the values calculated from the calibration phase, a simulation and deformation prediction will be completed on the samples printed at 45 degrees.

1.4.3 Distortion compensation phase

For the final phase, a complex geometry component will be fabricated, and a deformation prediction simulation will be completed to investigate the capability of Simufact Additive to predict the occurring deformation on a complex geometry. A deformation compensation simulation will also be completed on the complex geometry part to investigate the achievable accuracy that is possible to achieve with an OC AM machine and the use of Simufact Additive as additive manufacturing simulation software.

1.5 Research method

Figure 1-1 shows a graphical breakdown of the methodology that will be followed throughout this study to achieve the aim. The experiment will be done in three phases. The calibration phase, the validation or simulation phase, and the distortion compensation phase. During the calibration phase, two calibration cantilever beams will be fabricated parallel to the X and Y-axis, respectively. The samples will be sectioned to induce a release in residual stress that will deform the cantilevers. The deformation of each sample will then be measured with the use of a CMM machine, and the deformation measurement values will be used in the calibration phase as input data to calculate the relevant Eigen strain tensor values. The calculated Eigen strain tensor values will then be used in the validation phase of this study to predict the deformation of the calibration cantilever beams fabricated at an angle of $45°$ relative to the X and Y-axis. After fabrication, the $45°$ samples will be sectioned, and the deformation measured. The predicted deformation will then be compared to the actual deformation of the sample. Once the relevant Eigen strain tensor values are validated, the distortion compensation phase will commence. During this phase, a complex geometry will be simulated to predict the deformation that will occur and be subjected to the distortion compensation algorithm, where the geometry of the component will be altered to compensate for the distortion. The samples, which was subjected to distortion compensation and the sample that was not will then be compared to evaluate the accuracy of this method.

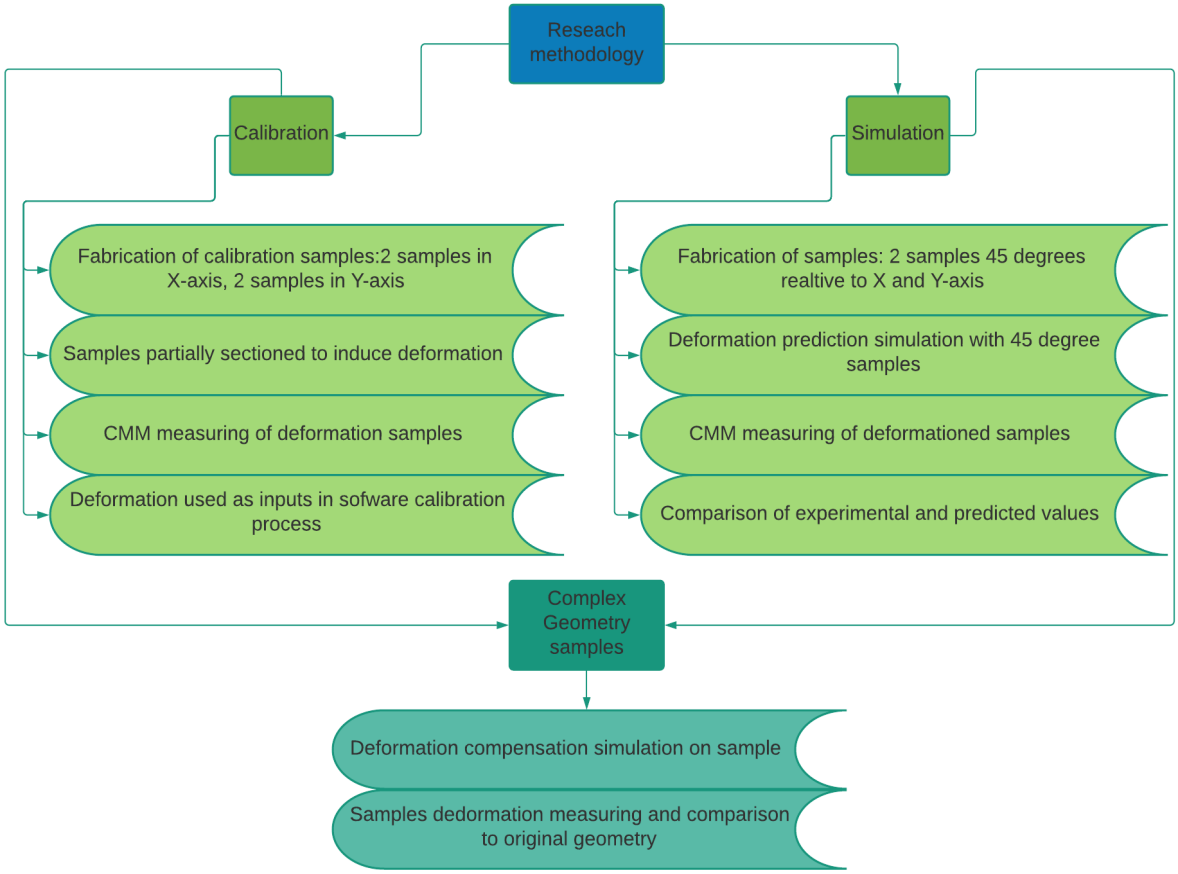

Figure 1-1-Research methodology and experiment planning

CHAPTER 2

LITERATURE REVIEW

2.1 Introduction

As the number of different processes of manufacturing increases, the need for a system to classify current and future manufacturing processes arise. Nassehi et al. [15] proposed a classification method based on the technology used in the manufacturing process. This classification divided the manufacturing process into five categories [15]. Figure 2-1 shows how each of the manufacturing technologies is divided, followed by a brief explanation of each.

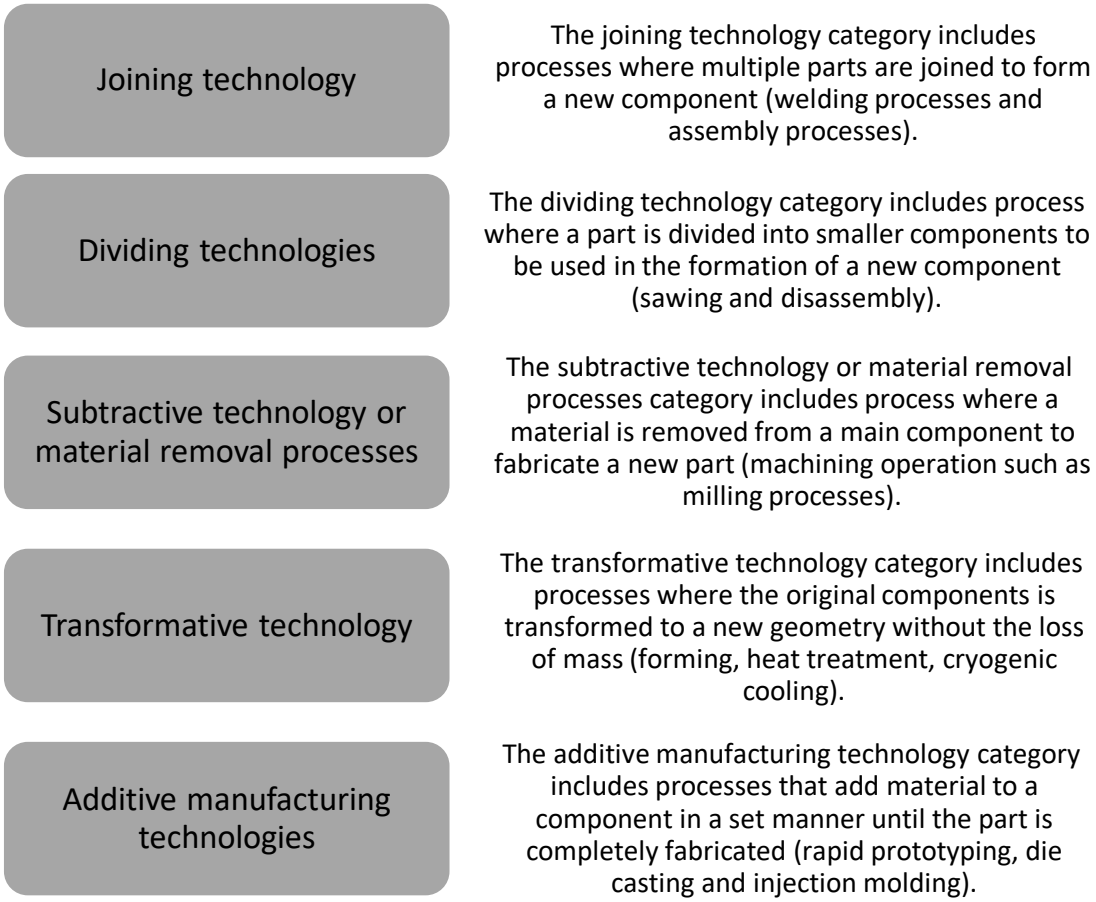

Figure 2-1-The five main categories of manufacturing technologies

2.2 Additive manufacturing.

The basic principle of AM can be described as a model that is generated using computer-aided design software (CAD). The model is then manufactured by adding material in layers [1]. The AM process begins with a component that is rendered in the selected CAD software. After the rendering is completed, the CAD data must be converted to a stereolithography (STL) file format

[16]. This STL file is then used in the slicing[3] software to generate the g-code[4] needed for the machine to follow a sequence of steps to fabricate the component. Each of the layers that are created is a cross-section, as viewed from above, of the original model that was generated using the CAD software. The layers created by the slicing software must have a finite thickness on the grounds that as the height of the layer trends to zero, the more accurate the final geometrical approximation will be to the original CAD model. This being said, there is a condition to which the system must adhere, and that is the fabrication tolerance and accuracy of the AM machine. As the material of each layer is stacked upon one another, the effect of staircasing can visibly be noticed in the model that is being fabricated [17]. This staircase effect is depicted in Figure 2-2. As the height (denoted by h) is reduced, the staircase effect will be decreased, resulting in a smoother surface and a more dimensional accurate approximation of the original CAD data.

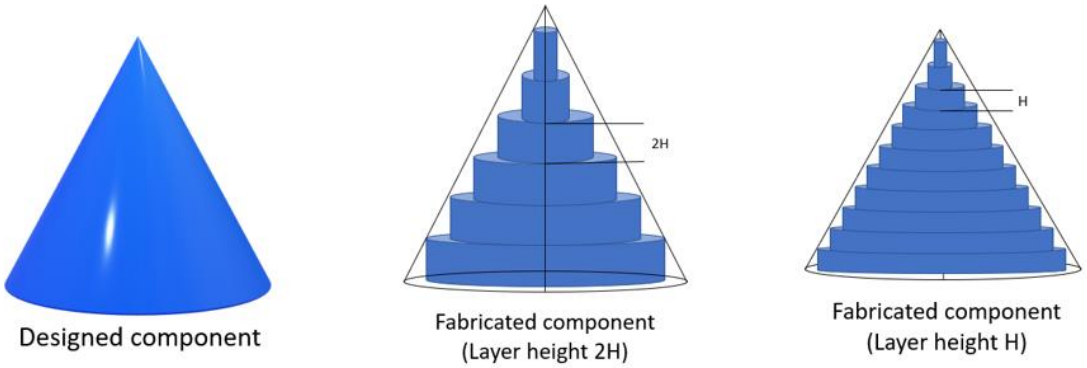

Figure 2-2-Staircase effect caused by the layering of material. Adapted from Quan et al. [18]

2.2.1 Additive manufacturing workflow.

As with all manufacturing techniques, AM must also follow a set of guidelines for the successful manufacturing of components. The AM workflow can be visualized in Figure 2-3. The first step in the AM workflow is the generation of the CAD model. After the CAD model has been generated, a multitude of software programs is available that can be used to perform various simulations on the model to determine if the component will meet the theoretical criteria of the design [19]. When the component has passed the simulation stage, the slicing software will begin to generate the g-code for the AM machine, and printing will commence. After the part is fabricated, the post-processing phase will be performed, and these include heat treatments, support removal, and

[3] Slicing refers to the operation when the original CAD data is "sliced" into layers. The projection of each layer will be the cross-section at a specific height measured from the starting plane of the CAD model.
[4] G-code is the programming language used for computer numerical control (CNC) machines[81].

polishing will be completed. The post-processing phase is the final phase before the component is completed [20].

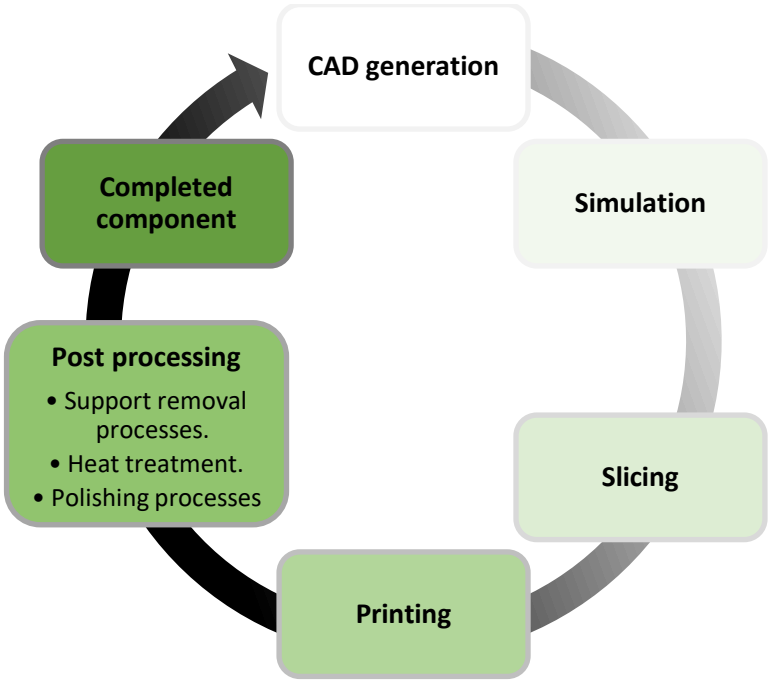

Figure 2-3-Additive manufacturing workflow

Following the flow diagram in Figure 2-3, the process starts by generating the CAD model that will be used in the fabrication process. The CAD models are designed using any number of 3-dimensional modelling software packages such as Autodesk, Siemens NX, Dassault systems Solidworks, and Simplify3D [21] [7]. These software packages enable the users to model a component in a 3-dimensional virtual space without the need for any physical resources. After the CAD design process is complete, the CAD data is used in simulations. The simulation phase of the AM workflow provides a theoretical understanding of the part during fabrication and the loading cycle of the part. In most cases, FEM is used to predict and describe how the part will be affected by the external loads, be it thermal or mechanical, or internal forces that are acting on the component. The simulation software used for the numerical computation aids in increasing the product quality, the decrease of component cost and time [22]. This will enable the designer to make any changes to the design before manufacturing has begun to ensure that no resources are lost due to design errors and verify that the component will meet the initial design requirements without physical failure of the material or component. After the CAD model is verified in the simulation software, the data file is transferred to the slicing program. In the slicing software, the CAD data is prepared and translated into a g-code that will be used by the AM machine to fabricate the part. The g-code contains all the machine data and steps that must be followed in

the manufacturing phase, such as laser paths, laser speeds and a multitude of over boundary conditions and properties.

The slicing process can be categorized into four categories as classified by Xu et al. [17]. The basic slicing method was introduced as the first slicing method used for AM. The process slices the CAD model into successive cross-sectional layers of the model with a fixed layer height. The critical parameters of basic slicing are layer direction and layer height. As the layer height is increased, the surface finish of the part will decrease. This method of slicing usually tends to give a staircase effect to the component (as seen in Figure 2-2). The adaptive slicing method is derived from basic slicing with the difference of a variable height adjustment. The layers will vary in the height regarding the surface complexity of dimensional accuracy and tolerances that is required to achieve the design specification of the component after fabrication. For some processes of AM, such as Direct Energy Deposition (DED), a non-uniform directional slicing strategy is required. To fabricate complex components which contain multiple main geometric directions, such as a branch of overhanging structures, the use of support structures become inevitable. A subcategory of slicing methods that fall under the multi-directional slicing are silhouette edge projection proposed by Singh et al. [23], transition wall method proposed by Yang et al. [24] and decomposition regrouping slicing proposed by Ding et al. [25]. Non-layer wise slinging reduces the need for support structures and improves the producibility and surface quality of complex geometric components. This method requires and employs a multitude of axes of motion at the same time.

After slicing is completed, the g-code containing the part and process data is transferred to the AM machine. The AM machine parameters such as laser intensity, scanning speed, recoater speed, powder feed rate and scanning strategy are set in the g-code but can be altered during printing on the machines user interface. The build chamber is purged of oxygen and filled with an inert gas such as nitrogen to decrease the risk of oxidation during fabrication. When the system has reached an equilibrium, the fabrication process can commence.

2.2.2 Additive manufacturing processes.

The fabrication process differs with each type of AM process used during manufacturing. These different processes can be divided into three categories, namely liquid-based, solid-based and powder-based processes [16]. The different types of AM processes are depicted in Figure 2-4. As shown, AM is first divided into a matter state process which is liquid, solid and powder-based. These categories are then divided into a specific manufacturing method which is, fabrication by melting, polymerization, and binding. Each category is then divided into the manufacturing process used to fabricate the component.

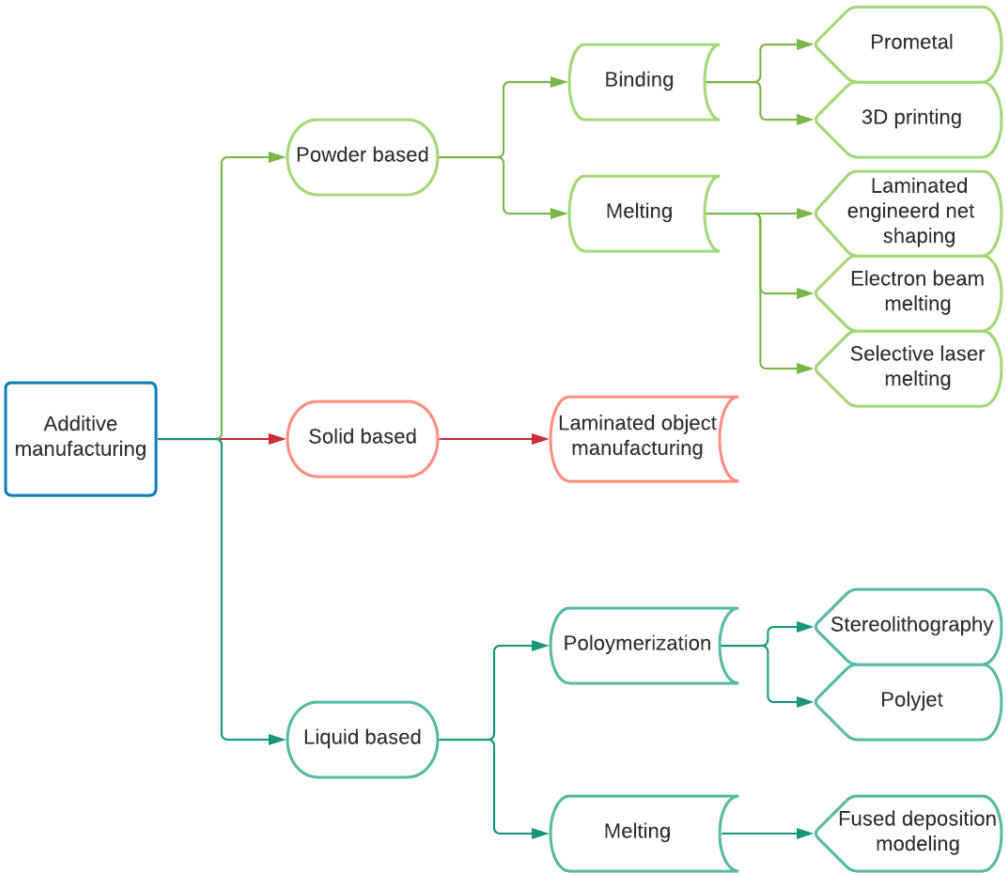

Figure 2-4-Additive manufacturing process categorisation

2.2.3 Solid based AM.

According to Mohamed et al. [26], fused deposition modelling (FDM) is one of the most popular and widely used AM technologies. This is because the process can be used for prototyping, production application and modelling. With the use of various thermoplastics, the manufacturing method can process complex geometrical parts by melting and selectively extruding the material through a nozzle while tracing the cross-sectional geometry of the part from the CAD data. After the cross-section is completed, the model is moved a set step from the nozzle, and the process is repeated, completing the model in a layered fashion [26][27]. Figure 2-5 is a representation of an FDM process where blue indicates the build material and red is an indication of the support material. The material is pushed through the heating element housing, where it is melted to a predefined viscosity and extruded through the nozzle. The support structure material can be water-soluble material to ease the support removal phase of the process, while other FDM machines will use the same material for the component and the support structures.

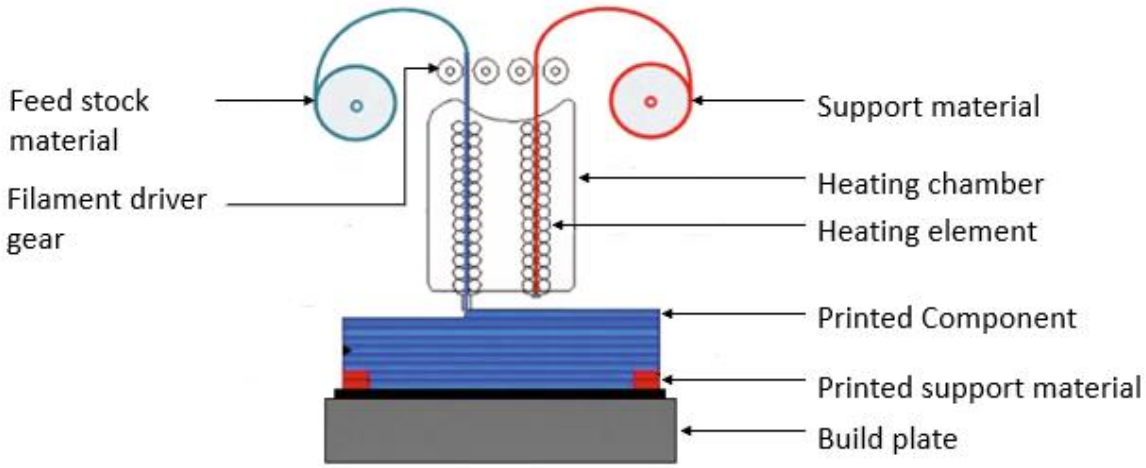

Figure 2-5-FDM Printing. Adapted from Mohamed et al. [26]

2.2.4 Liquid-based AM.

Stereolithography (SL), shown in Figure 2-6, is a liquid-based process that involves the curing and solidification of photosensitive polymers. The curing and solidification during the fabrication of a component will be initiated by an ultraviolet laser contacting the resin. The ultraviolet laser then scans the cross-section of the CAD model through the resin. The resin is then hardened according to the path the laser travel and repeats the process for each layer until the part is completed [28][29].

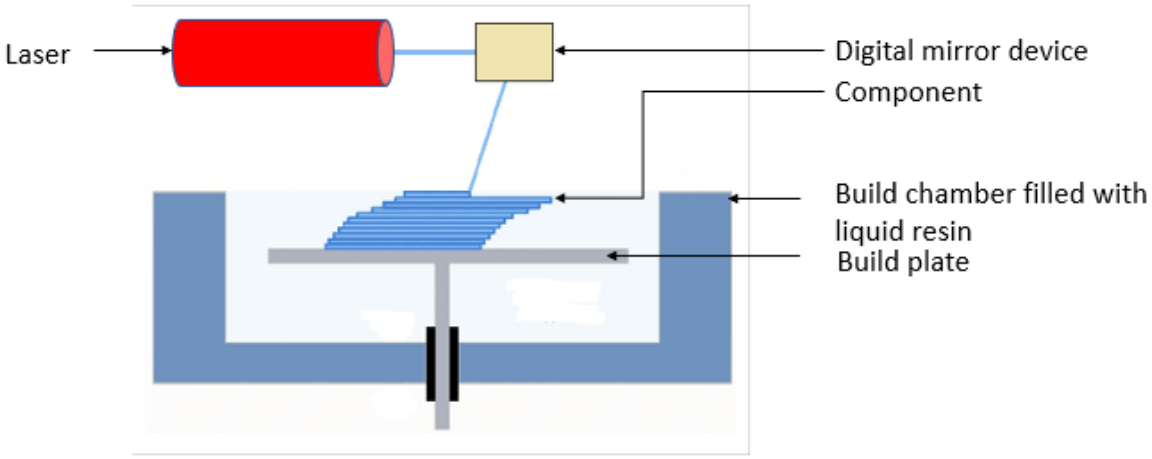

Figure 2-6-Stereolithography process. Adapted from Quan et al. [12].

2.2.5 Powder-based AM.

Figure 2-7 illustrates the PBF and how this process works. The PBF process starts with the build chamber being in a partial vacuum or inert atmosphere that will provide shielding of the molten metal and prevent oxidation and degradation of the powdered material. A thin bed of powder is then lain over the build plate by a recoating mechanism. Some recoating mechanisms are in the form of rollers and others in the form of a blade. The essence of the recoating mechanism is to apply a new layer of powder to the build plate after each cross-section is completed. The build plate is connected to a piston mechanism that lowers the build plate to a set height upon the completion of each layer. The height that the piston will lower is a set value equal to the layer height of the component being fabricated. After the component is fabricated, the excess powder will be removed, revealing the part [30]. Most SLM machines make use of a fibre laser as the energy source to melt the powder particles together. By using a galvanometer, the focus of the beam is adjusted to achieve the right temperature and intensity for the melting process. As the build plate and powder bed are stationary, the focus of the beam is moved around with the use of an F-theta lens [31]. The powder particles that are not melted or used during the fabrication process is removed and can be recycled for future build to minimize material wastage.

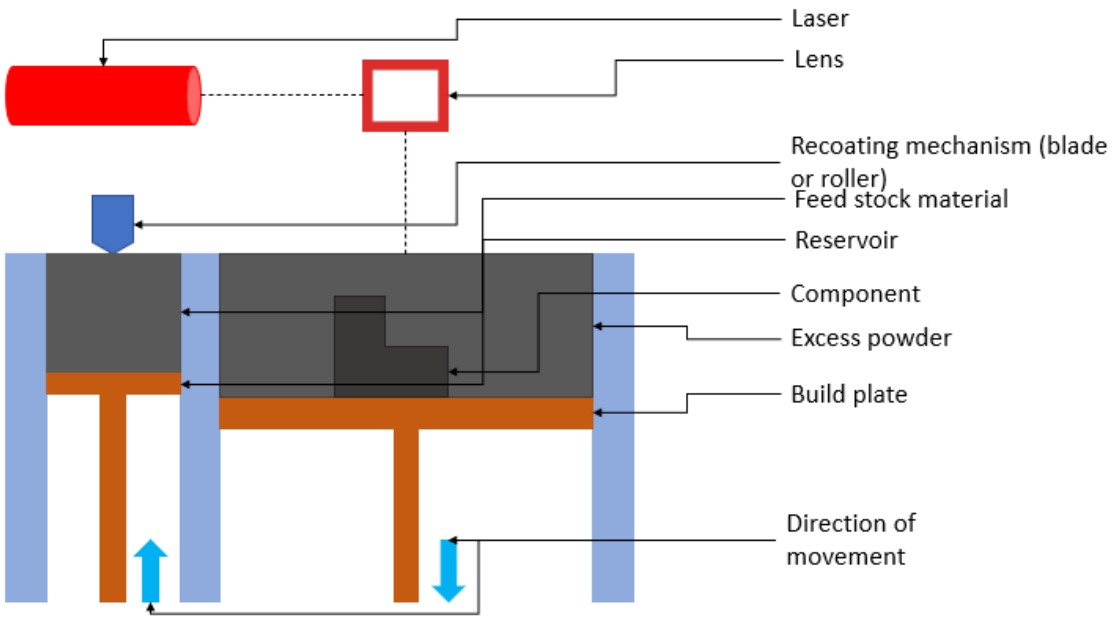

Figure 2-7-Powder Bed Fusion Process

2.3 Metal additive manufacturing.

The process of MAM can be compared to the SL process as the method of fabrication is similar. Instead of using a liquid bases polymer and an ultraviolet laser as in SL, MAM uses a high power

laser or electron beam to fuse metallic, ceramic or other powders to build up the component in a layer by layer fashion [32][33][34]. MAM can be divided into two subcategories, namely Selective Laser Melting (SLM) and Electron Beam Melting (EMB). The further classification includes the material feed method, such as wire feed fusion (WFF), powder feed fusion (PFF), direct energy deposition (DED) and powder bed fusion (PBF) [8] [30].

The process starts with the first layer of powder that is deposited onto the build plate. A high energy density laser is then used to melt the powder particles together according to the CAD data. After the first layers scanning process has been completed, the procedure will repeat until the component is finished [34]. The MAM method has been adopted by aerospace, engineering and medicine due to the manufacturing methods capabilities to fabricate complex geometries that would otherwise be too expensive or impossible to manufacture with traditional manufacturing technologies [35][36][37]. During prefabrication, specific process parameters must be calibrated to achieve the required dimensional tolerances and mechanical properties in the component. Parameters such as laser power, hatch spacing, scanning speed and layer height are set to achieve a single melt track that will completely bond with the adjacent melt tracks and the previous layer of the component [34]. The build chamber of the machine will often be purged with a non-reactive gas such as nitrogen or argon, which protects the components from oxidation during the printing process. Each variable will influence the component's mechanical and thermal properties during fabrication and post-processing, which can lead to certain limitations of the MAM process.

2.3.1 Limitations of metal additive manufacturing

2.3.1.1 Residual stress

Residual stress can best be described by the stress that would exist in a component in the absence of external loads [13][38]. Classification of residual stress is according to the mechanisms which produce the stress, namely, structural mismatching and uneven distribution of non-elastic strains [39]. These different residual stresses can further be classified according to the scale on which they occur [39] [40]:

- Type 1 (σ^{i}): Marco-residual stresses, stresses that vary over a considerable distance and are evident in dimensional variations. Type 1 residual stresses account for large deformation in a component.

- Type 2 (σ^{ii}): Residual stresses that occur because of different phase formations in the material.

- Type 3 (σ^{iii}): Micro-residual stresses, stress that occurs because of dislocation at an atomic scale.

According to Fergani et al. [41], residual stress in AM "is a result of the high energy density delivered by the laser during the SLM process that produces subsequently high thermal gradients during fabrication within the component." The non-uniform expansion and compression forced-induced by the thermal gradients can potentially produce significant residual stresses. The high thermal gradients during fabrication are not the only source to induce thermal expansion. As the laser scans over the powder and forms a melt track, different phases of the material are present (Type 2 residual stress). As a result of the thermal expansion coefficient of the material present in different phases, thermal expansion is expected at different rates. While the laser scans the cross-sectional area of the CAD design, the areas surrounding the melt tracks will be thermally affected and change the thermal behaviour of the component [42][13][43][44]. This region, including the melt pool, is known as the heat-affected zone (HAZ). See Figure 2-8 [45]. Brice et al. [45] and Fergani et al. [41] have concluded in previous studies that the HAZ will influence the thermal behaviour of the melt track and component. The conclusion was that supplying additional heat to the completed and previous layers during fabrication and after the cooling process can significantly decrease the resulting residual stress induced by the HAZ in the component. This additional energy in the cycle will serve for a continuous relaxation of residual stress acting as a stress relief heat treatment of the layers while the component is fabricated.

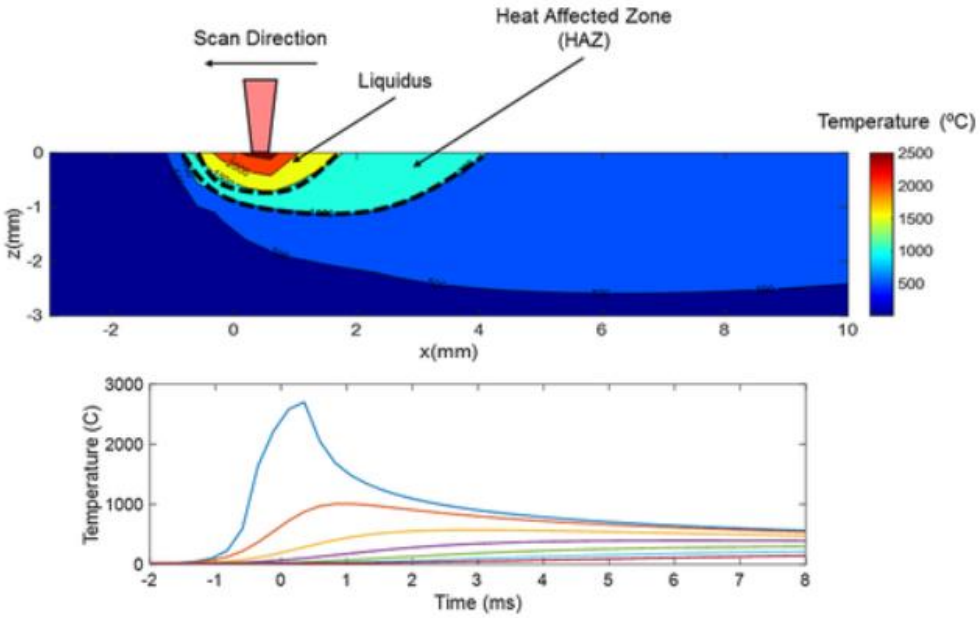

Figure 2-8-Depiction of laser scanning and affected zones. Reproduced with permission from O Fergani et al. [41]

2.3.1.2 Support structures in AM components

Support structures serve a multitude of purposes, such as the conduction of heat, connecting components to the build plate of the AM machine and supporting the overhanging material. Support structures are divided into two categories, active and passive support structures. As explained by Morgan et al. [46], any components that are fabricated in loose powder should be accompanied by passive support structures during fabrication. Any component that utilizes a passive support structure can also be referred to as a floating component. According to Morgan et al.[46] the most common support structures are active support structures that are used to support any geometry that has an angle that surpasses the physical manufacturing capabilities of the AM machine or has overhanging angles. Support structures serve as a direct connection between the part and build plate to support the overhanging material and to decrease the risk of deformation of the part and the overhanging areas. As the laser melts the powder particles, the heat input will result in the component expanding and shirking. By increasing the component's height, the thermal gradient at which the component is cooled and heated is different at specific points on the part. This non-uniform expansion and contraction will result in residual stress in the component. If the residual stress exceeds the strength of the support material, the component will yield and deform. This deformation can lead to defective parts and damage to the AM machine. One of the alternatives would be to strengthen the support material to the point where the residual stress can never exceed the strength of the support material, but by following this approach, the post-processing of the component will increase in difficulty during the support removal phase and prolong the post-processing needed for achieving the desired tolerances and surface finish. Therefore, all the support structures should be optimized for each component that is fabricated to ensure the support material is strong enough to counteract the effect of internal stress but not too difficult to remove. Optimizing and refining the component and support structures to minimize the post-processing of the part can significantly increase the success rate and lower the cost per unit part [47][48][49].

The PBF process starts with the first layer of metal powder melted directly to the solid base plate. This first layer will form the base layer of the support structures that are connected to the base plate and component. The layering of the material then continues as each of the following layers is melted to the previous layer to complete the component and the support structures that are connected to the part. The process can be seen in Figure 2-9, which depicts the process of the first layer and the following layers that are melted onto each other. During PBF processes, all support structures are manufactured using the same material as the part, unlike FDM fabrication, where support structures can be manufactured with a different material than the component. The support structures are removed after fabrication from the component by either or a combination

of cutting, breaking, and machining processes. The support structure removal process after manufacturing can result in damage to the component to such an extent that the fabricated component is rendered unusable and discarded. Therefore support structures should be removed with care to prevent damage to components [46].

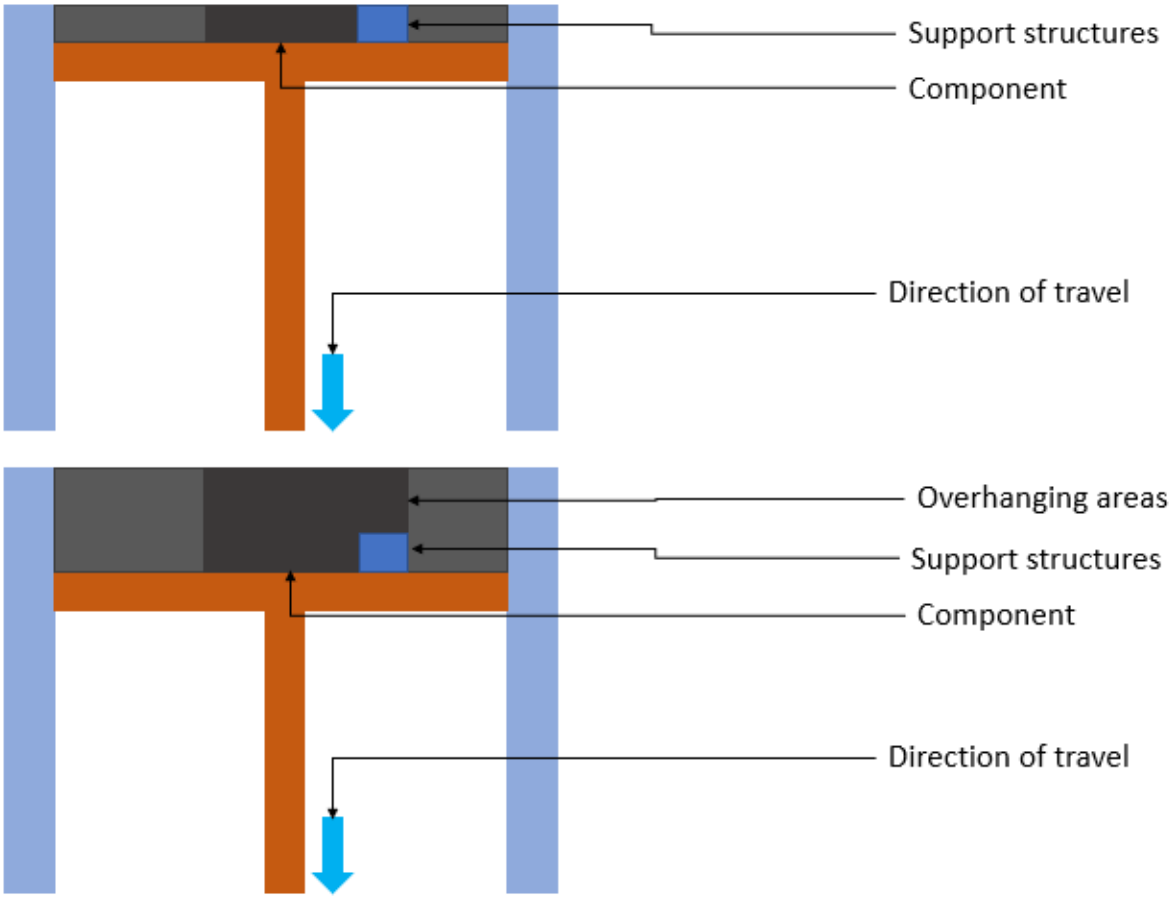

Figure 2-9-PBF component and support structure fabrication process.

2.3.1.3 Parameters and the impact thereof on the printing process

Parameters during manufacturing play a definite role in the successful fabrication of the component [50]. As different process parameters can influence the mechanical properties of the material, as shown in a study conducted by P. Hanzl et al. [51]. The study concluded that parameters such as laser speed and laser power would have the most significant effect on mechanical properties such as the tensile strength of the part. Laser speed and laser power will influence the dwell time and cooling rate of the melted powder resulting in a more refined grain structure compared with traditional manufacturing processes. Using a higher laser power and slower speeds will result in deeper penetrating and larger cross-sectional areas of the melt pools. Deeper and larger melt pools overlap more between adjacent melt tracks, which will reduce the lack of fusion porosity and stabilize the melt pool to avoid rupture. This effect is also known as

balling [52]. Increasing the power of the laser above a certain threshold of the powder and material characteristics can result in vaporization zone formation. This phenomenon is due to gaseous voids forming in the melt layer because of the overheating and vaporization of the metal powder. As the next layer of powder particles are dispersed, the voids that formed can be filled, but in some instances where the laser penetration was too deep, the powder may not fill the holes. A study conducted by Leung et al. [32] used a high-speed camera to capture the moment of vaporization when the first melt track is scanned upon a layer of powder without any anchoring. Figure 2-10 depicts the vapours blowing out metal powder particles as the gasses are released. Figure 2-11 depicts droplet and powder spatter as a result of blowback[5].

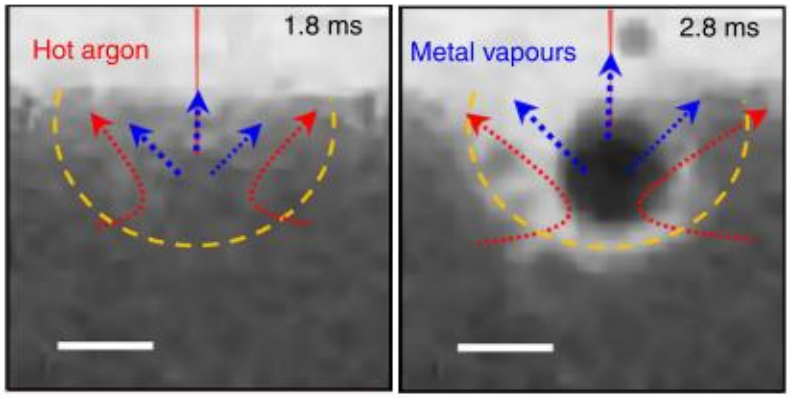

Figure 2-10-Vapour formation during the melting process. Reproduced with permission from Chi Lun Alex Leung et al. [32]

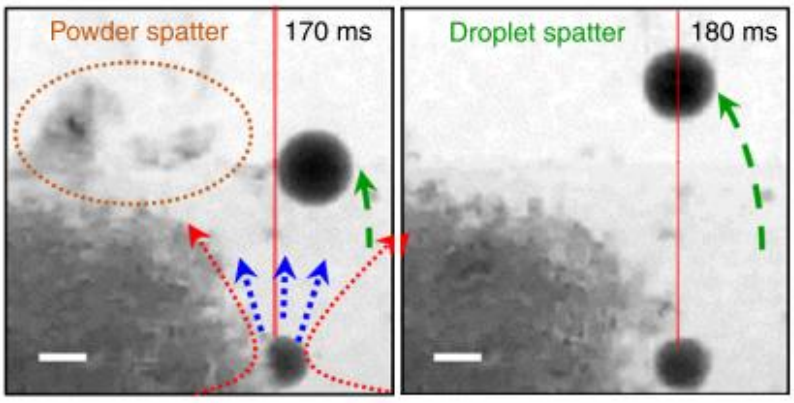

Figure 2-11-Blow back due to vaporization. Reproduced with permission from Chi Lun Alex Leung et al. [32]

[5] Blowback refers to the vapour release during the melting process that forces powder and metal droplets to escape the melt pool.

The shape and characteristics of a vaporization zone are driven by the recoil pressure and thermal gradient between the vapour and liquid interface [50]. This shape and characterization are used as a ground base on determining whether keyhole porosity is formed or not [53]. When the first melt track is scanned into the powder, the depth of the melt track will differ from the depth of a melt track lain upon a previous layer. In a study by Teng et al. [50], different laser powers and different scanning speeds were implemented to examine the penetration depth of the laser beam on the first melt track in the powder substrate. In Figure 2-12, the different penetration depths are clearly shown.

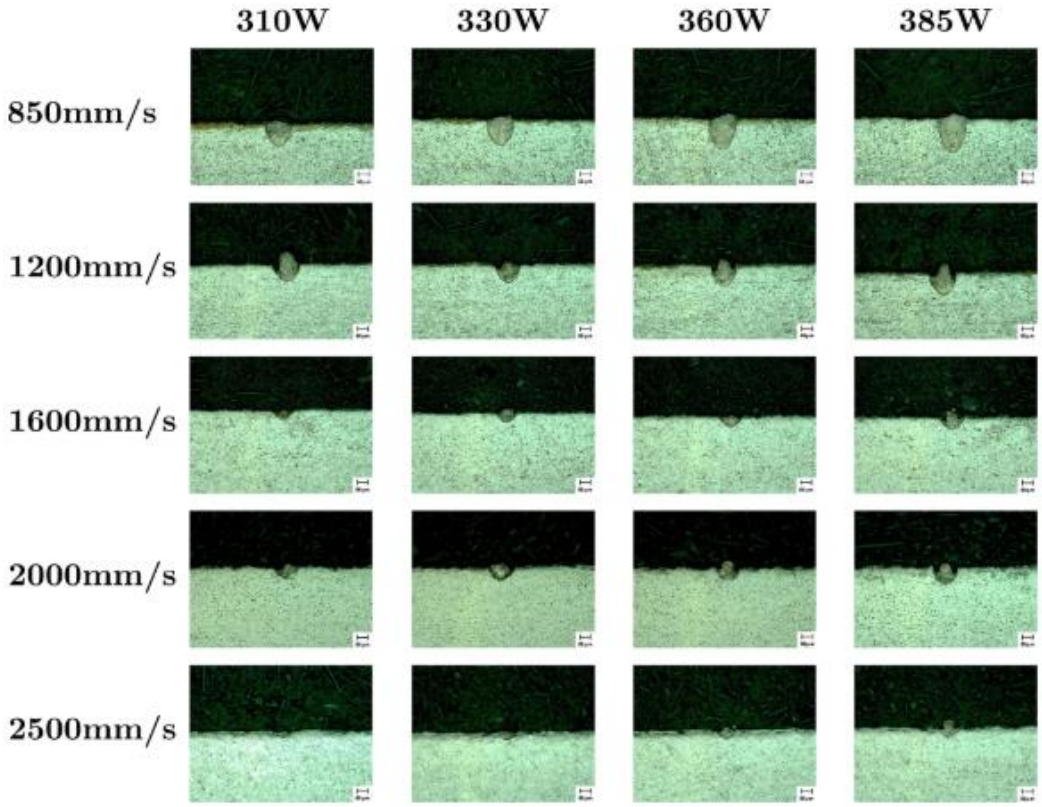

Figure 2-12-Penetration depth of laser during first melt track. Reproduced from Chong Teng et al. [50]

2.3.2 Cobalt chrome

One of the most known and used base metal alloys used for biomedical, orthopaedic, and dental applications is Cobalt Chromium (CoCr). As described by Al Jabbari [54], CoCr alloys have high strength, heat resistant, nonmagnetic, favourable resistance to wear, corrosion, and tarnish. In AM, the CoCr powder consists of a set formula for the material to achieve a standard composition to recreate previous manufacturing parameters. The chemical composition of CoCr powder can be found in Table 2-1. To achieve good powder packing properties of the metal powder particles,

the nominal shape of the particles are spherical with a size distribution of between 20µm-50µm [34] [53] [55].

Table 2-1-Chemical Composition of CoCr Powder [50]

Element	Symbol	Wt.%
Carbon	C	≤0.14
Silicon	Si	≤1.0
Nickle	Ni	≤1.0
Cobalt	Co	Balance
Iron	Fe	≤0.75
Manganese	Mn	≤1.0
Chrome	Cr	26.0-30
Molybdenum	Mo	5.0-7.0
Nitrogen	N	≤0.25

In cases where biomaterial such as bone and teeth are replaced by removable or permanent implants, for instance, removable partial dentures (RPD), CoCr is a well sought after material concerning biocompatibility and previously named material properties [31] [56]. The dimensional accuracy of such parts is of utmost importance as the implants should be custom to each patient [54].

2.4 AM simulation software packages.

To utilize the method of distortion compensation for SLM parts, a simulation program must be used to predict the deformation of the component and apply the distortion compensation algorithm to the geometry of the part. There are several commercially available software packages that provide the ability to apply distortion compensation to components. The leading companies in this field are Simufact additive, ANSYS additive suite, Materialise Magic, Dassault Systems, Siemens, and Altair. For this study, a comparison of solving methods of only Simufact additive and ANSYS additive suite will be investigated as these simulation packages aims to focus mainly on the AM process and the AM workflow.

MSC Simufact Additive and ANSYS additive suite (AAS) are both designed to operate on the principles of the finite element simulations and directly facilitate the SLM process [57]. Both

Simufact Additive and AAS use layer discretization with voxel elements for functions such as distortion prediction and deformation compensation. AAS offers the option between voxel elements and tetrahedral elements during the meshing procedure, whereas Simufact Additive only offers voxel elements during this stage [22].

2.4.1 ANSYS additive suite

The AAS software package was developed to be fully adaptable in the ANSYS Workbench environment, which enables the user to work in parallel with other ANSYS software. The workflow process in AAS starts by meshing the components either with voxel elements or tetrahedral elements, where each of the meshed layers represents several actual metal layers. The assumption during this process is that thermal continuity exists between the layers. The simulation process needs extensive input data and parameters before the simulation can start. Basic material properties such as elastic modulus, orthotropic thermal conductivity, Poisson's ratio, density, coefficient of thermal expansion, elastic bilinear curves of plastic stress and strain and specific heat capacity should manually be entered into the simulation domain [22] [58]. The main parameters that are necessary to simulate a component in AAS can be found in Table 2-2.

Table 2-2-Simulation parameters needed in ANSYS additive suite

Parameter	Value
Element size	1mm
Method	Cartesian
Hatch spacing	0.11mm
Scan speed	650mm/s
Laser power	200W
Preheat temperature	22°C
Layer thickness	50µm
Scan strategy	Meander

2.4.2 MSC Simufact additive

MSC Simufact Additive is a computer software simulation package designed for SLM processes and technologies. Simufact Additive also facilitates laser beam melting (LBM), electron beam melting (EBM) and direct metal laser sintering (DMLS) methods of fabrication. The software works

on the principle of finite element (FE) simulation to predict outputs such as distortion and residual stress in a component because of the fabrication process. These predictions of stress and deformation can aid with the component design phase by predicting the optimum design of the component and orientation during the fabrication phase to minimize resource usage [22] [58]. Simufact Additive aims to simulate the whole AM process instead of focusing only on the fabrication process. Post-processing methods such as support cutting, hot isostatic pressing, heat treatment, and evaluation processes are included in the software package. The software also includes a material and powder database that eases the simulation setup process and includes a variety of MAM powders and their properties [22]. The chosen software package for this study is Simufact Additive (hereafter only referred to as Simufact).

2.4.2.1 Meshing process used in Simufact

Voxel meshing in Simufact is completed by utilizing hexahedral element meshing for the component. When the voxel mesh is created, a 3-D network is created over the component using volumetric mesh structures, after which a surface mesh is created on the component. With the use of the voxel mesh and surface mesh, guaranteed component coverage can be assured. All output results of the simulation are linked to the mesh created before the start of the simulation. With the use of the connection list in the output file, Simufact provides individual properties of each nodal point in the mesh. Simufact thus utilizes the knowledge of the properties of the material and how the material will react in certain situations and uses the deformation prediction and compensation method to achieve the desired tolerance when manufacturing geometry sensitive components [22] [59].

2.4.2.2 The mathematical method used for calibration and prediction in Simufact

The ISM was initially developed for the measurement and modelling of the distribution of three-dimensional welding residual stresses in the welding joint [60]. This method translates the deformation of a component into unit strain tensor values in an element. The elemental strain increment consists of an elastic strain, plastic strain, thermal strain, and phase transformation induced strain. When the heating and cooling process is finished, the total residual strain in an element is the summation of all the strains present in the element [60]. As SLM can be compared with a micro-welding process, the ISM can be modified to satisfy the condition for SLM processes [61].

CHAPTER 3

THEORY

3.1 Inherent strain method.

When regarding the residual stress of any component, the state of equilibrium with regards to the stress and the strain in the part should be analysed. When this equilibrium state is out of balance, a strain field cannot exist without the accompanying stress. To fit the existing strain field within the parts body, stress within the component must be present [60]. To fit the strain field, the component must therefore deform to bring all forces acting on and within the component into equilibrium. This strain field may be caused by many means and include plastic deformation, thermal strain, and phase transformation. The residual stress within the component can be altered by sectioning the component and forcing a line of deformation. Having an ideal cutting line, the component can be sectioned without altering the inherent strain found within the original part. By cutting the component, the residual stress distribution will be changed but not the inherent strain within the part [60]. The deformation of the component as a result of the sectioning phase is then measured to calculate the inherent strain tensors present in the component. These inherent strain tensors or Eigen strain tensors can then further be used to calculate the residual stress that was present in the component before the sectioning phase. These values are then used to predict the deformation of a component manufactured with the same material and parameters.

The Eigen strain tensor variable ϵ^*, indicates any strain that is permanent in the material due to processes such as crystallography transformation, thermal expansion, and plastic deformation, which will give rise to residual stress in the component. The total strains can thus be expressed by the use of the small strain approximation that dictates that the total strain is the sum of the elastic strain, which is governed by the theory of linear elasticity, and the present Eigen strains.

Equation 3-1 The small strain approximation

$$\epsilon_{total} = \epsilon_e + \epsilon^*$$

where ϵ_e represents the elastic strain and ϵ^* is the Eigen strain.

The term Eigen strain can also be referred to as inherent strain, which was introduced by Ueda [62] in 1975. The induced residual stress in a component may be regarded as the results of an incompatible strain field consisting of shrinkage strain, plastic strain, creep strain and phase transformation strain. The use of Eigen strains for calculating the residual stress can be classified into two categories, the direct problem of Eigen strain theory [63] where an Eigen strain value is used to deduce the residual elastic strain and stress fields everywhere in the component, but this method can only be used for a uniform Eigen strain distribution. The second method was proposed by Toshio Mura in 1982 to analytically find the residual elastic strains and stresses

within the extended elastic body which contains a non-uniform Eigen strain distribution. The following formula shows the relationship between the Eigen strain distribution and the corresponding residual elastic strain, Equation 3-2.

Equation 3-2-Mura Eigen strain equation

$$e_{kl}(x) = -\epsilon^*_{kl}(x) - \int_{-\infty}^{\infty} C_{ijkl}\epsilon^*_{mn}(x')G_{kp,ql}(x-x')dx)$$

Where C_{ijkl} represents the elastic stiffness coefficient, $G_{kp}(x-x')$ denotes Green's function for the particular geometry representing the displacement component in the k direction at x when a force is applied at x' in the p direction[64].

The inverse problem of the Eigen strain theory state that with knowledge of the residual deformation state, the corresponding underlying Eigen strain distribution can be calculated. The basis of the analytical approach to the inverse problem of Eigen strains theory is that with a comparison between measured experimental data and the original deformation state, the Eigen strain field can be reconstructed [65].

Ueda et al. [62] introduced a method based on the ISM in correlation with the finite element analysis to calculate and predict the residual stress in components [65]. In this method, the relationship between the inherent strain $\{\epsilon^*\}$ or the elastic strain $\{\epsilon\}$, or the stress $\{\sigma\}$ produced by the inherent strain at a point on the component can be expressed by Equation 3-3 and Equation 3-4.

Equation 3-3 Stain based on the ISM method

$$\{\epsilon\} = [H^*]\{\epsilon^*\}$$

Equation 3-4 Stress based on the ISM method

$$\{\sigma\} = [D]\{\epsilon\} = [D][H^*]\{\epsilon^*\}$$

Where $[H^*]$ represents the elastic response matrix and $[D]$ the elasticity matrix.

With this method, the total strain in any component can be expressed by Equation 3-5

Equation 3-5 Total strain of the component

$$\epsilon_{total} = \epsilon_{elastic} + \epsilon_{plastic} + \epsilon_{thermal} + \epsilon_{phase} + \epsilon_{creep}$$

The total strain of the system can also be rewritten in terms of the inherent strain, see Equation 3-1.

The inherent strain can be introduced into the FEM model by using Equation 3-6 to Equation 3-11.

Equation 3-6 Force equation

$$F = \int_{v}^{0} B^T D \epsilon^* dV$$

Where B represents the strain displacement matrix, D is the compliance, and K is the stiffness matrix.

The strain displacement matrix can be calculated using Equation 3-7

Equation 3-7 Strain displacement matrix

$$B = J\left[\frac{dN_1}{d\zeta} \quad \frac{dN_2}{dx} \quad \frac{dN_3}{dx}\right]$$

Where J represents the Jacobian matrix, ζ the isoperimetric natural coordinate, and N_i is the shape function.

Equation 3-8 Displacement matrix

$$\underline{u} = K^{-1}F$$

Equation 3-9 Strain as a function of the strain displacement and displacement matrix

$$\epsilon = B\underline{u}$$

Equation 3-10 Strain

$$\epsilon_{elastic} = \epsilon_{total} - \epsilon^*$$

Equation 3-11 Stress

$$\sigma = D\epsilon_{elastic}$$

3.2 Finite element method.

FEM is a numerical solving solution that can be utilized to analyse component deformation, stress, heat flux, magnetic flux and solve other engineering flow problems. The FEM analysis works by breaking down a complex geometry or domain into simple geometric shapes called finite elements [66][67]. The element corners will form a mesh over the complex geometry and can be focused upon individually. Considering the relationships between each of the elements and the material properties of the original geometry, the corners of the elements can be expressed in terms of unknown values. By considering the loading and constraints of the elements, a set of equations can be formed to find an approximation of the behaviour of the geometry [68]. Figure 3-1 is a representation of a body having a volume of **V** and a surface of **S**. Within this body, there exists a point **X** that can be located by the position coordinates **(x, y, z)** of point **X**. By applying a distributed force, **T**, the body will deform under the load. The deformation of the body will affect point **X** as this point will also undergo deformation and change the original **(x, y, z)** coordinates to a new set of coordinates **(x', y', z').**

The deformation of point X can be calculated by using the three components of the displacement vector, namely.

Equation 3-12-Displacement vector.

$$\boldsymbol{u} = [u, v, w]^T$$

The distributed force per unit volume can be calculated with the use of the force vector.

Equation 3-13-Force vector.

$$\boldsymbol{F} = \left[F_x, F_y, F_z\right]^T$$

As the external load is applied and the elements deform, different stresses will act on the element's volume **dV**. The stresses acting on the element include the normal stress, and shears stress and are represented by six individual components.

The normal stress is represented by, $\sigma_x, \sigma_y, \sigma_z$ and the shear stress represented by $\tau_{xy}, \tau_{xz}, \tau_{yz}$. The six components represent the stress in the element.

Equation 3-14-Elemental Stress.

$$\sigma = \left[\sigma_x, \sigma_y, \sigma_z, \tau_{xy}, \tau_{xz}, \tau_{yz}\right]^T$$

The forces acting on each of the element **dV** are developed by multiplying the area and the stress, and considering the equilibrium of the element **dV** the equilibrium equations are:

Equation 3-15-Equilibrium equations.

$$\Sigma F_x = \frac{\partial \sigma_x}{\partial \boldsymbol{x}} + \frac{\partial \tau_{xy}}{\partial \boldsymbol{y}} + \frac{\partial \tau_{xz}}{\partial \boldsymbol{z}} + f_x = 0$$

$$\Sigma F_y = \frac{\partial \tau_{xy}}{\partial \boldsymbol{x}} + \frac{\partial \sigma_y}{\partial \boldsymbol{y}} + \frac{\partial \tau_{yz}}{\partial \boldsymbol{z}} + f_y = 0$$

$$\Sigma F_z = \frac{\partial \tau_{xz}}{\partial \boldsymbol{x}} + \frac{\partial \tau_{yz}}{\partial \boldsymbol{y}} + \frac{\partial \sigma_z}{\partial \boldsymbol{z}} + f_z = 0$$

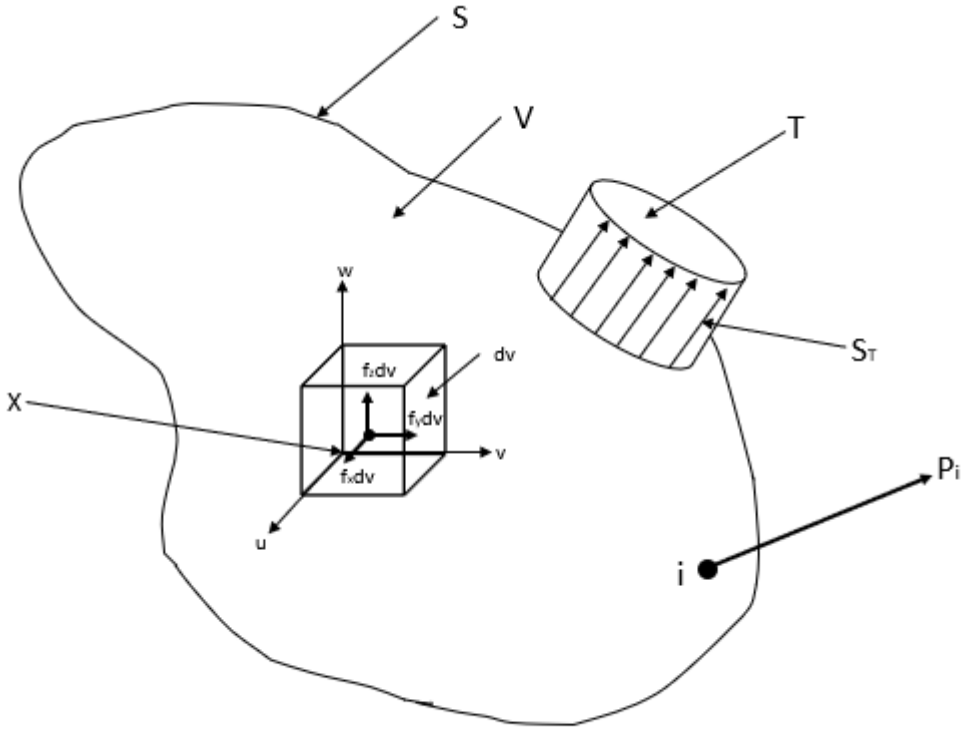

Figure 3-1-Body under load. Adopted from Fish et al. [66]

When the body is discretized, the mesh will be connected to the nodal points. When performing a FEM, each of the nodal points becomes the focal point of each nodal equation. If the behaviour of each nodal point can be analysed, a very accurate assumption can be made about the

behaviour of the system. Figure 3-2 depicts the mesh and the nodal points in the mesh of discretized system.

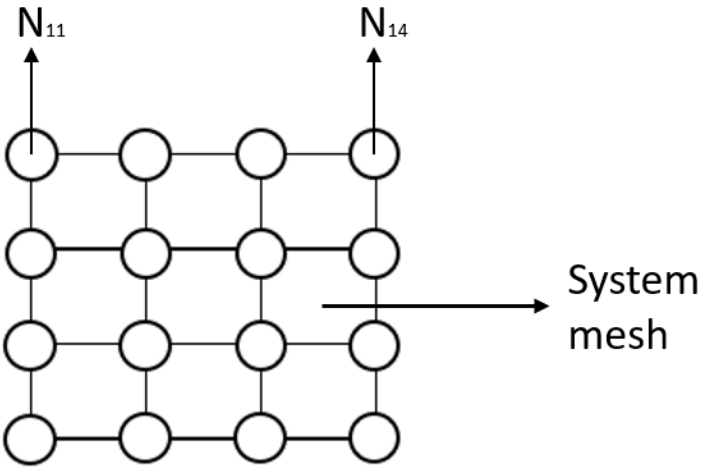

Figure 3-2-FEM mesh and nodal points

To illustrate, the focal point of the system will be two nodal points. A force is applied to the system, and the behaviour of the nodal points is analysed. The force applied to the system will result in a nodal displacement. For the calculation of stress and strain, the following formulas are well known.

Equation 3-16-Stress experienced by the nodal point

$$\sigma = \frac{F}{A_0} = \mathrm{E}\epsilon$$

Equation 3-17-Strain experienced by the nodal point

$$\epsilon = \frac{\Delta L}{L} = \frac{u_2 - u_1}{L}$$

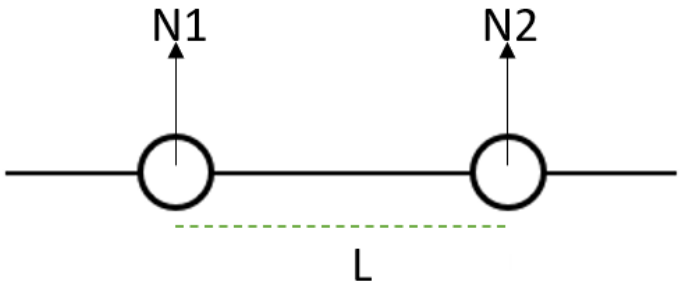

Figure 3-3-FEM binodal system.

Figure 3-3 depict the mesh of a system with two nodal points with a distance of L between nodal point N1 and N2. When a force is applied to the system, N1 and N2 will be affected by the force and undergo a displacement due to the force. As in Figure 3-4, nodal point N2 has displaced with a displacement of L1.

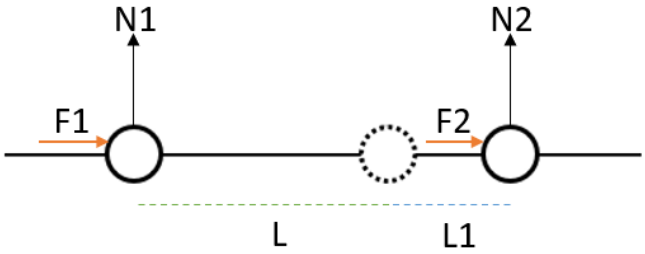

Figure 3-4-Displacement of nodal point

Form Equation 3-15, the summation of the forces in the system must be calculated.

Equation 3-18 System force exerted on nodal points

$$\Sigma F_x = F_1 + F_2$$

Combining Equation 3-16 and Equation 3-17 yields,

Equation 3-19 Nodal force

$$F = \frac{EA(u_2 - u_1)}{L}$$

Calculating the forces of equilibrium and rewritten in matrix notation yields

Equation 3-20 System force in matrix notation

$$\begin{bmatrix} F_1 \\ F_2 \end{bmatrix} = \frac{EA}{L} \begin{bmatrix} 1 & -1 \\ -1 & 1 \end{bmatrix} \begin{bmatrix} u_1 \\ u_2 \end{bmatrix}$$

With the use of Equation 3-20 and the general stiffness matrix, the equation can be manipulated to solve a finite number of nodal points by adding the nodal points to the matrix.

Equation 3-21 General formulations of FEM matrix force

$$\begin{bmatrix} F_1 \\ F_2 \\ F_3 \end{bmatrix} = \begin{bmatrix} k_1 & -k_1 & 0 \\ -k_1 & (k_1 + k_2) & -k_2 \\ 0 & -k_2 & k_2 \end{bmatrix} \begin{bmatrix} u_1 \\ u_2 \\ u_3 \end{bmatrix}$$

Which will result in the general formulation, which is used FEM.

Equation 3-22 Force as a function of the general stiffness matrix and displacement matrix

$$[F] = [K][U]$$

Where [F] results in the force matrix, [K] the general stiffness matrix and [U] the displacement matrix.

3.3 Using the ISM in conjunction with the FEM

To utilize the ISM for the calculation of displacements and strains in any components, the method must be combined with a FE approach. As explained in section 3.2, the FEM consists of a system of elements and nodes that are used to derive the stress state of the part using the strains applied [69]. To calculate the displacement of a nodal point in the system, the assumption is made that the displacement is a weighted contribution of the displacement at the ends of the bar. For the one-dimensional system shown in Figure 3-5, the system comprises of two nodal points with a uniaxial load applied to the nodal points. The displacement of the element, which is denoted as $U^e(x)$ is a function of the shape function and the displacement of the nodal point.

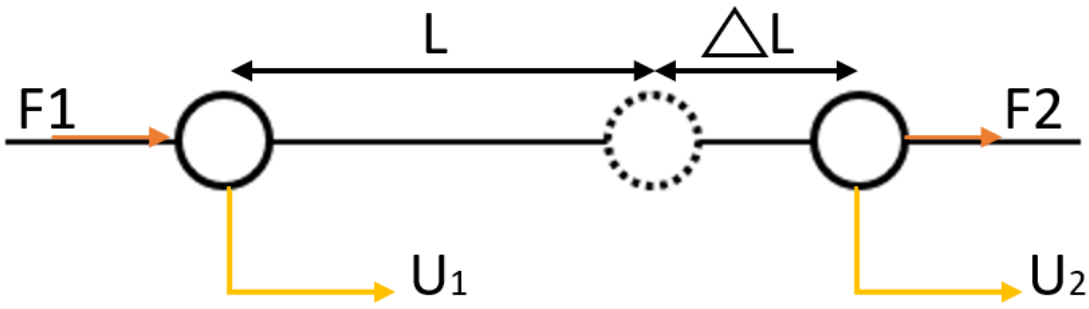

Figure 3-5- One-dimensional system

The displacement of the element at an arbitrary point x can be calculated with the following equation with $U^e(x)$ the displacement at point (x), and U_p^e the nodal displacement of each of the nodes. With N^e known as the shape function matrix, which is used to interpolate the element displacement from the nodal displacement.

Equation 3-23 Nodal point displacement

$$U^e(x) = N_1 U_1^e + N_2 U_2^e = [N_1\ N_2][\begin{bmatrix} U_1^e \\ U_2^e \end{bmatrix} = N^e u^e$$

To derive the shape function of the system at point (x) that is located at an arbitrary point on the length of the element L choosing the point (x) that the distance from the left can be calculated by using Equation 3-24.

Equation 3-24-Distance of node X

$$X = x - x_1$$

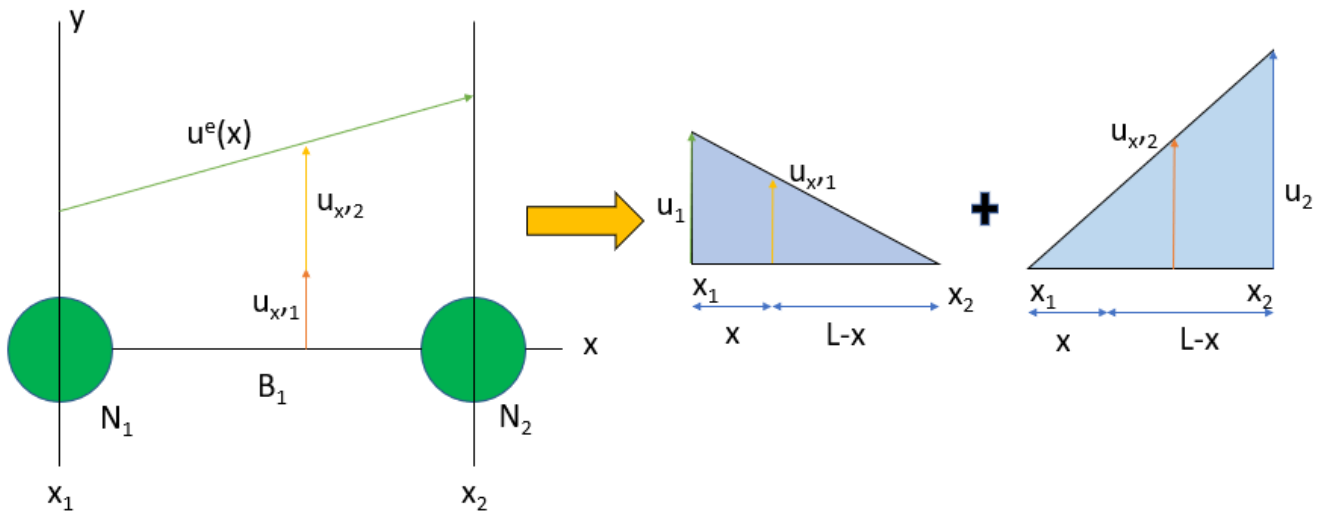

Figure 3-6- Shape function derivation adapted from [69]

From Figure 3-6, the congruence of the triangles can be used to formulate Equation 3-25 and Equation 3-26.

Equation 3-25 Nodal point - N_1

$$N_1 : \frac{U_{x,1}}{U_1} = \frac{L - X}{L} \; so \; that \; N_1^e U_1 = \left[1 - \frac{X}{L}\right] U_1$$

Equation 3-26 Nodal point - N_2

$$N_2 : \frac{U_{x,2}}{U_2} = \frac{L - X}{L} \; so \; that \; N_2^e U_2 = \left[\frac{X}{L}\right] U_2$$

The shape function can now be rewritten to use isoperimetric natural coordinates for each of the nodal points and setting ζ as the isoperimetric natural coordinate correlating to the x-direction of displacement. As shown in Equation 3-27 and Equation 3-28.

Equation 3-27 Nodal point N_1 in isoperimetric natural coordinates

$$N_1^e = 1 - \frac{X}{L} = 1 - \zeta$$

Equation 3-28- Nodal point N_2 in isoperimetric natural coordinates

$$N_2^e = \frac{X}{L} = \zeta$$

To derive the strain displacement matrix for the system in Figure 3-5, the displacement of the element $U^e(x)$ is described by a guess displacement value as the actual displacement of the nodes will be calculated using the shape function of the system. The guess values will serve as the initial step in the iterative process to solve the displacement of the nodal points until coverages are achieved.

3.3.1 Determination of the associate strain of an element

The axis strain of the system can be represented by Equation 3-29.

Equation 3-29-Axis strain

$$\epsilon^e(x) = \frac{du^e(x)}{dx} = \begin{bmatrix} \frac{dN_1^e}{dx} & \frac{dN_2^e}{dx} \end{bmatrix} \begin{bmatrix} u_1^e \\ u_2^e \end{bmatrix}$$

With

$$\frac{dN_1^e}{dx} = -\frac{1}{L}$$

$$\frac{dN_2^e}{dx} = \frac{1}{L}$$

Equation 3-29 can be rewritten to contain the strain displacement matrix $\boldsymbol{B}$ which gives

Equation 3-30-Strain displacement matrix

$$\epsilon^e(x) = \mathbf{Bu}^{\mathrm{e}}$$

The strain displacement matrix can be represented with isoperimetric natural coordinates given in

Equation 3-31-Strain displacement matrix

$$\mathbf{B} = \begin{bmatrix} \frac{dN_1^e}{dx} & \frac{dN_2^e}{dx} \end{bmatrix} = \begin{bmatrix} \frac{dN_1^e}{d\zeta}\frac{d\zeta}{dx} & \frac{dN_2^e}{d\zeta}\frac{d\zeta}{dx} \end{bmatrix} = \frac{d\zeta}{dx}\begin{bmatrix} \frac{dN_1^e}{d\zeta} & \frac{dN_2^e}{d\zeta} \end{bmatrix} = \mathbf{J}^{-1}\begin{bmatrix} \frac{dN_1^e}{d\zeta} & \frac{dN_2^e}{d\zeta} \end{bmatrix}$$

Following the strain displacement matrix, the force-displacement must be solved next. The step is done by an energy balance of the system, which is the total internal energy and the external work applied to the system given in Equation 3-32.

Equation 3-32-Energy balance of system

$$\mathbf{U}_{int}^e = \frac{1}{2}\left[u^e(x)\frac{E^eA^e}{L^e}u^e(x)\right] = \frac{1}{2}[(\mathbf{u}^e)^{\mathrm{T}}\mathbf{K}^e\mathbf{u}^e]$$

Equation 3-33 Stiffness matrix

$$\mathbf{K}^e = \int_0^1 E\mathrm{A}\mathbf{B}^{\mathrm{T}}\mathbf{B}L\,d\zeta = \frac{EA}{L}\begin{bmatrix} 1 & -1 \\ -1 & 1 \end{bmatrix}$$

In Equation 3-33 K^e represents stiffness matrix, E Youngs modules, A^e the cress sectional ares of the element and L^e the length of the element. Equation 3-34 represents the work applied to the system.

Equation 3-34-Work applied to the system

$$\mathbf{W}^e = (\mathbf{u}^e)^{\mathrm{T}}\mathbf{f}^e$$

Where $\mathbf{f}^e$ represent the nodal force with the corresponding displacement.

Equation 3-35-Nodal force

$$\mathbf{f}^e = \mathbf{K}^e\mathbf{u}^e$$

The stress of the element can now be calculated with Equation 3-36.

Equation 3-36-Elemental stress

$$\boldsymbol{\sigma}^{\boldsymbol{e}} = E^e\mathbf{B}\mathbf{u}^e$$

Simufact uses a much more complicated system as described using hexahedral elements instead of a one-dimensional linear system. To use this FEM, the solid body is discretized, and each of the nodal points is allocated an isoperimetric natural coordinate. Using the three-dimensional approach, the isoperimetric natural coordinates are expanded to include three dimensions for all

directions of physical distortion the solid body can undergo. The shape function of a hexahedral element is shown in Equation 3-37 [70][71].

Equation 3-37-Shape function of element N_i

$$\mathrm{N_i} = \frac{1}{8}(1+\zeta\zeta_i)(1+\eta\eta_i)(1+\epsilon\epsilon_i)$$

The displacement matrix of the system can now be described in three dimensions, each with a corresponding coordinate, shown in Equation 3-38 and Equation 3-39.

Equation 3-38-Displacement matrix

$$(\mathbf{u}^e)^T = [\mathbf{U}_1 \quad \mathbf{U}_2 \quad \cdots \quad \mathbf{U}_8]$$

Equation 3-39-Displacement matrix

$$\mathbf{U}_i = \begin{Bmatrix} x_i \\ y_i \\ z_i \end{Bmatrix} for\ i = 1,2,\dots,8$$

This transforms the shape as defined in Equation 3-40.

Equation 3-40-Shape function

$$\mathbf{N}^e = [\mathrm{N}_1 \quad \mathrm{N}_2 \quad \cdots \quad \mathrm{N}_8]$$

The strain matrix for the three-dimensional system can now be described as in Equation 3-41.

Equation 3-41-Strain displacement

$$\mathbf{B}_i = \mathbf{L}\mathrm{N_i}$$

3.3.2 Incorporation of the ISM into the FEM

For this derivation, isotropic material properties will be assumed so that the material constant matrix can be defined as in Equation 3-42.

Equation 3-42-Material constant matrix

$$C = \frac{E}{(1+v)(1-2v)}\begin{bmatrix} 1-v & v & v & 0 & 0 & 0 \\ v & 1-v & v & 0 & 0 & 0 \\ v & v & 1-v & 0 & 0 & 0 \\ 0 & 0 & 0 & 1-2v & 0 & 0 \\ 0 & 0 & 0 & 0 & 1-2v & 0 \\ 0 & 0 & 0 & 0 & 0 & 1-2v \end{bmatrix}$$

Coupling the ISM to the FEM will then result in Equation 3-43.

Equation 3-43-$\mathbf{f^e}$ formula

$$\mathbf{f}^e = \int \mathbf{B}^T \, \mathbf{C}\varepsilon^* dV : with\ dV\ the\ volume\ of\ the\ element$$

$$\mathbf{u}^e = (\mathbf{K}^e)^{-1}\mathbf{f}^e$$

$$\varepsilon^{total} = \mathbf{Bu^e}$$

$$\varepsilon^{elastic} = \varepsilon^{total} - \varepsilon^*$$

CHAPTER 4

METHODOLOGY

4.1 Introduction

This chapter aims to provide insight into the methods and experimental procedures that will be used in this study to obtain results that can be objectively quantified to evaluate the efficacy of the distortion compensation method. The required workflow to obtain a distortion compensated geometry will firstly be presented to highlight the importance of each step. Once this has been done, a more detailed and in-process aspect will be addressed to identify the variables at play in this study.

The workflow can be divided into four consecutive phases that need to take place to obtain the distortion compensated geometry. The following section will discuss these processes briefly:

- **Calibration sample fabrication phase**: The calibration phase firstly requires a set of target deformation points that will be used to calculate the system Eigen strain tensor values. These target deformation points are obtained by fabricating the calibration cantilever that is provided by Simufact. After the cantilevers are fabricated, the samples will be partially sectioned with the use of a WEDM, and the deformation of each of the samples will be measured with the use of a CMM machine.
- **Calibration Phase**: The calibration phase is required firstly to quantify the inherent strain present after the production of an SLM manufactured part. The inherent strain caused by high thermal gradients can be quantified by means of the ISM in conjunction with the manufactured calibration sample. This method makes use of the target deformation of the cantilever that was obtained in the previous phase to calculate the correlating Eigen strain tensor values. The result of the calibration phases is a set of Eigen strain tensors in the X, Y, and Z direction that will enable the prediction of stress and deformation in components that are simulated.
- **Validation Phase**: The validation phase will use the Eigen strain tensors values calculated in the calibration phase for the simulation procedure. The cantilever samples that will be simulated are fabricated at an angle of $45°$ relative to the X and Y-axis to evaluate is the calibration was successful, and the predicted stresses and deformation are within reasonable tolerances.
- **Distortion compensation phase**: The distortion compensation phase will use an iterative optimisation process to alter the geometry of the component that is simulated to decrease the deformation of the as-build part. The part will be fabricated, sectioned, and measured to evaluate the accuracy of the predicted deformation and the magnitude of the decrease in distortion of the part.

By completing the listed phases, the efficacy of the distortion compensation method can be evaluated for SLM specimens. Figure 4-1 depicts how the experiment phases of the study will be executed. The fabrication, sectioning and top plane deformation measuring process will be similar for the calibration, validation, and distortion compensation phases of this study.

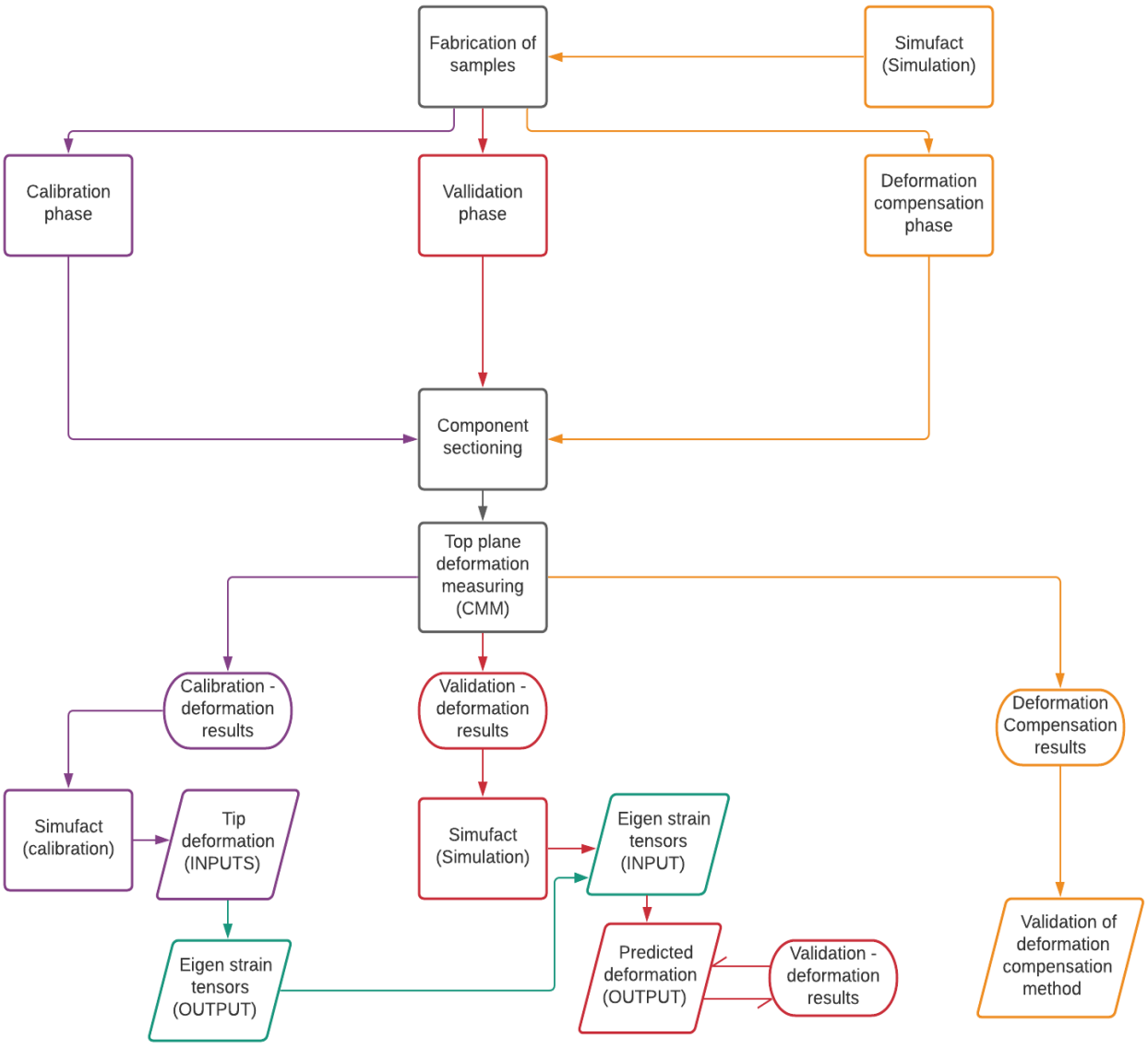

Figure 4-1-Experiment flow diagram.

4.2 Material and Equipment

4.2.1 Orlas creator metal additive manufacturing machine

The manufacturing of samples used in this study was completed on an Orlas creator metal powder bed fusion additive manufacturing system. The printer has a circular build plate with a rotating recoating mechanism that uses a rubber blade to transfer powder from the powder reservoir to the build area. The machine details and system information of the OC printer can be found in Table 4-1 [72].

Table 4-1-OC specifications

Specification of OC	
Laser power	Yb: Fibre 250W
Laser wavelength	1070 nm
Building platform/Volume	100mm x 110mm (diameter x height)
Material deposition	Scraper
Repeatability	X= 15µm, Y=15µm, Z=15µm
Minimum feature size	X=80µm, Y=80µm, Z=20µm
Typical accuracy	40µm
Ready-to-run materials with developed print parameters	Stainless steel (17-4 PH) Cobalt-Chrome (CoCr) Bronze (CuSn8)
Extraction unit	Non-reactive materials

4.2.2 Cobalt Chrome powder for AM.

For this study, the feedstock material used for the fabrication of the cantilever samples will be Cobalt Chrome (CoCr) powder. The CoCr powder is a gas atomized metal powder supplied by Praxair Truform. The feedstock material's chemical composition and mechanical properties can be viewed in Table 4-2 and Table 4-3. Table 4-4 and Figure 4-2 depicts the particle size distribution of the CoCr powder used for this study. The mean particle size of the powder is $27\ \mu m$ which is well between the prescribed particle size AM processes [73]. The following data of the feedstock material was generated by a process known as static automated imaging.

Table 4-2-Chemical composition of CoCr Praxair powder

Chemical Composition (Batch 5190B19-1) CoCr powder			
Element		**Quantity (%)**	**Maximum (%)**
Carbon	C	0.08	0.15
Sulphur	S	0.002	0.010
Cobalt	Co	Balance	
Chromium	Cr	28.31	27.0-30.0
Iron	Fe	0.37	0.75
Manganese	Mn	0.14	1
Molybdenum	Mo	6.15	5.0-7.0
Nickel	Ni	0.17	0.5
Phosphorus	P	<0.005	0.02
Silicon	Si	0.25	1
Tungsten	W	0.06	0.2
Titanium	Ti	0.00	0.1

Table 4-3-Mechanical properties of cobalt chrome AM powder

Mechanical properties of additive manufactured Cobalt Chrome.		
	Yield Strength (YS) [MPa]	**Ultimate tensile strength (UTS) [MPa]**
Changhui Song et al.[74]	662	1210
Leonhard Hitzler et al.[75]	757	1052
Shingo Kurosu et al. [76]	450-920	908-1282
Inhouse testing	691,36	927,4184

Table 4-4-Diameter report of CoCr powder

Diameter report (μm)- Results	
Diameter Mean	27.12 μm
Diameter STDV	10.74 μm
Diameter RSD (%)	39.60 μm
Particles counted	9053

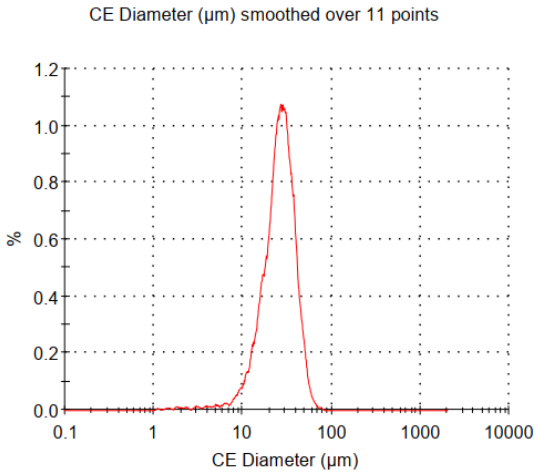

Figure 4-2-Diameter distribution of CoCr powder.

Figure 4-3 and Figure 4-34 depicts Scanning electron microscopy (SEM) images of the powder particles. One thing to note is the distorted shapes of some of the particles. This can be due to the atomization of the particles during fabrication. These non-circular shaped particles can have an impact on the packing density of the powder during fabrication. From this SEM sample, all the shapes are still in the valid tolerances and acceptable deviation of powder standards. The particle size and the circularity of the powder can change as the powder that was not used in the previous build gets recycled. The recycling of powder refers to a series of sifting and drying processes to prepare the powder that did not form part of the component in the previous build.

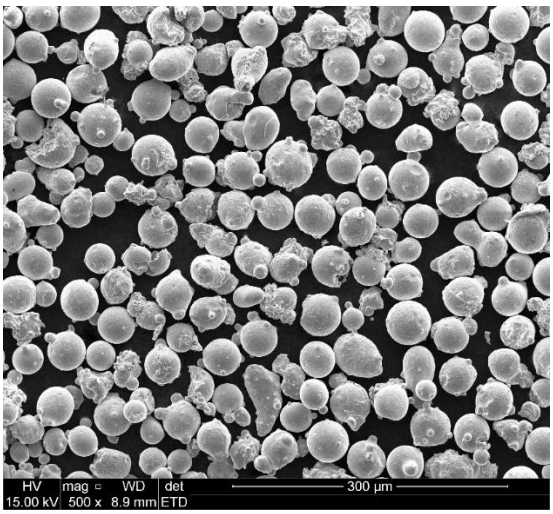

Figure 4-3-SEM image of CoCr powder

Figure 4-4-Closeup SEM of powder particle

4.3 Calibration sample fabrication process

The calibration, validation, and distortion compensation samples that will be used for this study will undergo a series of processes to prepare the samples for further experimentation. The samples will be fabricated, sectioned, and measured before they will be used in the various divisions of this study, as shown in Figure 4-5.

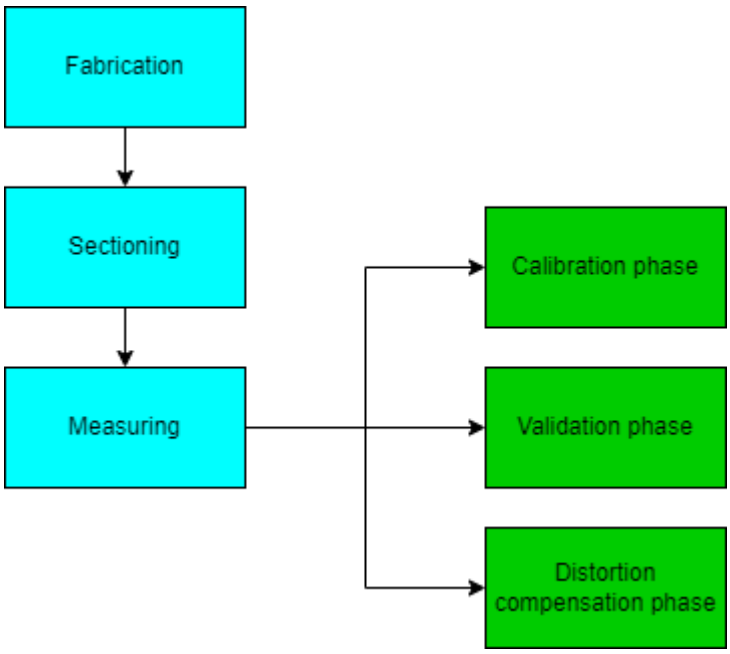

Figure 4-5-Sample fabrication process

The samples that will be fabricated for this study are two samples parallel to the X-axis, two samples parallel to the Y-axis, and two samples at an angle of $45°$ relative to the X and Y-axis. The samples that are fabricated parallel to the X and Y-axes will be used in the calibration phase, and the sample fabricated at an angle of $45°$ will be used for the validation phase of this study. Samples fabricated parallel to the X-axis has a hatching pattern horizontal to the X-axis. The blue line in Figure 4-6-A is a representation of the boundary of the sample that is fabricated, while the green lines in Figure 4-6-A indicate the direction the laser will follow while scanning each of the layers. The laser will start by scanning the boundary section of each component that is separate from the other. When the boundary is complete, the laser will then melt the powder enclosed by the boundary, following the scanning strategy that was set during the slicing process of the component. During the X hatching, the laser will start at the top or bottom of each section and scan the power inside of the boundary from right to left or from left to right. The Y hatching works on the same principle, but the scanning path (green lines) are vertical to the X-axis, as shown in Figure 4-6-B. The sample fabricated at a $45°$ angle will have a hatching pattern of $45°$ relative to the X-axis and Y-axis, as shown in Figure 4-6-C.

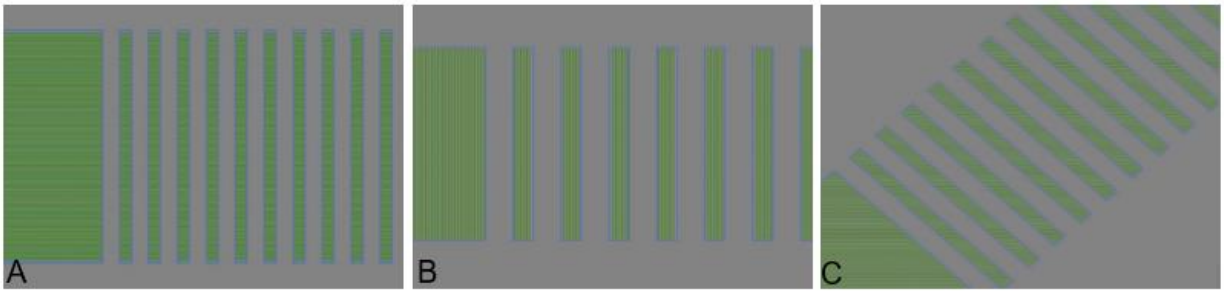

Figure 4-6-A-X hatching pattern, B-Y hatching pattern, C-45° hatching pattern

4.3.1 Sample parameters and process

The samples used in each of the phases of the study will be fabricated using the set parameters shown in Table 4-5. These parameters are set during the setup procedure of the model in the slicer program (OR suite).

Table 4-5-Sample fabrication parameters

Fabrication parameters	
Laser power	Boundary=112W Infill=104W
Beam expander	40µm
Scanning speed	630 mm/s
Layer height	25 µm
Powder feed rate	350%
Recoater speed	32mm/s
Chamber oxygen %	0.05%

The fabrication process can be seen in Figure 4-7. The process starts with the boundary of the component being scanned. After the boundary is scanned, the laser is moved to a point where it will melt the powder particles inside the boundary to complete the infill of the layer. As the layer is now completely scanned, the recoater process will start, and the next layer will be scanned. This process is then repeated until the component is fabricated and can be extracted from the machine for post-processing.

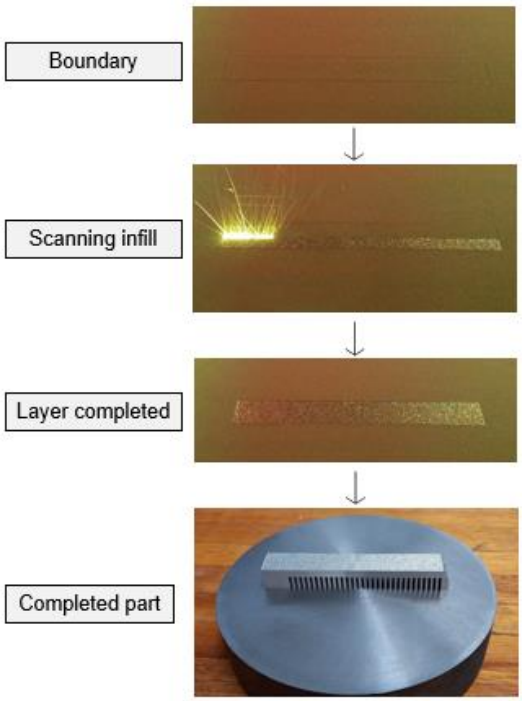

Figure 4-7-Printing process.

Note in Figure 4-8 shows clearly how the boundary of the sample is slightly elevated over the top face of the component. The reason for the perimeter elevation of the component is a result of different power settings that results in a different laser power density that is used when completing the melt track [77]. As seen in Table 4-5, the laser power used to scan the component boundary or perimeter is set to $112\ W$ while the laser power used for the infill is set to $104\ W$

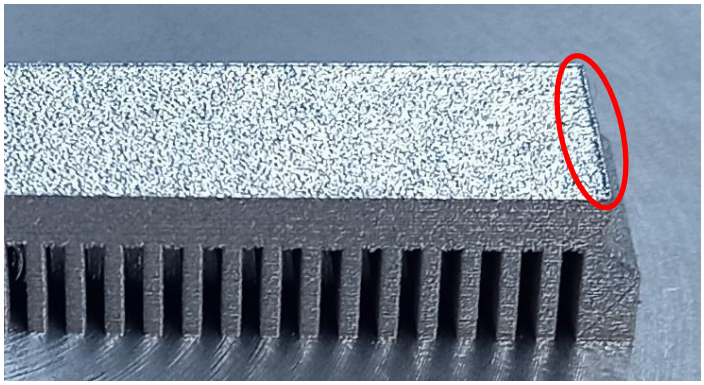

Figure 4-8-Elevated boundary section.

4.3.2 Sectioning of Components

A WEDM was used to partially cut the samples at the height of 2.9mm from the build plate. This method was used to section the components from the build plate as the sectioning process will

not thermally affect the component. If the part is sectioned with a process that increases the components' overall temperature, the mechanical properties of the sample can be affected, resulting in a potential decrease of residual stress that would occur, which will have an impact on the measured results. Figure 4-9 depicts the cutting process and setup for the calibration samples and validation samples. A jig was used to keep the part perpendicular to the cutting wire to ensure the cut line would be parallel to the build plate surface and perpendicular to the component. Figure 4-10 shows the component after the cutting phase with an evident distortion (right side of the figure) of the sample due to the residual stresses in the part being released due to the cut.

Figure 4-9-Wire electron discharge machine cutting phase.

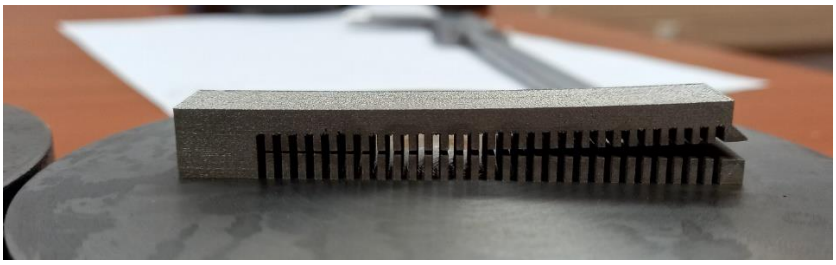

Figure 4-10- Calibration sample after cutting phase.

The calibration cantilever sample can be seen in Figure 4-11 with the cantilever on the left side in the Y-axis and on the right side of the figure the cantilever on the X-axis. By visually comparing the samples, the deformation of the sample printed in the X-axis was considerably more than that of the Y-axis sample.

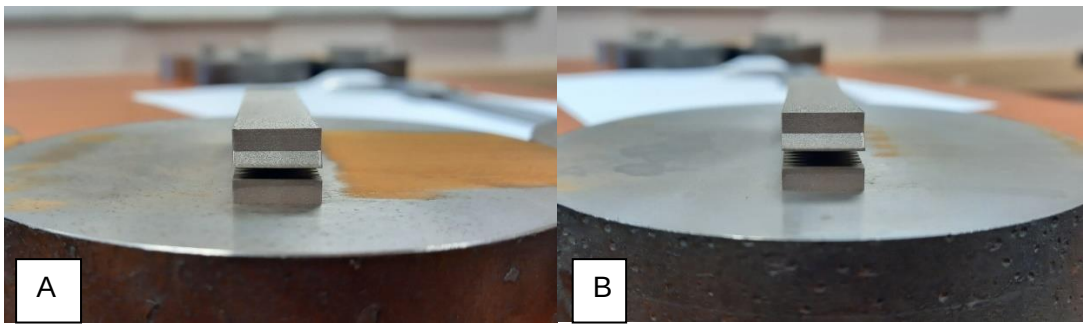

Figure 4-11-Calibration cantilever Y-axis sample (A) and X-axis sample(B).

4.3.3 Sample measuring.

The coordinate measuring machine (CMM) is a machine that uses a force triggered probe to measure the surface of a component. The sample is clamped into the workspace of the CMM to ensure the part is secure and stable during the measuring process. The process is controlled by a computer program that moves the measuring probe to set X, and Y coordinate in space then extends the probe in the direction of measuring until the probe is triggered when contact is made. The X, Y and Z coordinates are tabled, and the machine moves on to the following node that will be measured. Specification of the CMM machine used for this study can be found in Table 4-6.

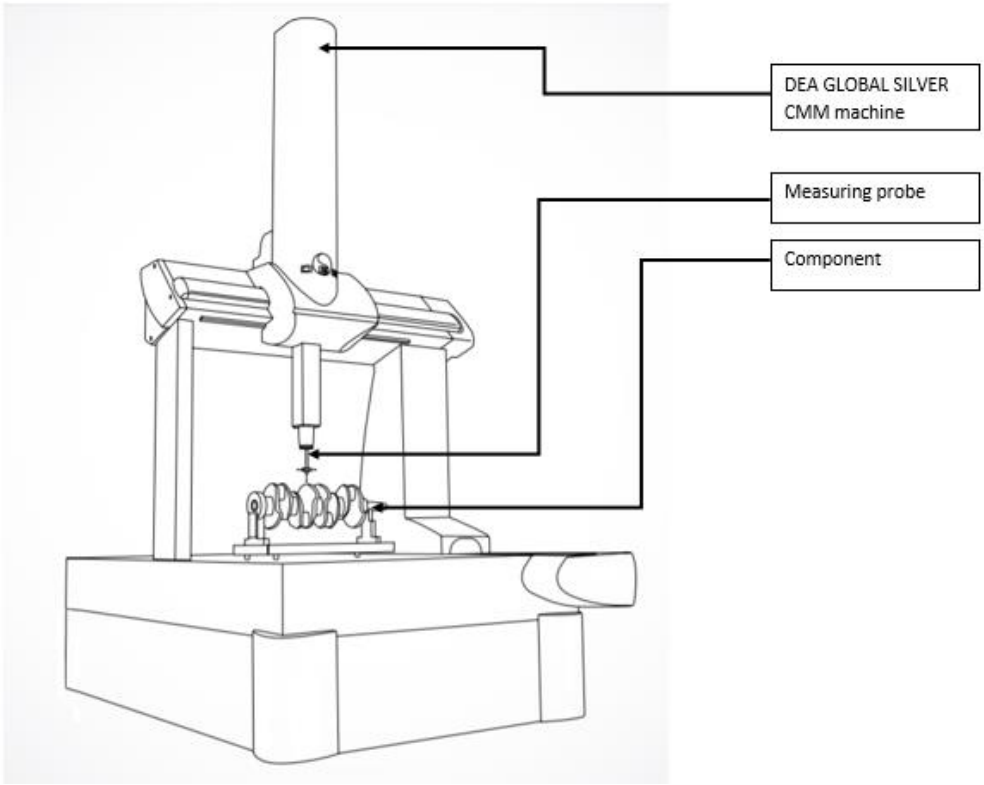

Figure 4-12-DEA GLOBAL SILVER. Adapted from Hexagon Datasheet [78]

Table 4-6-Machine specification [78]

Machine specifications	
Temperature compensation	CLIMA.
Performance environment	Standard:18-22 °C. CLIMA:16-26 °C.
Max scanning speed	500mm/s.
Performance data are valid if the following specifications are met.	Standard temperature range:18-22 °C. Max air temperature variation 1°C/h-2°C/24h. Max spatial gradient:1°C/m. CLIMA temperature range:16-22 °C. Max air temperature variation: 1°C/h-5°C/24h. Max spatial gradient: 1°C/m.
Probe configuration	TP200: Standard force module, stylus length 10mm, tip diameter 4mm.
Technical Characteristics	
Mechanical frame	X: Micromachined anodized light alloy extrusion. Y: Integral dovetail guideways, machined into the table. Z: Micromachined anodized light alloy extrusion.
Surface plate	Material: Granite; Part locking; threaded inserts M8 x 1.25; Flatness: according to DIN 876/III.
Sliding system	Air bearing on all axes.
Measuring system	METALLURGY linear scales. System Resolution:0.039 µm.
Temperature compensation	CLIMA: Multisensory temperature compensation technology, 16-26 °C.
Ram counterbalance	Pneumatic, adjustable.
Air supply	Minimum air supply pressure: 0.5 MPa Air consumption: 150Nl/min.
Environment	Metrological specification temperature range: Standard:18-22 °C and CLIMA: 16-26 °C Operating temperature: 10-40 °C Relative humidity:20%-90% non-condensing
Probe heads and sensors	HH-A, HH-AS8, HP-S-X1C, HPS-X5, TP200, HP-T, HP-TM, HPS-X1, HP-L-10.66

4.4 Simufact simulation setup procedure and Mesh independency

4.4.1 Simufact simulation setup procedure

Section 4.4.1 discusses the calibration and simulation setup procedure explaining the workflow and parameter setup during calibration or simulation when using Simufact. The setup of the calibration and simulation procedure consists of four main setup sections, the process setup, machine setup, manufacturing and optimisation setup, and the analysis and result setup. These setup sections must be set at the start of any calibration or simulation procedure. The flow diagrams in Figure 4-13 to Figure 4-16 shows the procedure flow and minimum parameters that have to be set.

4.4.2 Process setup

The process setup section in Figure 4-13 sets the simulation configuration, type of simulation and the different manufacturing stages in the process.

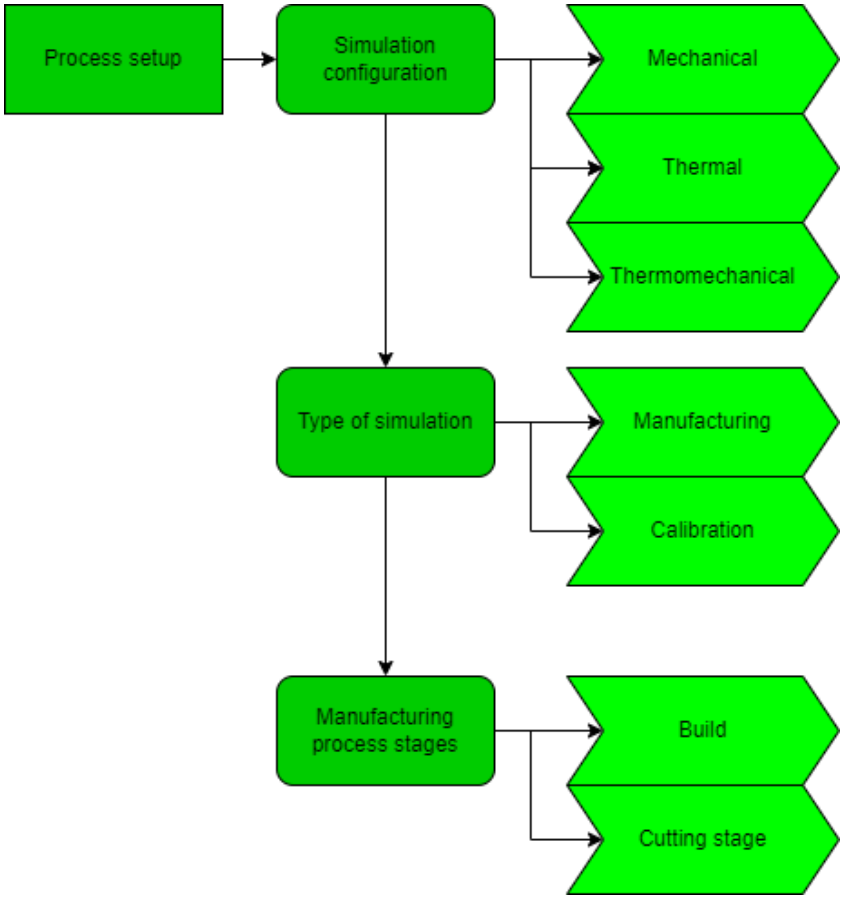

Figure 4-13-Process setup of a simulation procedure

4.4.3 Machine setup

The machine setup section in Figure 4-14 sets the machine properties and handles the part importation, support structure, material configuration, and base plate configuration.

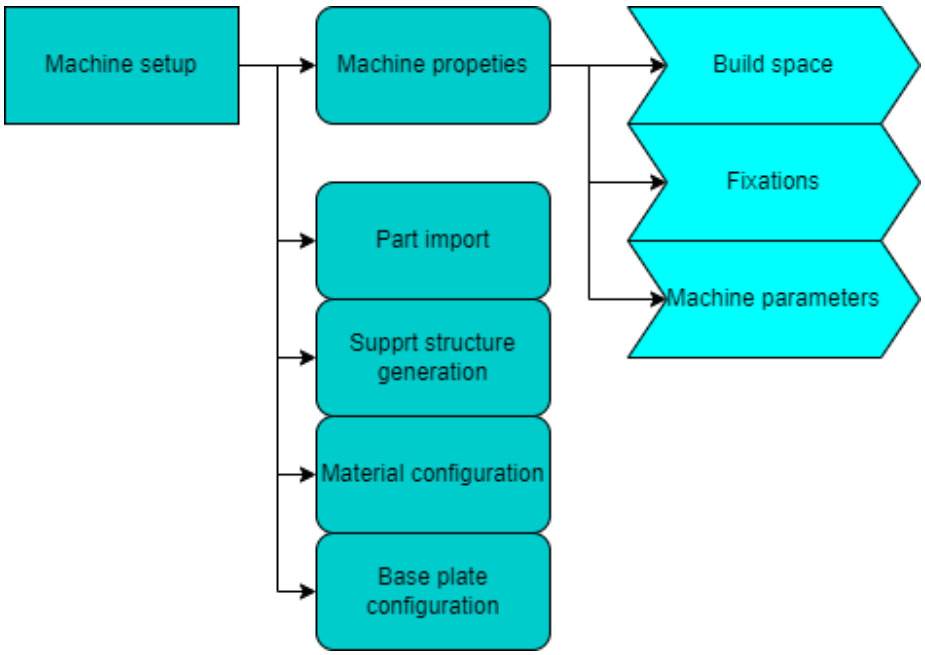

Figure 4-14-Machine setup of a simulation procedure

4.4.4 Manufacturing and optimisation setup

The manufacturing and optimisation section, shown in Figure 4-15, sets all the build parameters, calibration and measuring point parameters and properties of each of the manufacturing stages, such as the cutting stage.

Figure 4-15-Manufacturing and optimisation setup of a simulation procedure

4.4.5 Analysis and result setup

The final stage is the analysis stage, see Figure 4-16, where the surface mesh, voxel mesh, volume mesh and the numerical parameters are set for the calibration or simulation. After all these parameters are set, the simulation or calibration can commence.

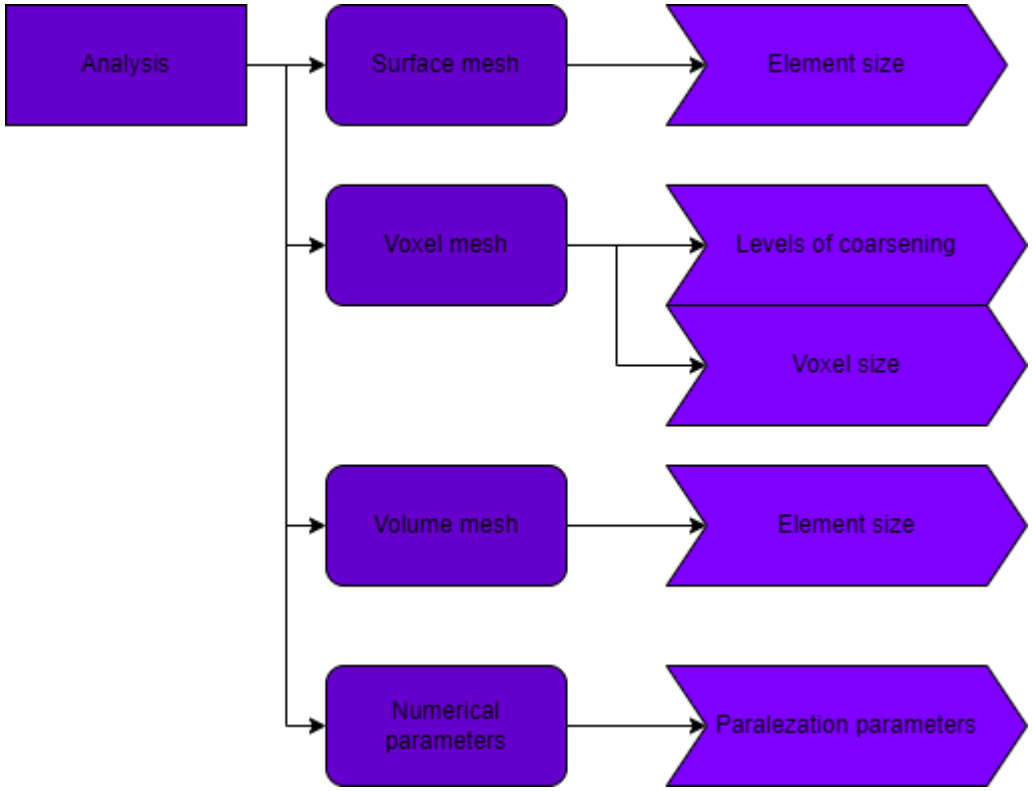

Figure 4-16-Analysis setup of a simulation procedure

4.4.6 Mesh independency

For Simufact to solve and calculate the related stresses, strains, and displacements of a component, the FE and ISM approach is used during the calibration and simulation phases. These methods are initiated by using a combination of the voxel, surface and volume mesh to discretize the component. Generalising the dictating rules of FEM, it is known from the literature that when the distance between the nodal points of the mesh has decreased, the accuracy of the calculated results of the FE model will increase, resulting in a more accurate approximation of the deformation and the stress response of the component [79]. The direct proportional correlation between the mesh size and the accuracy of the results achieved also correlates with the amount of time and computational cost the simulation will need to complete. Thus, by decreasing the mesh size, the time to solve each iteration of the simulation will increase. It is therefore essential

to find a value for the mesh size that will deliver the results where the computational expense and the accuracy of the model are in equilibrium with one another. The independency test will use a voxel element size of $0.25mm$, $0.5mm$, and $1mm$ to investigate the effect of the voxel element size on the accuracy of the predicted deformation results.

Figure 4-17 shows the mesh applied to the component at different voxel sizes ranging from $0.008mm^3$ per cube to $1mm^3$ per cube. As the cube volume of each voxel element decreases, the number of nodal points that connect each of the voxel elements on the components exponentially increases, as shown by Figure 4-18.

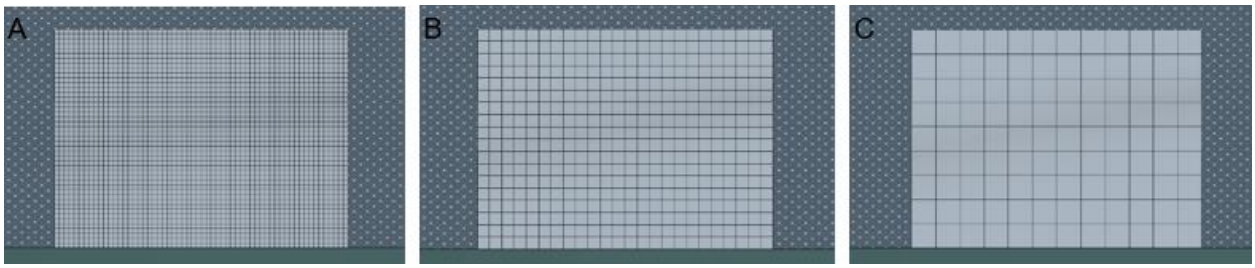

Figure 4-17-Voxel sizes (A-0.2mm, B-0.5mm, C-1mm)

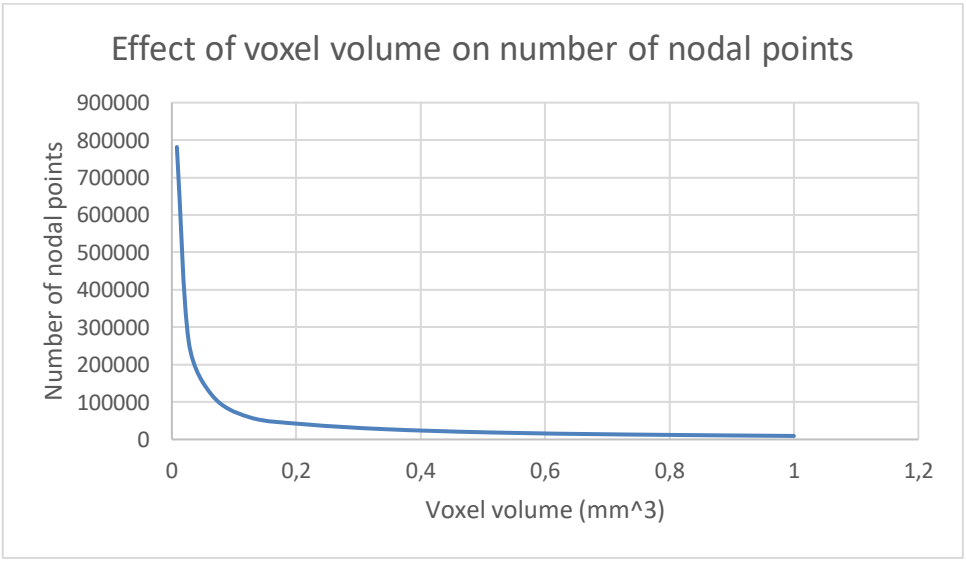

Figure 4-18-Effect of voxel volume on the number of nodal points.

4.4.6.1 Influence of voxel size on the volume fraction variable

The volume mesh used for the calculation in the FE analysis has a cuboidal shape which represents the voxel elements volume and, in turn, represent a section of the volume of the component that is simulated. As the surface geometry of many components will have angled and curved geometries, some intersecting voxel elements will have a volume fraction that is less than 100%. Decreasing the volume of the voxel element will ensure a closer approximation of the surface geometry of the component by increasing the volume fraction per voxel element used in the simulations. Figure 4-19 and Figure 4-20 are visual representations of the volume fraction influence of the FE model. As seen in Figure 4-19, the voxel size of the elements is set to $0.25mm$ and Figure 4-20 set to $0.9mm$. The voxel elements represented in red indicate a volume fraction higher that 98% per voxel element. As the volume fraction of the element decreases the accuracy of the approximation to the FE model will proportionally decrease.

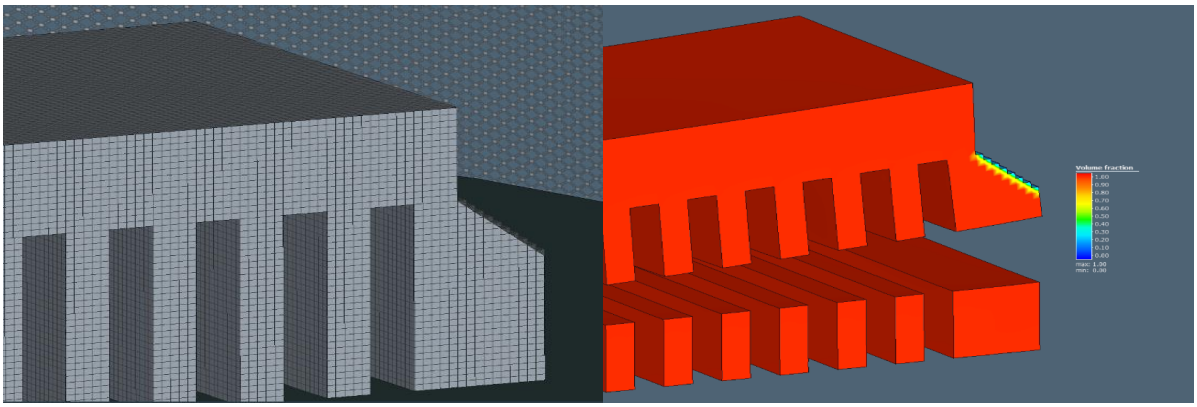

Figure 4-19-A-Voxel cube 0.25mm intersections B-Volume fraction 0.25mm intersections

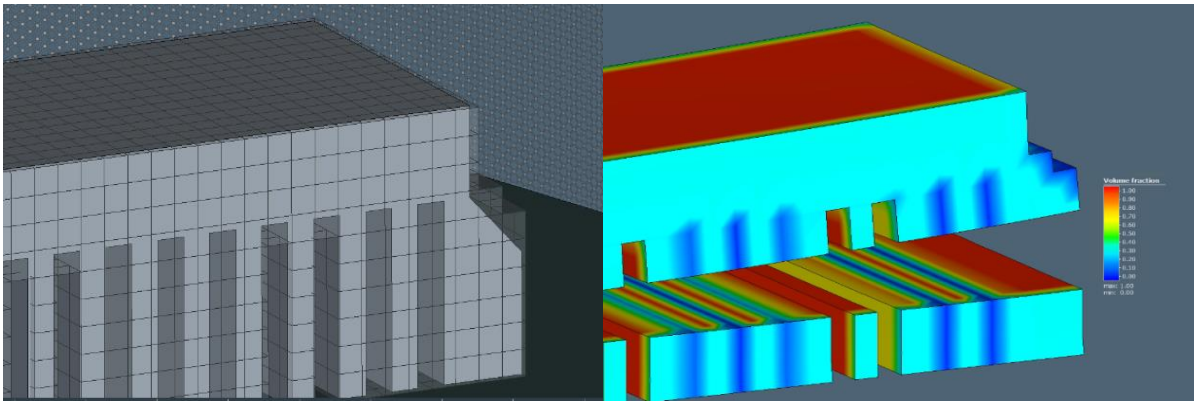

Figure 4-20-A-Voxel cube 0.9mm intersections B-Volume fraction 0.9mm intersections

4.5 Calibration phase

For the investigation of deformation prediction and compensation, a detailed calibration[6] of the machine and the software must be completed to ensure accurate and repeatable results. For the calibration phase, Simufact makes use of the ISM to calculate the deformation of the component numerically. The Inherent strains can be explained as process equivalent mechanical loads. The inherent strains that are present in the component can give insight into the material and mechanical properties of the component that was fabricated. By using the ISM, the calculation complexity of the system is reduced while still resulting in accurate strain and deformation results [59]. Figure 4-21 shows how each of the variables in the simulation will interact with the properties that connect the ISM with the calibration phases and the simulation phases. The material properties consist of the mechanical properties, thermal properties and microstructure of the component forming the material properties of the simulation. Parameters such as the laser power, hatching strategy and laser speed will represent the process parameters of the simulation. The material properties and process parameters will influence the thermal strains, plastic strains and phase transformation of the component during the simulation. The results of the simulation procedure will provide the outputs such as the stress, strains and distortion of the component during and after fabrication.

[6] A set of operations that will establish a relationship between the actual values resulting from the experiment and the predicted values resulting from the simulations. When the actual and theoretical values converge after altering certain conditions as need be the calibration is complete.[59]

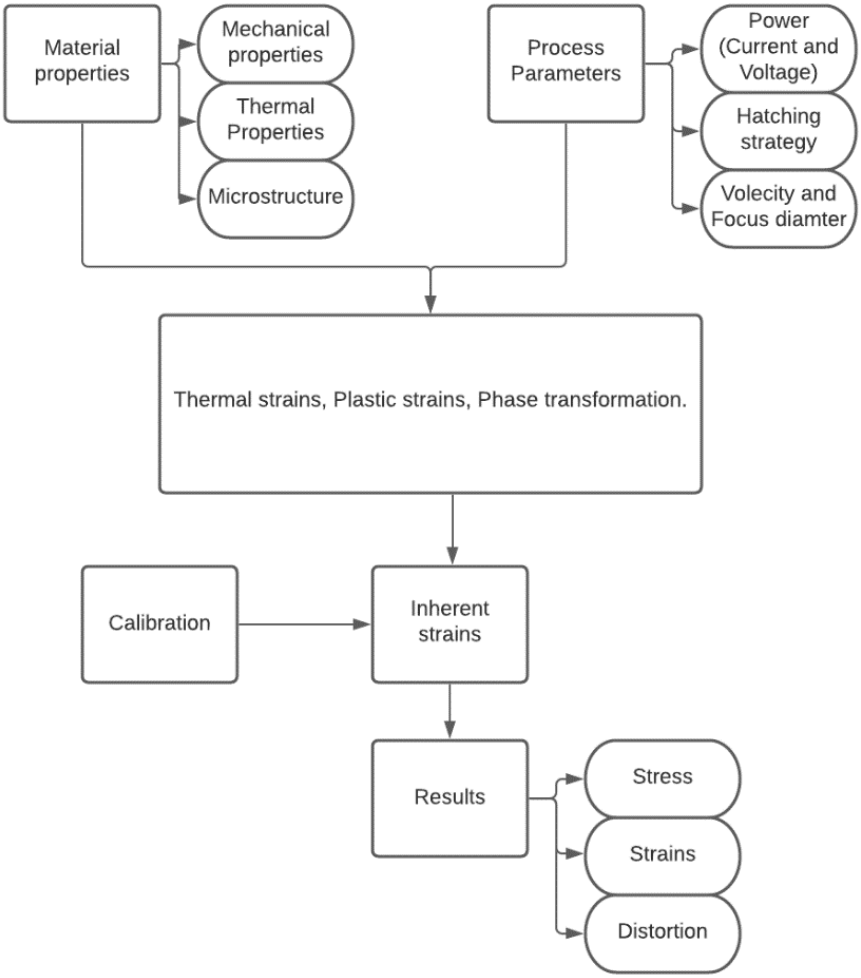

Figure 4-21-Calibration process using the inherent strain method (Adapted from Simufact additive tutorial 2020) [7]

4.5.1 Fabrication and process flow of samples used for the calibration phase

The calibration process starts by fabricating the prescribed cantilevers and partially cutting the components to induce deformation by mechanically reliving the stress that built up in the component during fabrication. This cutting process is completed to find the maximum Z-displacement of the component to calculate the inherent strains. Figure 4-22 A depicts the calibration sample before the cutting phase. The cutting plane, in Figure 4-22, is located 2.9mm from the top of the build plate. The sample will be sectioned from the front end, right side on Figure 4-22, 56.5mm inwards. By cutting the connection points to the build plate, the cantilever sample will deform due to the residual stress build up in the sample. The residual stress is a result of thermal and mechanical stress build-up in the part during fabrication. Figure 4-22 B depicts the calibration sample after the cutting phase is completed. As the part distorts, the internal stress in

the sample will decrease by deforming the component until an equilibrium is reached. After the sectioning phase of the calibration setup, samples will be measured with the use of a CMM machine to find the Z-displacement of each of the samples accurately. These displacements are then used as input variables in Simufact which in turn uses the ISM to calculate the Eigen strain tensors in each of the directions, X, Y, and Z. The calibration phase will enable Simufact to accurately predict the deformation of future components that are manufactured if CoCr powder hence all the parameters are kept constant. Changing the parameters of the machine will require a recalibration of the software to ensure accurate deformation and stress prediction.

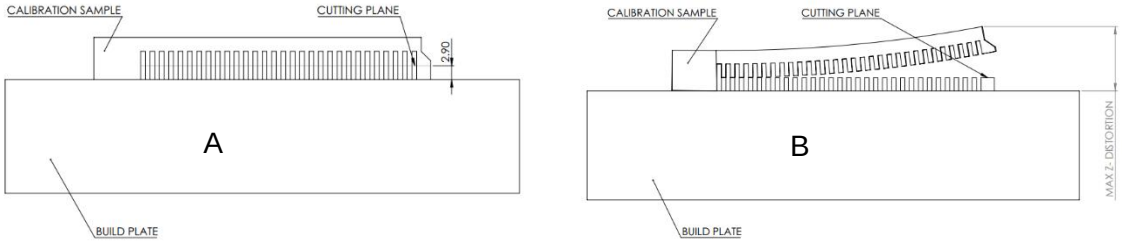

Figure 4-22-Calibration sample A- sample before section process, B- sample after sectioning process

4.5.2 Simufact calibration procedure

The Simufact calibration procedure aims to use the ISM to find values for the Eigen strain tensor that will satisfy the strain field of the system and enable a derivation of an equation to predict the deformation of the part. The ISM is used, as this method can be reversed to calculate the Eigen strain tensors from the deformation of the component. The calibration process was done in two sections, an isotropic calibration process and an orthotropic calibration process. These different procedures of calibration will be introduced to investigate the influence of the different methods on the Eigen strain tensor values and the accuracy of deformation prediction. The measuring points recorded from the deformed cantilever was converted into Cartesian coordinates that will represent the actual deformation of the cantilever in the coordinate domain used in Simufact. The isotropic and orthotropic calibration procedure works by setting the actual deformation of the cantilever equal to a target deformation in Simufact. The ISM algorithm then uses a guess value to determine an initial Eigen strain tensor value that will satisfy the deformation of the system. The iterative solving procedure then continues by using the Eigen strain tensor values calculated in the previous iteration as the new guess values for the system. This iterative process is then repeated until the predicted deformation of the cantilever converges with the actual measured deformation of the cantilever.

4.5.2.1 Isotropic and Orthotropic calibrations.

Once the system is calibrated with the use of isotropic calibration properties, the resulting Eigen strain tensor will only be in one direction as the isotropic properties will not be bounded by direction. Therefore, the Eigen strain tensor in the Y direction will be set equal to the Eigen strain tensor values in the X direction if the cantilever is oriented parallel to the X-axis. When the cantilever is oriented parallel to the Y-axis, the Eigen strain tensor in the X direction will be set to that of the Y-direction. This entails that the deformation will be dictated by one Eigen strain tensor throughout the whole system. The orthotropic calibration will take the strain direction into account when the calibration is done, calculating an Eigen strain tensor value for the X direction and the Y direction regardless of the strain direction.

- **Isotropic calibration process**

For the isotropic calibration process, a single cantilever component is placed on the build plate. During this calibration, the strain tensor in the X direction and the Y direction are equal to one another, which decreases the orientational influence on the deformation of the cantilever. The cantilever parts were printed explicitly at a fixed $0°$ angle for the X direction cantilever and a fixed $90°$ angle for the Y direction cantilever component.

Equation 4-1- Isotropic strain tensor.

$$\epsilon_{xx} = \epsilon_{yy}$$

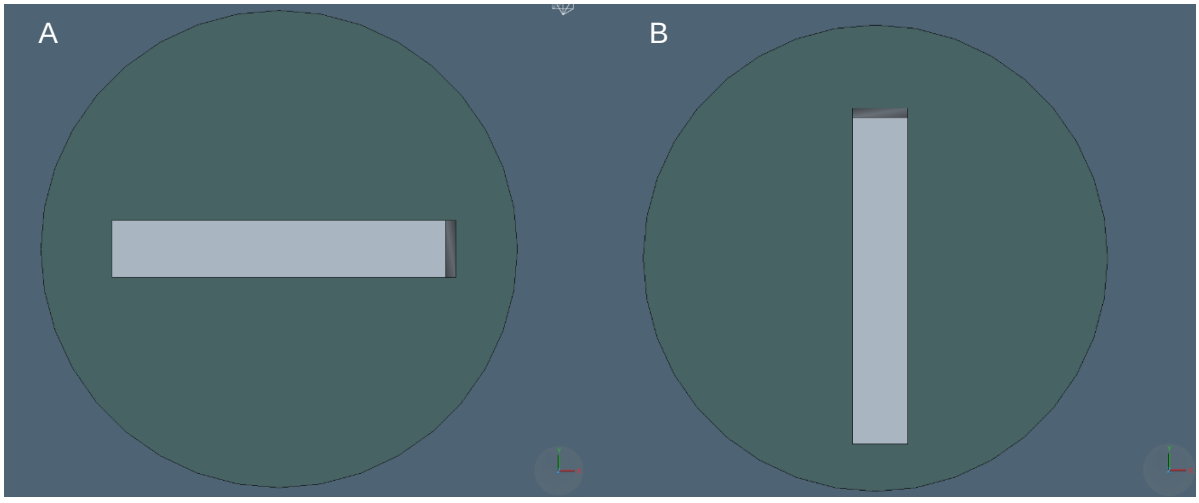

Figure 4-23-A-Isotropic calibration in the X direction and B- Isotropic calibration in the Y direction

- **Orthotropic calibration process**

The orthotropic calibration process was populated with two cantilever components, one in the X direction and one in the Y direction on the same build plate. Calibration in the X direction and Y direction simultaneously will result in an X strain tensor and a Y strain tensor which are unequal. With the Eigen strains in the X- direction and Y direction not equal to one another, the simulation will be able to predict whether or not a twisting distortion will be present due to the orientation and parameters used during the fabrication process.

Equation 4-2-Orthotropic strain tensors

$$\epsilon_{xx} \neq \epsilon_{yy}$$

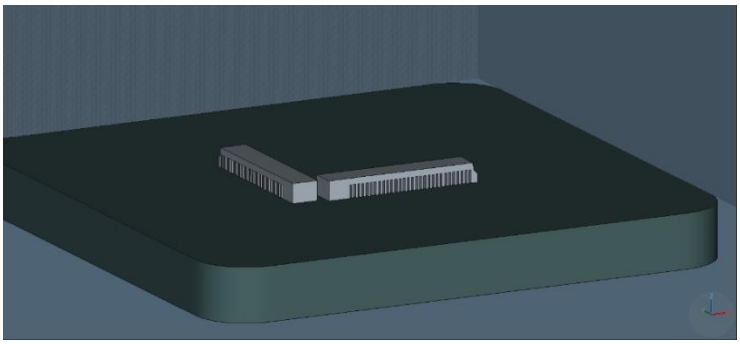

Figure 4-24-Orthotropic calibration in X and Y direction.

4.5.3 Calibration parameters

Parameters such as machine settings and feedstock material properties should be set accurately to represent the actual fabrication and lab conditions. Table 4-7 show the process parameters that will be used for the calibration phase in Simufact to represent the actual parameter of the experiments. The physical parameters such as the build space, number of lasers, and material properties are physical properties of the machine and the feedstock material that will be used and cannot be adjusted. In contrast, the speed and laser power are parameters that must correlate with the parameters that were set in the slicing program before the fabrication of the samples has commenced. These parameters are prescribed by Orlas for the OC AM machine process parameters.

Table 4-7-Calibration parameters.

Calibration parameters		
Machine Setting		
Build space	**Isotropic**	**Orthotropic**
X	250 mm	250 mm
Y	250 mm	250 mm
Z	250 mm	250 mm
Base plate shape	Rounded corners	Rounded corners
Machine parameters		
Number of lasers	1	
Max laser power	112W	W
Max laser speed	630	mm/s
Min recoater time	14,2	s
Material		
Name	CoCr powder	
Thermal properties		
Specific heat capacity	0,43	J/(gK)
Density	8300	kg/m^3
Dissipation factor	0,9	
Mechanical properties		
Poisson's ratio	0,3	
Thermal expansion factor	1,36E-15	1/K
Ultimate strain (A)	20	%
Yield strength	1060	MPa
Tensile strength	1350	MPa
Baseplate		
Material	E8 Machined steel	
Thickness	25	mm
Build parameters		
Layer thickness	0,025	mm

4.5.4 Target deformation measuring points

To ensure the measured values are as close as possible to the actual deformation values of the top plane measuring boundary was decreased by $1mm$ in the X and Y-axis. This was done to accommodate the elevated boundary of the part that is estimated at $120\ \mu m$ higher than the top plane of the cantilever. Figure 4-25 depict the coordinate grid that was used for the measuring points on all the samples. With the use of the measuring mesh, the top plane and deformation of each point were accurately measured while excluding the elevated boundary.

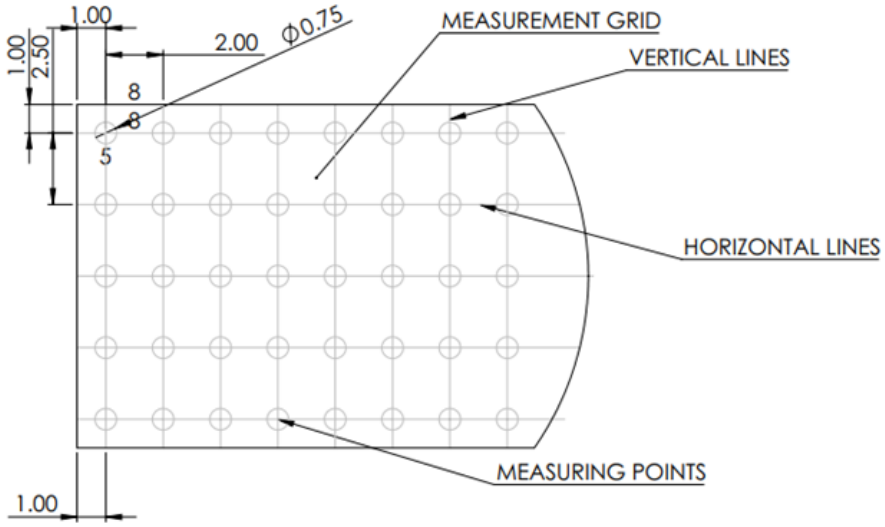

Figure 4-25-Measuring grid.

4.6 Validation phase

The results obtained from the calibration process must now be validated to ensure the values of the Eigen strain tensors will satisfy a general system and is not unique to the system used for the calibration phase. The validation process uses the cantilever beam printed at an angle of $45\ °$ relative to the X and the Y-axis. The Eigen strain tensors that were the output results of the calibration phase is now used as the input Eigen strain tensors for the system during the simulation phase and are used to predict the deformation that will occur in the component. This validation phase is performed to ensure the correct Eigen strain tensors are used throughout the simulation and deformation compensation phase. The components will be fabricated, sectioned, and the actual deformation of the components will be compared to the simulated deformation. The deformation of points corresponding to the measuring grid in Figure 4-25 in Section 4.5.4 will be compared to that of the deformation predicted from the simulation using the same coordinate system.

4.7 Deformation compensation phase

4.7.1 Simulation procedure

The procedure to simulate components can be described with the use of the flow chart in Figure 4-26. The process starts with the CAD data being imported into Simufact. After importation, the parameters are set, and the mesh generation process starts. During the mesh generation, the process parameters such as laser speed, and laser powder, are set, and the elemental size of the voxel mesh is set. The support structure boundary conditions are set, after which all constraints on the simulation must be met before executing the simulation. Additional cooling steps are present in the thermomechanical simulation to cool the component to the set cooled temperature in the parameter settings. A shape compensation procedure can be implemented on the component and re-stimulated for better results regarding the part distortion and stress distribution in the part. Alternatively, the results of the simulation, such as the STL file or ARC file, can be exported for any further analysis or simulations.

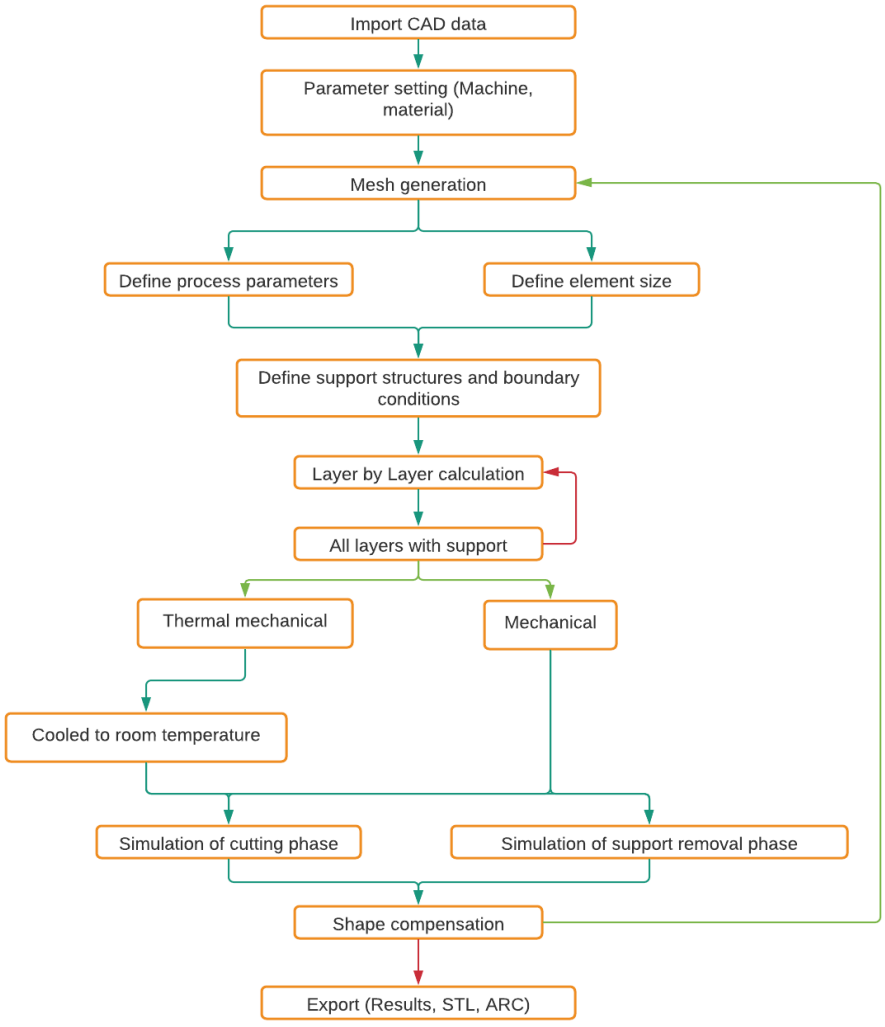

Figure 4-26-Simulation procedure adapted from [80]

4.7.2 Distortion compensation

During the deformation phase, a complex geometry part with sections in the X, Y and $45\,°$ relative to the X and Y axis will be simulated. The original geometry of the component is used in Simufact as the reference geometry, and the results of the simulation, which will be the distortion of the part, is then used in an iterative process. This iterative process alters the geometry of the part to compensate for the distortion of the part to increase the geometric accuracy of the component. If this optimisation process is successful, the result will be a decrease in the distortion and an increase in the absolute dimensional accuracy of the component directly after fabrication and sectioning from the build plate.

CHAPTER 5

RESULTS AND DISCUSSION

5.1 Introduction

This chapter aims to provide insight into the results obtained from the experimental procedures that were used in this study. After which, the surface measuring results of the calibration samples will be discussed, and the influence that the orientation of the component will have on the deformation and residual stress in the part. The following section will discuss the results of the mesh independency phase, calibration phase, and validation phase and the different parameters and variable that influences the deformation and stress build up in component during fabrication. The closing section of Chapter 5 will be a detailed discussion about the results and influencing variables that play a role during the distortion compensation phase of this study.

5.2 Calibration sample fabrication phase

The manufactured cantilever samples' top planes were measured with the use of a CMM machine by following the method given in Section 4.2 to evaluate each of the cantilevers' top plane deformation and tip displacement. The tip displacement was needed in Simufact as a calibration parameter that served as a displacement target during the iterative calibration process.

5.2.1 Calibration samples

The calibration samples that were fabricated parallel to the X-axis and the Y-axis, respectively, as seen in Figure 5-1. Figure 5-1 is a visual representation of the top plane of each of the cantilevers with respect to the total deformation of the cantilevers.

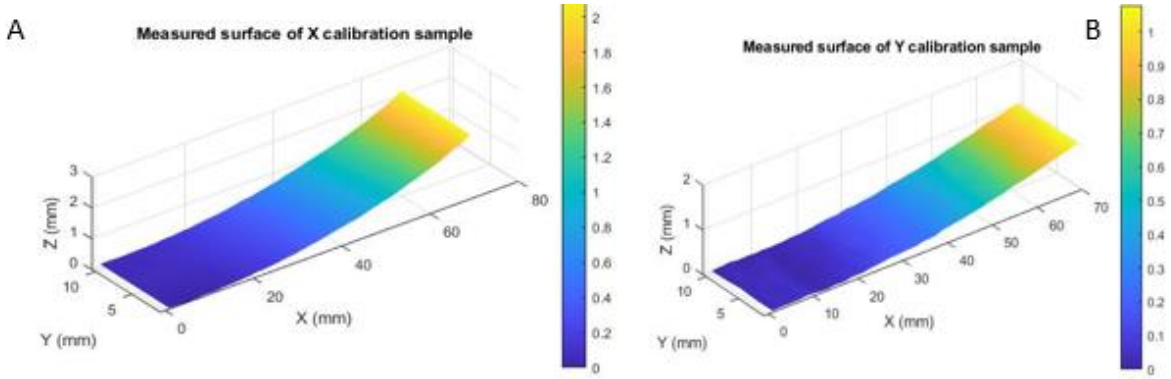

Figure 5-1-A-Top plane of cantilever fabricated parallel to the X-axis; B-Top plane of cantilever fabricated parallel to the Y-axis

Table 5-1 and Table 5-2 is a numeric indication of the deformation experienced by the sample. In the tables, the Px variable represents the point name referring to the measuring grid in Figure 4-25, while the X, Y, and Z columns represent the coordinates of each of the measuring points. The deformation experienced by the sample fabricated in the X-axis was relatively more prominent than that of the sample printed parallel to the Y-axis. The deformation the sample experienced was, on average, $9\ \%$ larger than the sample fabricated in the Y-axis. This is because of the shorter scan length of the melt tracks that formed the Y-axis cantilever hatching strategy, as seen in Figure 4-6 B. The Z_{target} the column shows the total deformation of the tip on the 5 selected points that are used in the calibration phase.The distortion of the measuring points was measured using the top plane of the build plate as a reference point. The target deformation points were then calculated by using the Original CAD cantilever as a reference which is nine mm from the top plane of the build plate.

Table 5-1-Tip deformation of X-axis calibration sample

Tip Deformation				
Placement	**X**	**Y**	**Z**	**Z_Target**
P35	69,0021	1,00162	10,87477	1,874775
P70	69,0026	3,50147	10,89967	1,899673
P105	69,00262	6,00146	10,89165	1,891653
P140	69,00291	8,50168	10,91281	1,912808
P175	69,00264	11,0016	10,92335	1,923345

Table 5-2-Tip deformation of Y-axis calibration sample

Tip Deformation				
Placement	**X**	**Y**	**Z**	**Z_Target**
P35	69,00007	1,00125	10,00227	1,002272
P70	69,00011	3,50126	10,00337	1,003369
P105	69,00012	6,00099	10,01913	1,019134
P140	69,00033	8,50132	10,05464	1,054641
P175	69,00017	11,0013	10,05486	1,054859

Figure 5-2 shows the validation samples' top plane. The sample was fabricated at 45° relative to the X-axis and Y-axis. As seen, the far tip of the sample shows significant deformation after sectioning as a result of the scanning pattern influence on the sample.

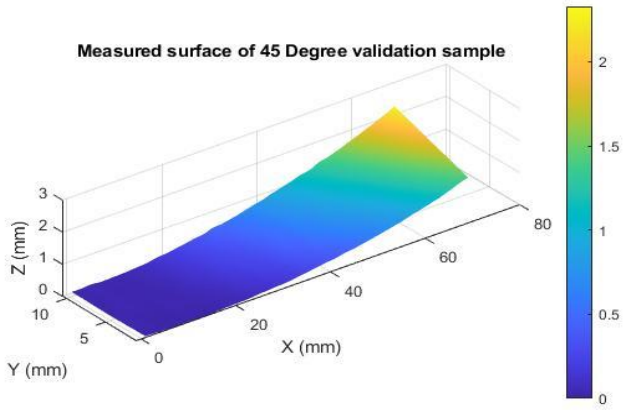

Figure 5-2-Sample printed at 45 degrees relative to the X and Y-axis

Table 5-3 shows the tip deformation of the sample that was used in Simufact as the validation target deformation. If the simulated deformation correlates with the 45° sample deformation, the Eigen strain tensor values calculated in the calibration phase can be used for accurate and repeatable deformation prediction simulations.

Table 5-3-Tip deformation of 45 Degree validation sample

Tip Deformation				
Placement	**X**	**Y**	**Z**	**Z_Target**
P35	69,00085	1,00226	10,21308	1,213078
P70	69,00072	3,50244	10,44808	1,448076
P105	69,00143	6,0024	10,6589	1,658899
P140	69,00197	8,50254	10,86642	1,866419
P175	69,00317	11,0028	11,1228	2,122797

The twisting deformation of the top plane of the cantilever showed a linear correlation, and this twisting effect was increased as the rotational angle of the top plane, and the X-axis increased. Where the maximum points of twist were at 45° relative to the X-axis. When this angle is further increased, the twist effect is decreased until the top plane is parallel to the Y-axis. As seen in Table 5-4.

Table 5-4-Slope of twist relative to the axis

Slope calculations of top plate twist					
X-Cantilever		**Y-Cantilever**		**45-Degree-Cantilever**	
X Points	**Zpoints**	**X Points**	**Zpoints**	**X Points**	**Zpoints**
1	1,8947745	1	1,002272	1	1,2130775
2	1,8996725	2	1,003369	2	1,4480755
3	1,891653	3	1,019134	3	1,658899
4	1,912808	4	1,054641	4	1,8664185
5	1,923345	5	1,054859	5	2,122797
X-Slope	0,00702765	**Y-Slope**	0,0156446	**45-D-Slope**	0,2237782

5.2.2 Mesh independency

Simufact uses a combination of voxel and surface meshing to ensure that geometric coverage exists between the component and the overlaying mesh. The cuboidal shape of the voxel elements used in the FE model can influence the approximation accuracy of the calibration and simulation phases. As the calibration phase is essential to the distortion compensation method, a mesh size was found that renders a good balance between the computational time expenditure and accuracy of results. The mesh independence investigation was divided into two sections, the one section investigating the influence of the voxel size during the calibration phase and the other investigating the influence of the voxel size during the simulation phase. The calibration and simulation processes use three main variables during the calculations. The calibration phase sets the voxel mesh and the distortion of the component to known variables and calculates the Eigen strain tensors as output. On the other hand, the simulation phases set the voxel mesh, and the Eigen strains tensor values to a known variable, as these values were calculated in the calibration phase, and calculate the deformation of the component as output. The difference between the variables is the weight of influence each of the variables has in the different processes. For example, changing the deformation in the calibration will have a relatively small effect on the resulting Eigen strain tensors, but by changing the Eigen strain tensors values in a simulation with

a relatively small degree, the impact on the predicted deformation of the component will be more prominent. It is, therefore, necessary to investigate the mesh independence of each process.

5.2.2.1 Calibration mesh independency

The calibration mesh independency phase investigated the effect of the volume fraction correlating to the different voxel element sizes ranging from $0.25mm$ to $1mm$ on the resulting Eigen strain tensor value calculations.

5.2.2.1.1 Influence of voxel size on the time to complete a simulation.

Different voxel size elements were simulated to investigate how the size variable will affect the time needed for each of the simulations to complete. As seen in Figure 5-3, when the size of the voxel elements is decreased, the total computational time needed for the simulation increases exponentially as the number of nodal points is increased exponentially.

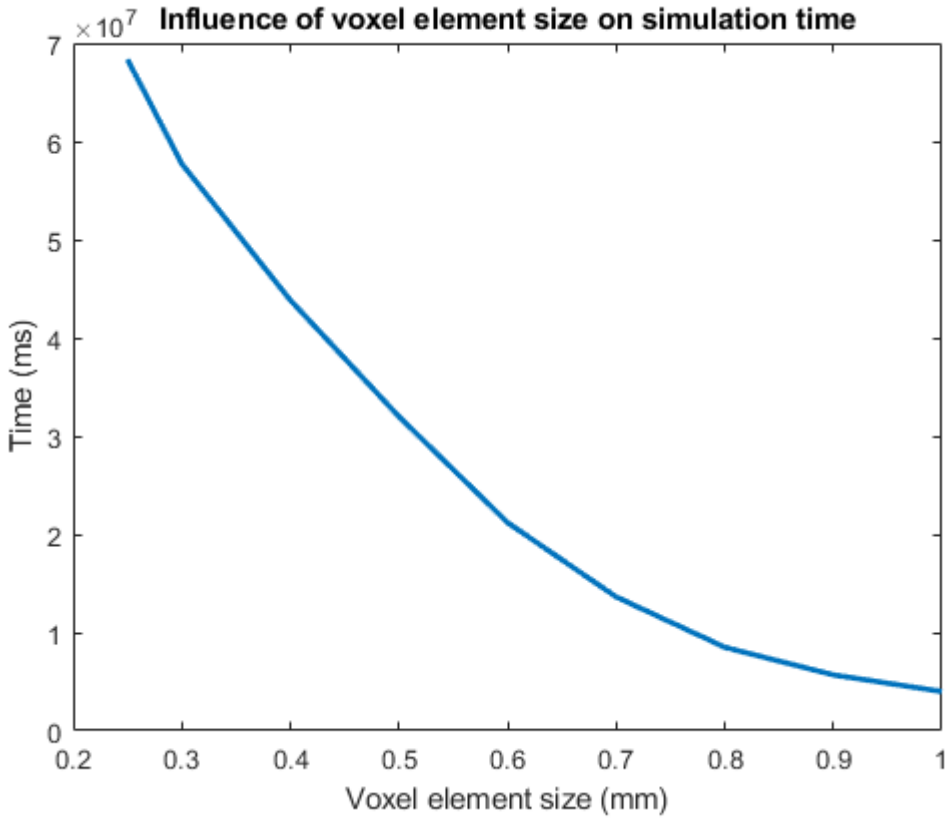

Figure 5-3- Influence of element size on the time to complete the simulation

5.2.2.1.2 Influence of voxel element size on volume fraction.

To investigate the correlation between the voxel element size, the volume fraction, and the accuracy of the predicted deformation as a result of the calculated Eigen strain tensor values.

Figure 5-4 shows the correlation between the voxel element size and the volume fraction variable that correlated to the geometry of the component. The volume fraction variable is calculated using the surface mesh on the component as the internal voxel elements will have a volume fraction of 100% and can be neglected from the calculation. As the voxel element size decreases, a trend becomes visible, suggesting that a decrease of voxel element size will lead to an increase in the volume fraction of the system and as the volume fraction increase, the accuracy approximation increases.

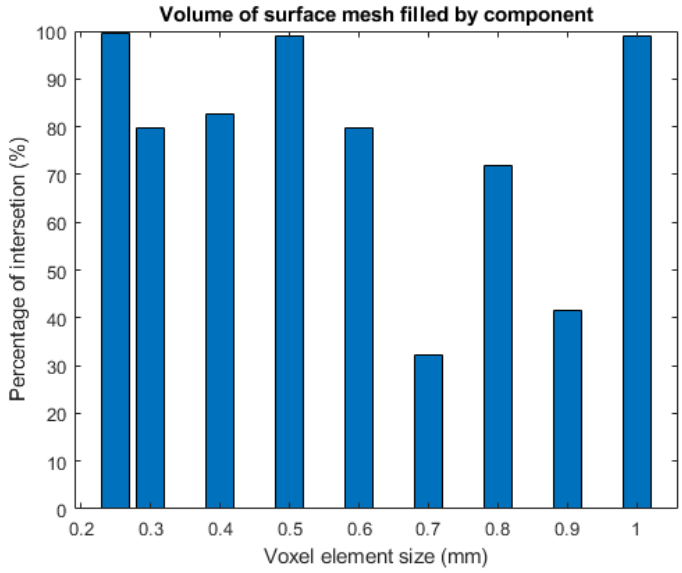

Figure 5-4-Surface mesh volume fraction of different element sizes.

5.2.2.1.3 Influence of voxel size and volume fraction on the predicted deformation

By varying the voxel element size during the calibration, a resulting Eigen strain tensor was calculated. These Eigen strain tensor values were then used in a simulation with a constant voxel element size. This was done to investigate how the voxel size and corresponding volume fraction will influence the accuracy of the predicted deformation resulting from the corresponding calculated Eigen strain value during the calibration phase. Figure 5-5 shows the predicted deformation resulting from each simulation with varying voxel size elements. As the voxel element size decreases, the predicted deformation resulting from the calculated Eigen strain tensor value approximates a more accurate representation of the actual measured deformation. The mesh independency threshold is visible at a voxel element size of $0.6mm$ as the error in predicted deformation is much higher when considering a voxel size of $0.7mm$ to $1mm$. This result indicates that the accuracy of the resulting data calculated during the calibration phase is depended on the voxel element size of the mesh used for the calculation of the Eigen strain tensor values.

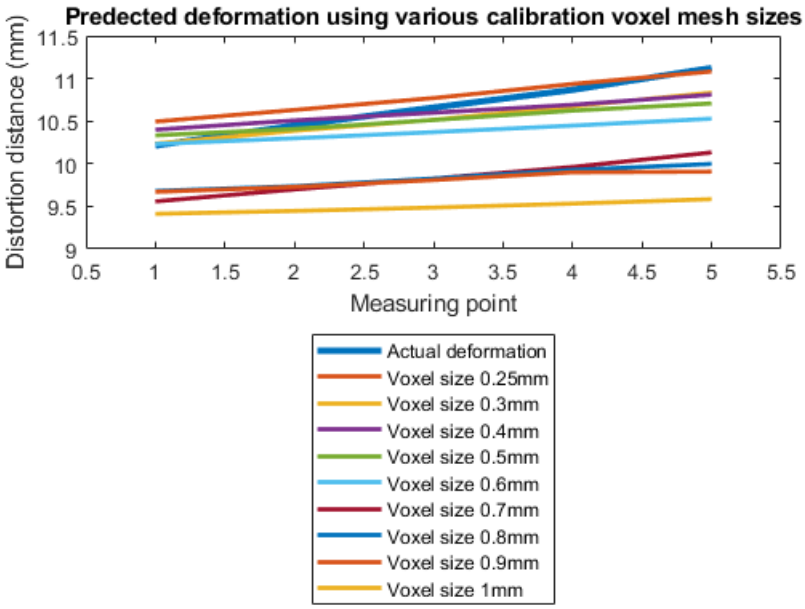

Figure 5-5-Influence of voxel size on the predicted deformation results

The voxel element size that resulted in a reasonable balance accuracy and computational time for the calibration phase was a voxel element size of $0.5mm$ for the geometry that was used during the calibration phase. Table 5-5 shows a summary of the calibration properties that resulted with the use of voxel element size of $0.5mm$ during the calibration.

Table 5-5-Voxel mesh independency testing results of the optimum configuration and balance of voxel size and time

Voxel Mesh Size	0,5
Voxel mesh volume	0,125
Voxels	44208
Nodal points	59125
Estimation value	
$\boldsymbol{\varepsilon_{xx}}$	-0,00302
$\boldsymbol{\varepsilon_{yy}}$	-0,00135
$\boldsymbol{\varepsilon_{zz}}$	-0,03
Steps	200
Calibration result	
$\boldsymbol{\varepsilon_{xx}}$	-0,00324
$\boldsymbol{\varepsilon_{yy}}$	-0,00144
$\boldsymbol{\varepsilon_{zz}}$	-0,03000
Steps	200
Error in predicted deformation and target deformation	
Point 1	2,2616 %
Point 2	0,745116 %
Total time (h: m: s)	08:22:44

Appendix A Table A 1 shows the results of each of the Eigen strain tensors values of the respective calibrations after alternating voxel mesh size.

5.2.2.2 Simulation mesh independency

From the calibration mesh independency investigation, the effect of the voxel element size is clearly shown in the accuracy of the calculated Eigen strain values. For the simulation mesh independency phase, the resulting Eigen strain values calculated with a calibration voxel mesh size of $0.25mm$, $0.5mm$ and $1mm$ was used to investigate the influence of the voxel element size on the accuracy of deformation prediction during the simulation. These Eigen strain tensor values were chosen as the values represent a wide range of calculated Eigen strain tensor values. During the simulation mesh independency phase, the voxel element size comprised for $0.25mm$, $0.5mm$, and $1mm$ elements. Figure 5-6 shows how the voxel mesh size influences the accuracy of the deformation prediction. The correlation shows that decreasing the element size used for the simulation will result in a more accurate prediction of the deformation of the component. The influence of the voxel size on the deformation will decrease as the voxel size decrease leading to a more accurate approximation of the deformation. There still exists a voxel element size threshold that must be crossed during the calibration phase, as seen in Figure 5-6. The alteration of the voxel element size during the simulation (that used the Eigen strain tensors that resulted from n calibration with a $1mm$ voxel element size) had little effect on the deformation prediction accuracy. All simulation error deviations can be found in Appendix A Table A 2. Considering the influence of the voxel size on the resulting data and computation expense, a voxel size of $< 0.5mm$ during the simulation phase will be adequate for this study.

This leads to the conclusion that if the voxel element size is not within reasonable size, that being smaller than $0.6mm$ during the calibration phase, decreasing the voxel element size during the simulation phase will not yield more accurate results. That being said, decreasing the voxel element size for simulation that did use Eigen strain tensor value that resulted from a calibration phase with the appropriate voxel element size will increase the accuracy of the predicted deformation.

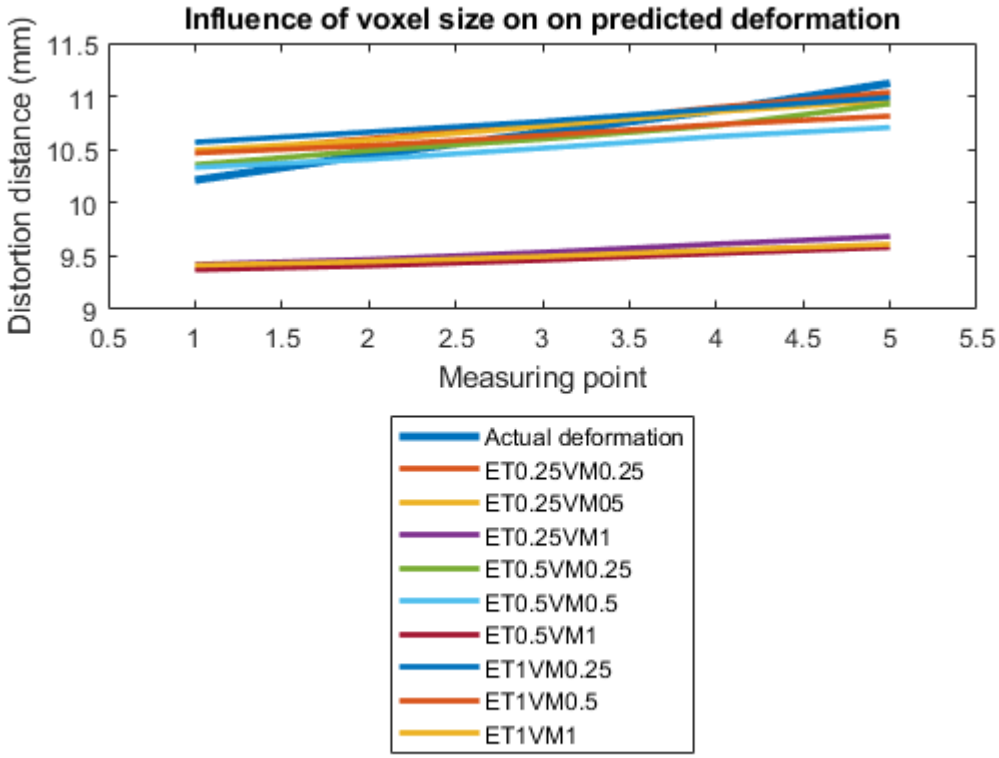

Figure 5-6- Influence of voxel size on deformation prediction data. ET refers to the Eigen strain tensor that resulted from the calibration with differentiating mesh sizes of 0.25mm,0.5mm,1mm. VM refers to the Voxel mesh size used for the simulation differentiating between a voxel mesh size of 0.25mm,0.5mm, and 1mm

5.3 Calibration phase

During the calibration phase of the software and the machine, the influence of three variables was investigated. This included the impact of the different calibration processes, namely the orthotropic double cantilever (ODC) and orthotropic single cantilever calibration process (OSC)[7], the effect of adding a third Eigen strain tensor in the Z-direction (Z-calibration), and the number of points that represent the targeted deformation during the calibration process. As seen in Figure 5-7, the two different scenarios are present where a single cantilever and a double cantilever is placed on the build plate respectively and fabricated.

[7] The isotropic calibration was excluded as the Eigen strain tensors resulting from an AM process is direction sensitive as the mechanical properties of the fabricated component will be influenced by the direction and orientation during the build process.

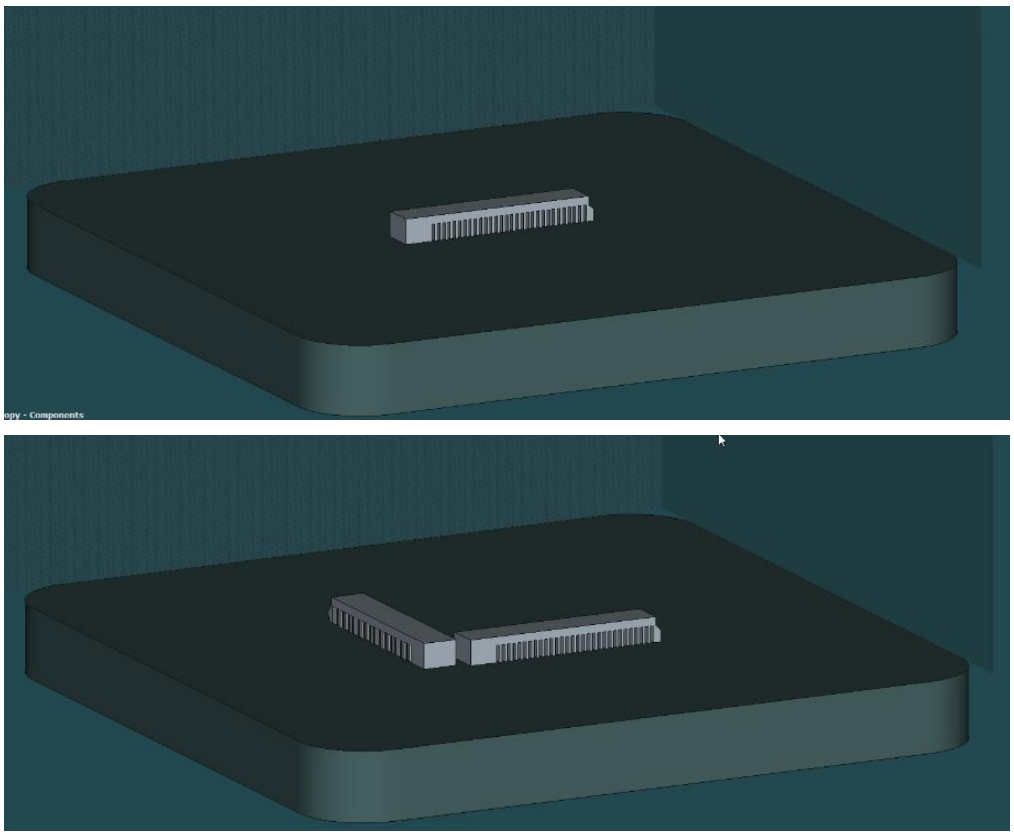

Figure 5-7-A- The single orthotropic cantilever process (OSC), B- The double orthotropic cantilever process (ODC)

The ODC and the OSC were further divided into two subjection calibration processes. One subsection calibrating Eigen strains tensors for the X-strain, Y-strain, and Z-strain ($\epsilon_{xx}, \epsilon_{yy}, \epsilon_{zz}$)(Z-calibration) and the other only calibration the X- strain and Y-strain ($\epsilon_{xx}, \epsilon_{yy}$) Eigen strain tensors. Lastly, the influence of the number of points was investigated by subdividing the calibration process into four scenarios. Single cantilever simulation (SCS) and double cantilever simulation (DCS), SCS1 and DCS1 only consider the average deformation measured over the total tip displacement, SCS2 and DCS2 consider the outermost points, SCS3 and DCS3 consider both the outermost points and the centre point, SCS4 and DCS4 consider all five measuring points. A visual representation of the measuring points can be seen in Figure 5-8 and Figure 5-9.

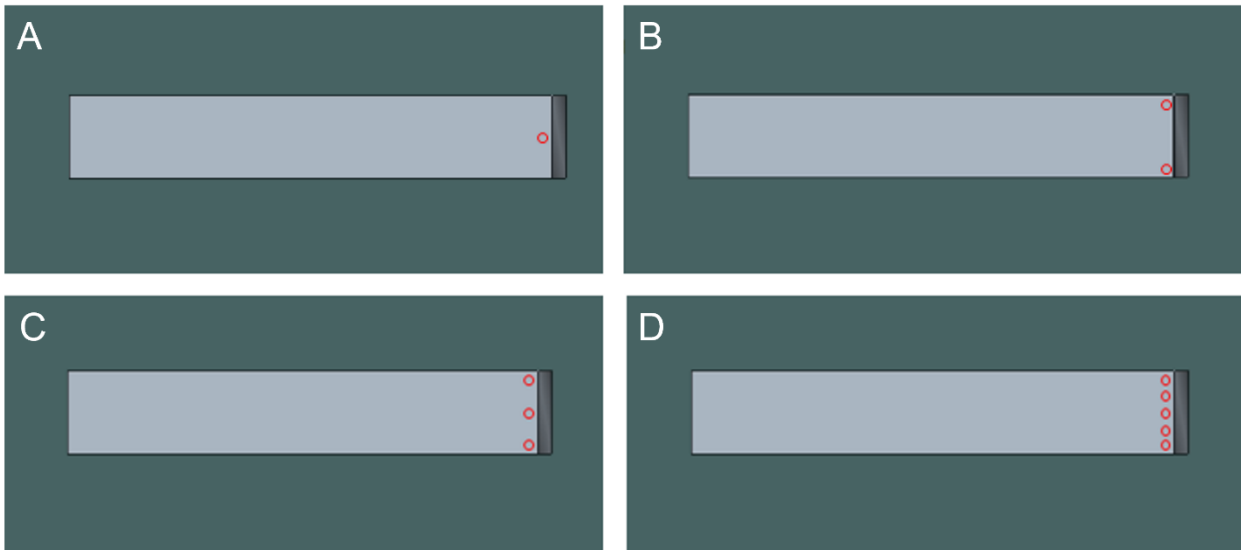

Figure 5-8- Measuring points used in OSC calibration simulations A- OSC1, B- OSC2, C- OSC 3, D- OSC 4

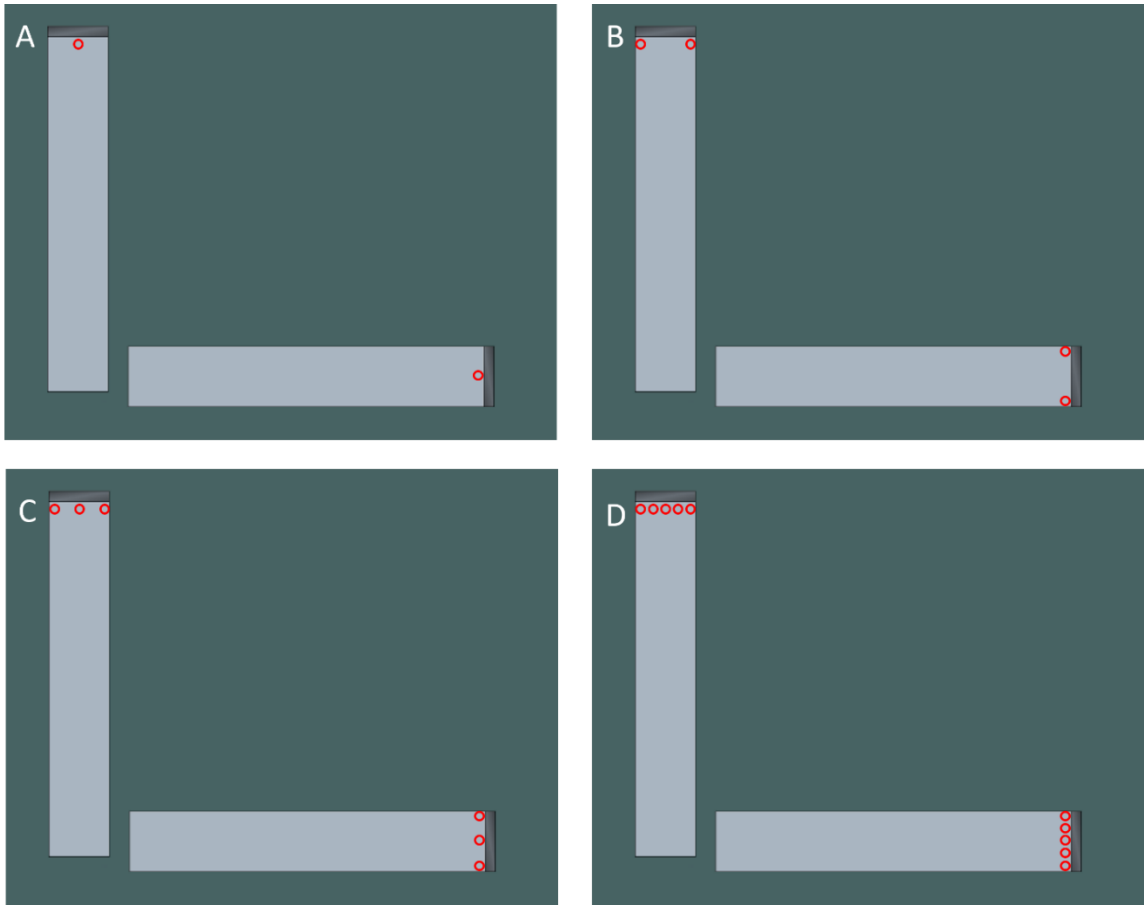

Figure 5-9-Measuring points used in ODC calibration simulations, A-DSC1, B-DCS2, C-DCS3, D-DCS4

The calibration was completed with a voxel mesh size of $0.5mm$ as this mesh size delivers the best calibration results with reasonable computational cost. A summary of die output results delivered from the calibration using OSC can be found in Table 5-6, and for the ODC, the results can be found in Table 5-7. The full results table can be found in Appendix A Table A 3 to Table A 6 for each calibration that contains the percentage deviation between the target deformation and the predicted deformation. As seen in Table 5-6, the Z calibration show little change from the initial prescribed value when using a single cantilever for the calibration process, posing a change $< 1 \times 10^{-7}$. The influence of Z-calibration is much more prominent in the ODC calibration when more than three points of measured distortion are considered. Increasing the Eigenstrain tensor in the Z-direction from the default guess value of -0.03 to -0.045, as seen in Table 5-7.

Table 5-6- OSC Eigen strain tensors calibration results

Single cantilever Orthotropic			
With Z calibration			
	ε_xx	**ε_yy**	**ε_zz**
SCS1	-0,00349197	-0,00135488	-0,03
SCS2	-0,00349197	-0,00135488	-0,03
SCS3	-0,00324916	-0,00144023	-0,0299999
SCS4	-0,00322619	-0,00149092	-0,02999993
Without Z calibration			
	ε_xx	ε_yy	ε_zz
SCS1	-0,00349197	-0,00135488	-0,03
SCS2	-0,00328818	-0,00189753	-0,03
SCS3	-0,00322302	-0,00149946	-0,03
SCS4	-0,003064	-0,00149292	-0,03

Table 5-7-ODC Eigen strain tensors calibration results

Double cantilever Orthotropic			
With Z calibration			
	ε_xx	**ε_yy**	**ε_zz**
DCS1	-0,00335932	-0,000884255	-0,03
DCS2	-0,00339867	-0,000841	-0,03
DCS3	-0,00340009	-0,000835946	-0,0297002
DCS4	-0,00343789	-0,000858798	-0,045229
Without Z calibration			
	ε_xx	**ε_yy**	**ε_zz**
DCS1	-0,00335931	-0,000884266	-0,03
DCS2	-0,00340409	-0,000839175	-0,03
DCS3	-0,0033921	-0,000846774	-0,03
DCS4	-0,00341383	-0,000828814	-0,03

5.4 Validation phase

The result of the calibration completed with the OSC and ODC process is a set of Eigen strain tensors. The resulting Eigen strain tensors must be evaluated in a deformation prediction simulation to select the most accurate configuration. This evaluation is done to investigate the influence of the number of input target deformation points and the influence of the Z-calibration function on the calibration. These configurations and settings were then used in the distortion compensation phase that will alter the geometry of the component. The target deformation was that of the predicted tip deformation of the cantilever that was fabricated at an angle of $45°$ relative to the X and Y-axis of the build plate. During the deformation prediction simulations, the voxel element size for the first assortment of simulations was set to $0.25mm$ and for the second group of simulations set to voxel element size of $0.5mm$. The was done to investigate how the voxel element size influenced the deformation prediction accuracy with the addition of the Z-calibration and multiple target deformation point variables to the simulation.

The configuration that produced the most accurate results during these OSC experiments was the simulation with a 0.25mm voxel mesh and using the Eigen strain values that resulted from the calibration using the average displacement of the cantilever tip. The percentage error between the predicted values and the actual deformation values of each of the points can be found in Table 5-8.

Table 5-8-Configuration of Eigen strain values and voxel mesh with the least amount of error for the single cantilever calibration.

Voxel mesh=0,25mm with Z calibration			
Average			
Z_Target	Z_predicted	Micron difference	Percentage error
11,1228	10,92738	195,417	1,8%
10,86642	10,7951	71,3185	0,7%
10,6589	10,64598	12,919	0,1%
10,44808	10,51956	-71,4845	0,7%
10,21308	10,39637	-183,2925	1,8%

The configuration that produced the most accurate results during the ODC experiments was the simulation with a 0.5mm voxel mesh and using the Eigen strain values that resulted from the calibration using the two most outer displacement points of the cantilever tip. The percentage error between the predicted values and the actual deformation values of each of the points can be found in Table 5-9

Table 5-9-Configuration of Eigen strain values and voxel mesh with the least amount of error for the double cantilever calibration.

Voxel mesh=0,5mm with Z calibration			
2Point			
Z_Target	Z_predicted	Micron difference	Percentage error
11,1228	10,8482	274,597	2,5%
10,86642	10,77079	95,6285	0,9%
10,6589	10,67067	-11,771	0,1%
10,44808	10,57551	-127,435	1,2%
10,21308	10,50691	-293,832	2,9%

The OSC process resulted in more accurate deformation prediction than that of the ODC process. For all the simulation configurations, the OSC had a maximum and minimum point error ranging between 3.6% for the maximum error and 0% for the minimum error. While the ODC process

resulted in a maximum points error of 4.1% and a minimum error of 0%. The maximum OSC error resulted in a deviation of $363.312\ \mu m$ and the ODC maximum error in a deviation of $455.727 \mu m$. Individual deviations and errors of each measuring point of all the OSC simulations can be found in Appendix A Table A 7 to Table A 10 and for the ODC simulation in Table A 11 to Table A 14.

To evaluate the influence of the amount of target deformation points used in the simulation, each configuration of Eigen strain tensor values resulting from the calibration phase was simulated. The simulation was performed with a voxel element size of $0.25mm$ and $0.5mm$ for the OSC process and the ODC process. The simulations were further divided into subsections governed whether the simulation uses Z-calibration or not. The number of target deformation points was altered during each of the simulations. The purpose of this section was simply to evaluate the minimum number of target deformation points needed in the calibration phase to result in accurate deformation prediction results in the simulation phase. Figure 5-10 and Figure 5-11 is a visual representation of the effect of the number of target deformation points used during the calibration, the effect of the voxel element size and the effect of Z-calibration on the deformation prediction accuracy during the simulation.

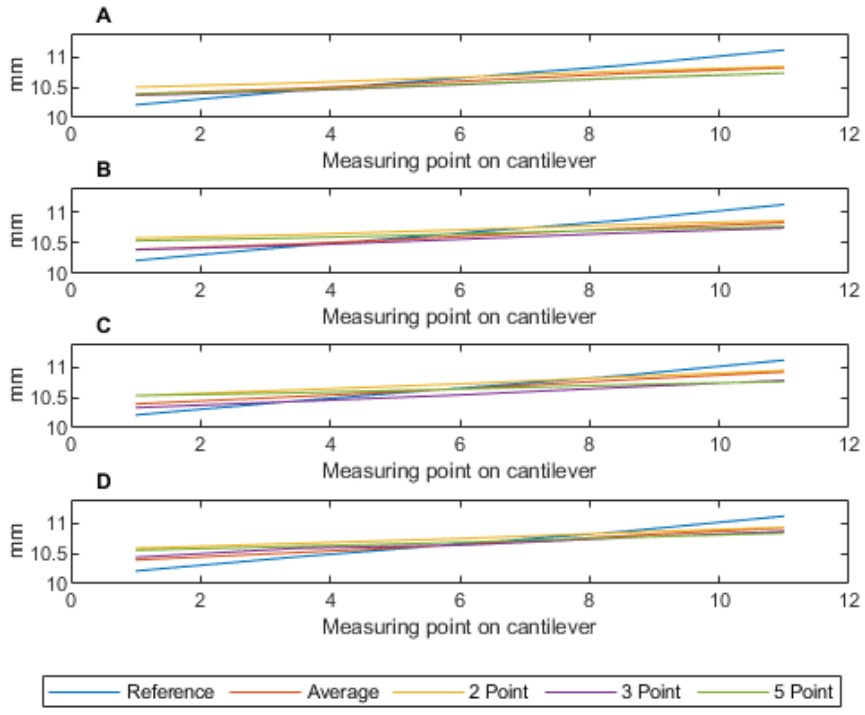

Figure 5-10-Calibration results of OSC-A- voxel mesh=0.5 with Z calibration, B- voxel mesh=0.5 without Z calibration, C- voxel mesh=0.25 with Z calibration, D- voxel mesh=0.25 without Z calibration.

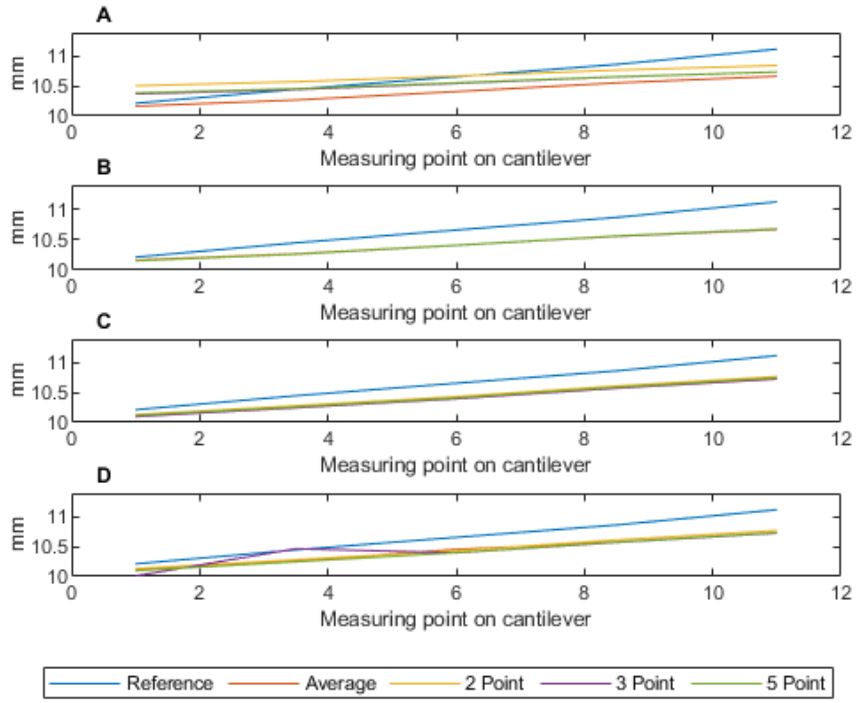

Figure 5-11-Calibration results of ODC-A- voxel mesh=0.5 with Z calibration, B- voxel mesh=0.5 without Z calibration, C- voxel mesh=0.25 with Z calibration, D- voxel mesh=0.25 without Z calibration.

5.5 Distortion compensation phase

The workflow that must be followed to be able to use the deformation compensation method is illustrated in Figure 5-12. The process includes a calibration cycle and a simulation cycle. If the calibration for the machine, feedstock material, and simulation software has already been completed, only the simulation cycle is necessary for this method. The geometry is simulated in the design space of Simufact, and distortion results obtain from the initial simulation. These results are used as an initial reference distortion of the geometry. The boundary condition is set as the minimum distortion goal for the process, and the software alters the initial geometry until the distortion results of the simulation satisfy the boundary conditions.

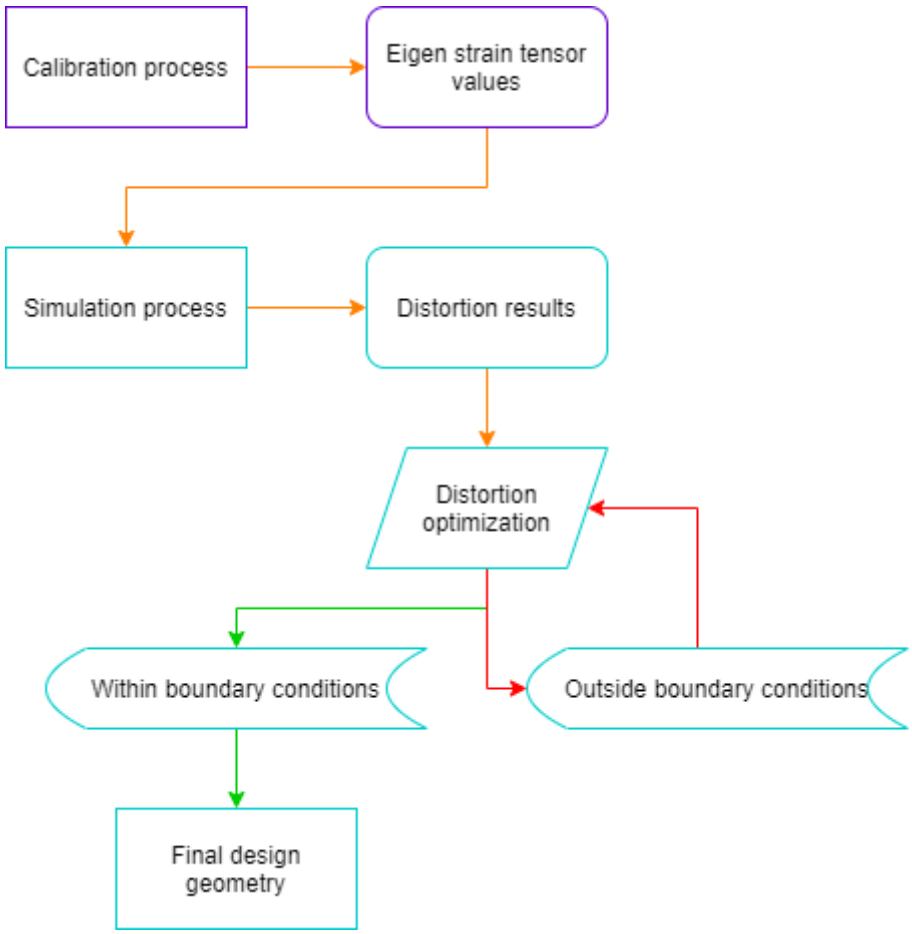

Figure 5-12- Distortion compensation design flow diagram

The simulation results of the initial distortion of the geometry are shown in Figure 5-13 A, and the distortion results of the compensated geometry are in Figure 5-13B. The distortion compensated values display a definite decrease in the overall deformation of the part. The distortion compensated decreased the total maximum distortion of the part from $1.45mm$ to $0.3mm$.

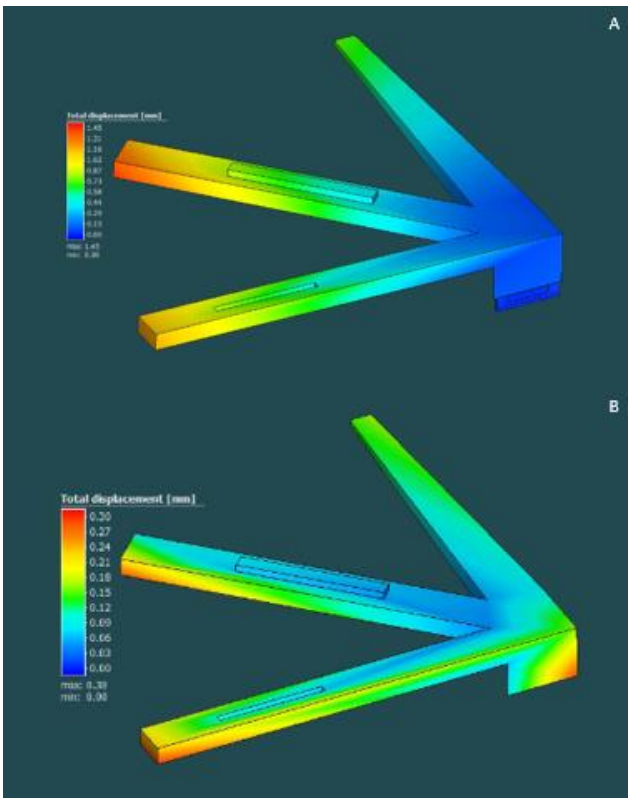

Figure 5-13-A Initial geometry, B- Distortion compensated geometry

The optimisation is achieved as previously explained in Section 4.7.2. The results of the complex geometry distortion compensation optimisation can be seen in Figure 5-14, which depicts the iterative flow and convergence of the process to the initial set values of the optimisation process.

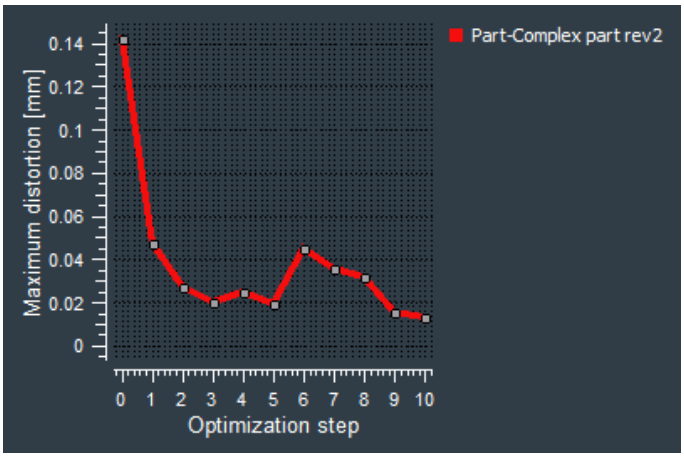

Figure 5-14-Distortion compensation optimisation process

5.5.1 Comparison of simulated deformation results aided by the distortion compensation method

The geometry was divided into three sections for analysis. Each section represents the tip deformation of the X-axis, 45°-axis, and Y-axis extensions. Figure 5-15 illustrates the sections that were analysed as these sections underwent the most deformation during the simulation.

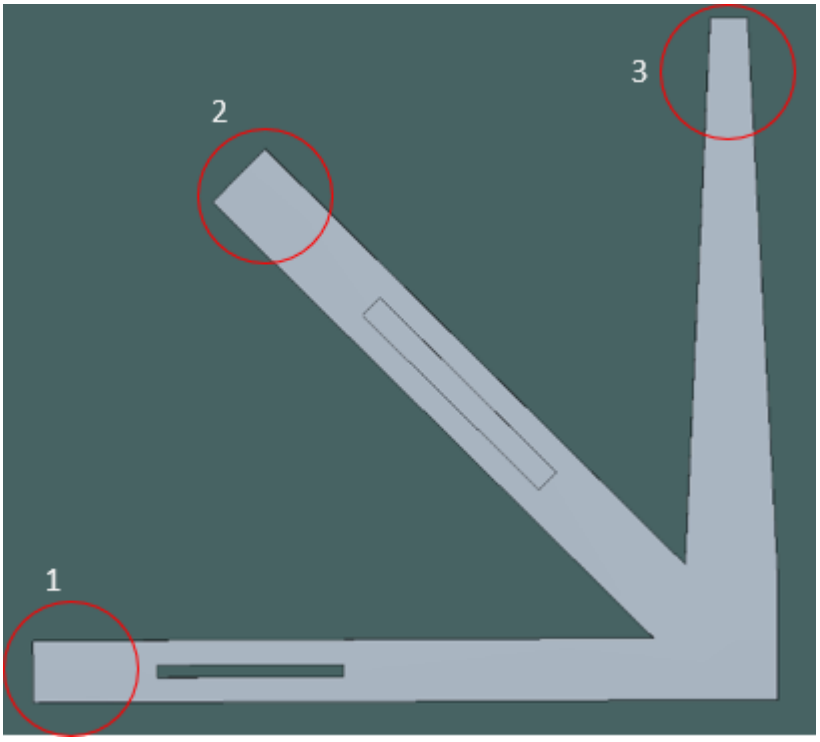

Figure 5-15-Complex geometry tip deformation sectioning, 1- Section 1, 2-Section 2, 3-Section 3

Figure 5-16 to Figure 5-18 show the deformation of each section of the complex geometry component in three stages. Stage one is the original CAD data file where there is no deformation present. Stage two is the non-deformation phase, where the geometry was simulated, and sectioned as-built and stage three is where the geometry has undergone a distortion compensation during the simulation phase and before the fabrication and section phase of the experiment.

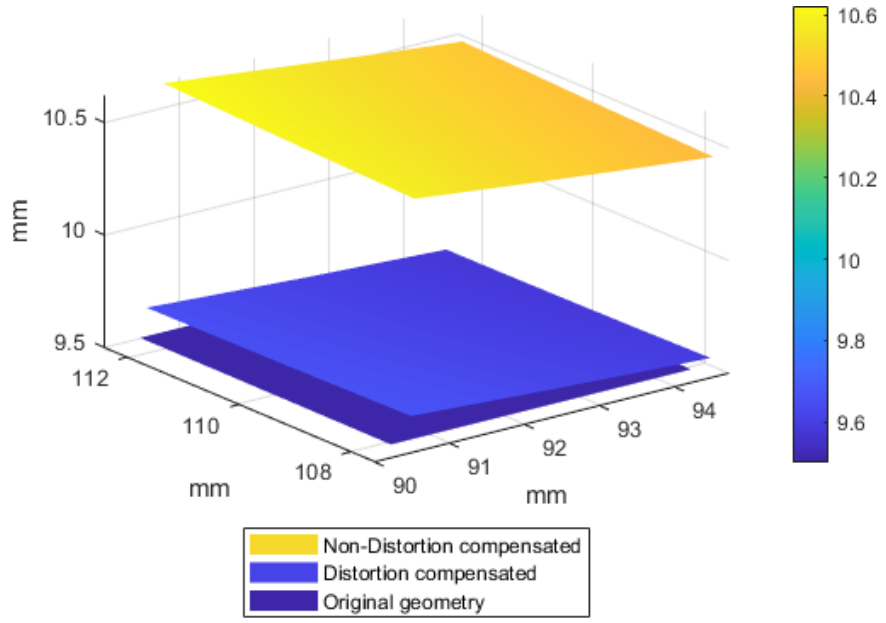

Figure 5-16- Simulated results of the distortion compensation tip deformation results of section 1 on the complex geometry

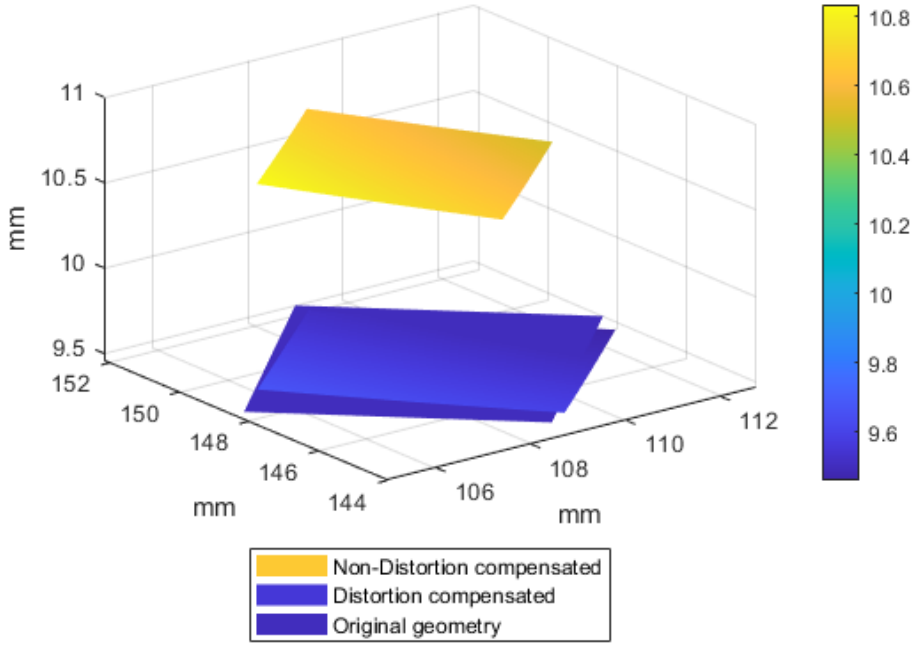

Figure 5-17- Simulated results of the distortion compensation tip deformation results of section 2 on the complex geometry

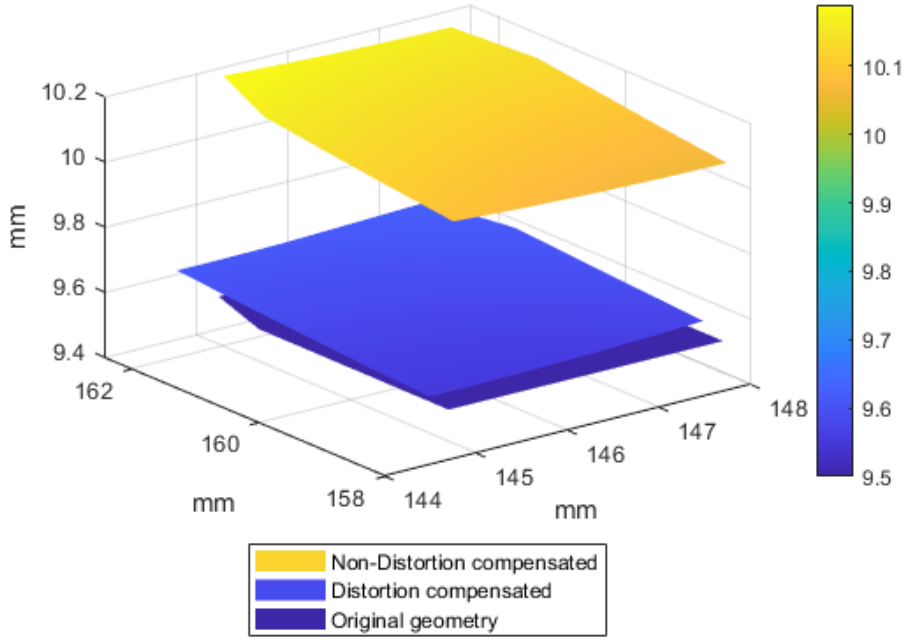

Figure 5-18- Simulated results of the distortion compensation tip deformation results of section 3 on the complex geometry

In each of the sections, the deformation was significantly reduced by altering the geometry of the component. Using the deformation compensation, the maximum tip deformation of section one was reduced by $10.08\ \%$, section two reduced by $12.04\ \%$ and section 3 reduced by 6.04%. The tip deformation values and reductions can be seen in Appendix B Table B 1.

Figure 5-19 to Figure 5-21 is a comparison between the measured or experimental deformation and the simulated deformation. The original CAD data of the complex geometry was also added for a relevant reference point. Figure 5-21 A is a depiction of section 1, B of section 2, and C of section 3. Figure 5-21 A resulted in an average accuracy of 3.3% with a maximum deviation of 5.08% on one of the nodal points under predicting the actual deformation of the section. The point of maximum deviation was in on the outer perimeter of the section. Figure 5-21 B resulted in the least amount of percentage error between the measured deformation values and the predicted deformation values with an average percentage error of $1.64\ \%$ and a maximum deviation of 3.94%. The point of maximum deviation was also on the outer perimeter of the section. Figure 5-21 C had an average percentage error of 2.52% over the tip section with a maximum deviation of 4.06%. Table 5-10 shows the average, maximum, and minimum deviation as a percentage and micron values of each section. The nodal point deviation of each of the sections can be found in Appendix B Table B 2

Table 5-10-Non deformation compensated geometry's deviation and micron difference of predicted distortion and measured distortion

	Section 1	Section 2	Section 3
Average deviation	0,80%	1,63%	2,52%
Max deviation	5,08%	3,94%	4,06%
Min deviation	1,97%	0,13%	0,88%
Max micron difference	563,905	437,8771	397,207
Min micron difference	212,327	14,32173	88,28

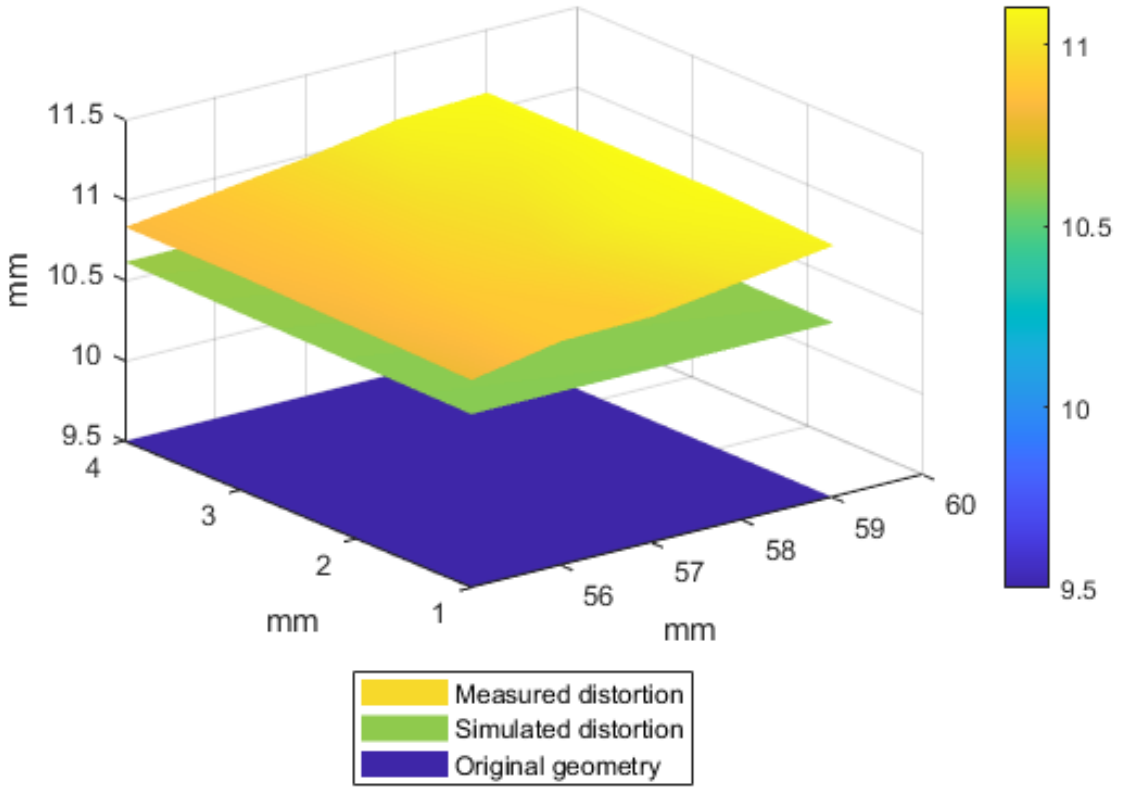

Figure 5-19-Non-distortion compensation tip deformation results of section 1 on the complex geometry

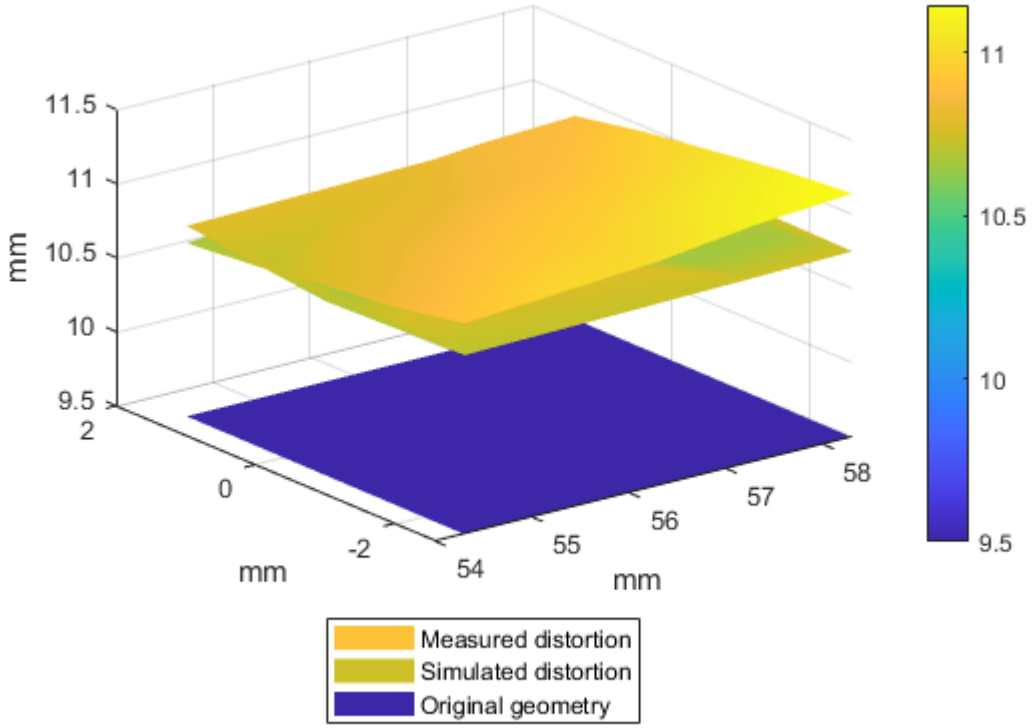

Figure 5-20-Non-distortion compensation tip deformation results of section 2 on the complex geometry

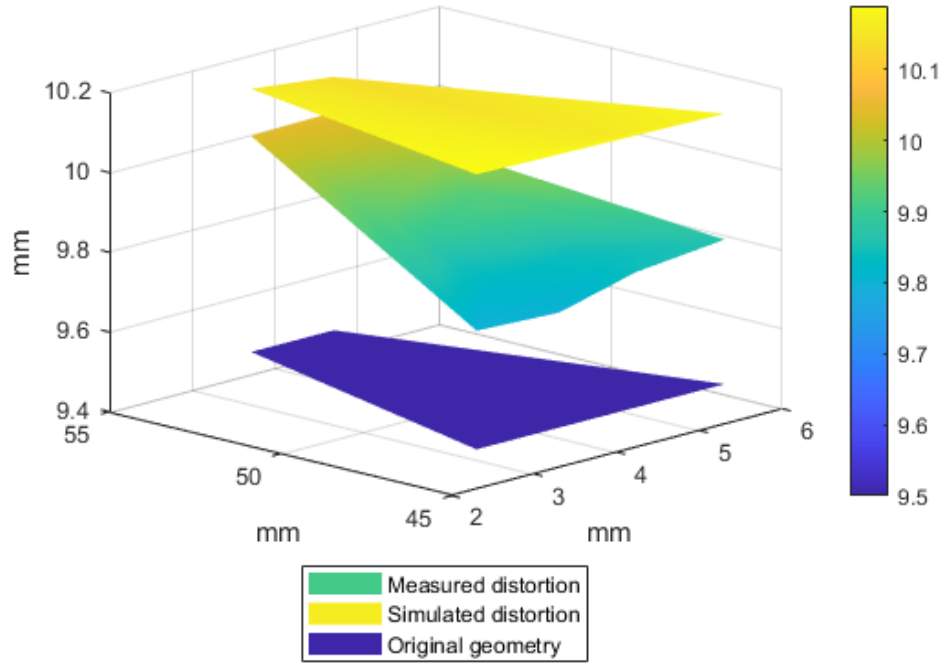

Figure 5-21- Non-distortion compensation tip deformation results of section 3 on the complex geometry

5.5.2 Comparison between measured results and simulated results of the distortion compensated geometry

Figure 5-22 to Figure 5-24 shows each of the sections of the distortion compensated geometry's experimental deformation measurements and the predicted deformation during the simulation phase. The deviation between the predicted distortion and the actual distortion of the geometry was significantly higher than that of the geometry that did not undergo distortion compensation. Even though the deviation in the predicted deformation is higher than the non-distortion compensated geometry, the total distortion of each of the sections was still decreased by a certain margin. This is discussed in section 5.5.3. The average deviation between the predicted deformation values and the experimental values for each of the sections can be found in Table 5-11. The deviation shows a tendency that indicates a direct correlation between the magnitude of compensation and the decrease a distortion prediction accuracy. The reduction in deformation of section one and section two both exceeded a $> 10\ \%$ theoretical decrease in deformation with a deviation in the accuracy of $> 7.2\%$, but section three only underwent a decrease in deformation of $6\ \%$ with an accuracy of 1.21% average deviation. This is due to the initial deformation of each of the sections. As section one and section two both had a more prominent distortion than that of section three, the total compensation needed for section one and section two must be more extensive.

Table 5-11-Deformation compensated geometry's deviation and micron difference of predicted distortion and measured distortion

	Section 1	Section 2	Section 3
Average deviation	9,63%	7,17%	1,21%
Max deviation	10,74%	8,73%	2,22%
Min deviation	8,30%	5,46%	0,16%
Max micron difference	1160,565	916,3982	208,6176
Min micron difference	875,268	554,9616	15,67753

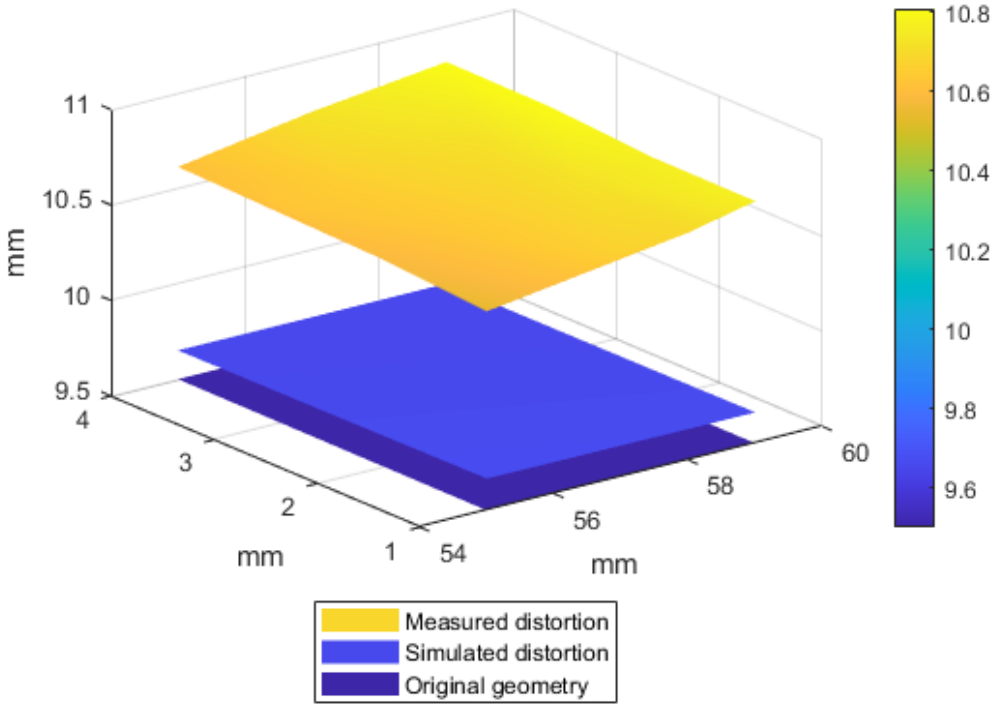

Figure 5-22-Distortion compensation tip deformation results of section 1 on the complex geometry

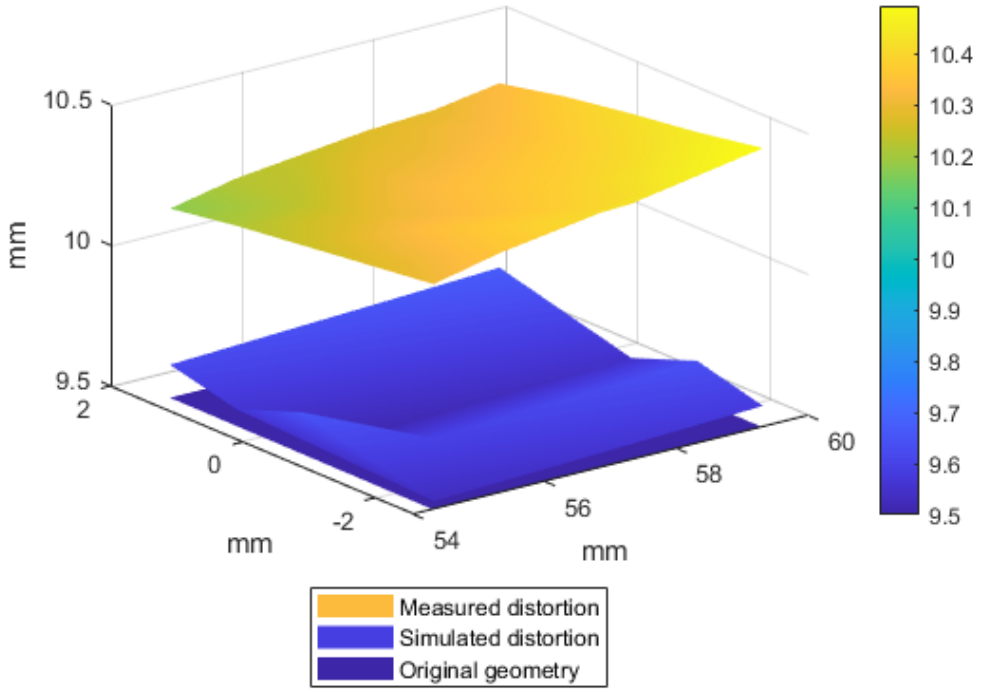

Figure 5-23-Distortion compensation tip deformation results of section 2 on the complex geometry

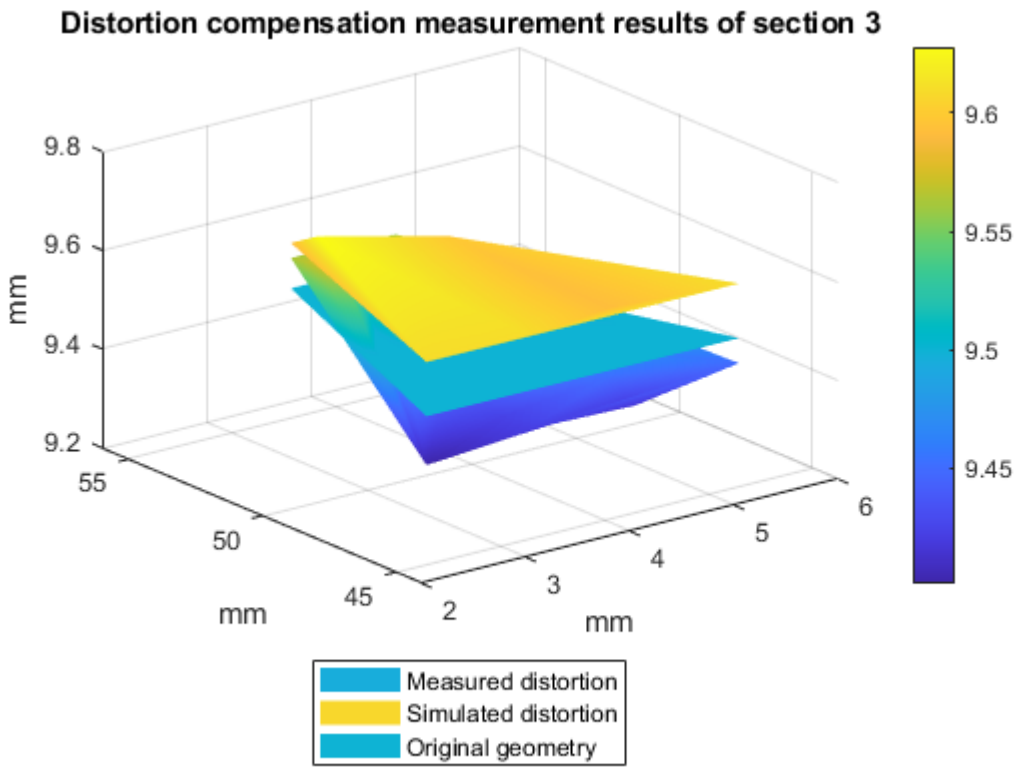

Figure 5-24-Distortion compensation tip deformation results of section 3 on the complex geometry

5.5.3 Distortion compensation results

Figure 5-25 to Figure 5-27 shows the tip deformation of the complex geometry that was subjected to the distortion compensation compared to the tip section of the complex geometry that did not undergo distortion compensation. As shown in the Figures in question, the distortion of each section was decreased through distortion compensation.

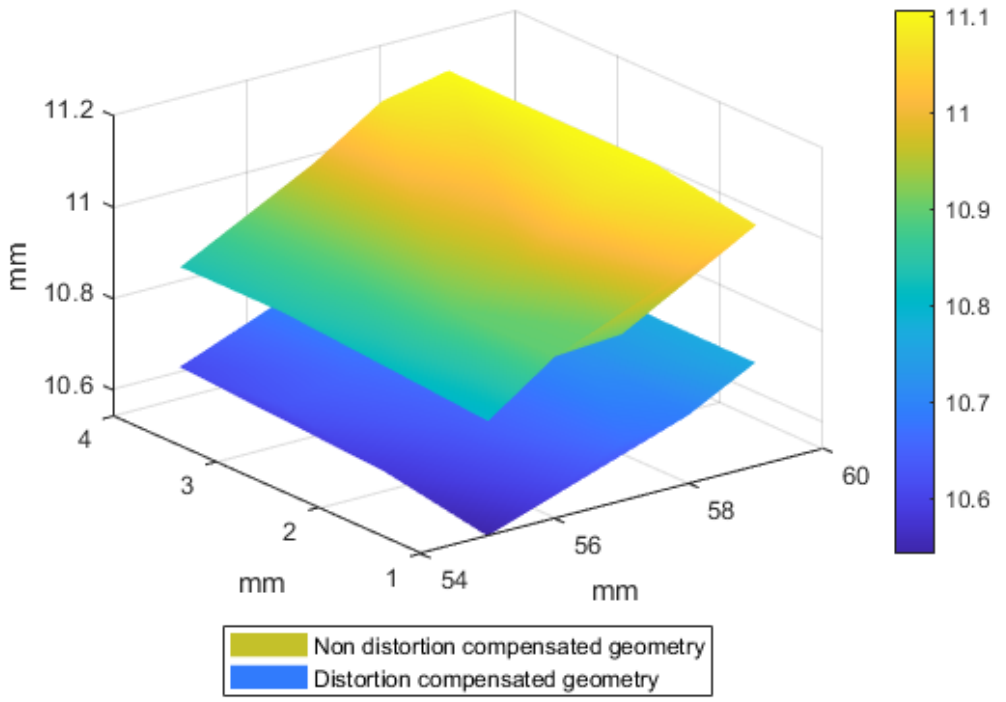

Figure 5-25- Comparison between measured results of the distortion compensated geometry and the non-distortion compensated geometry of section 1

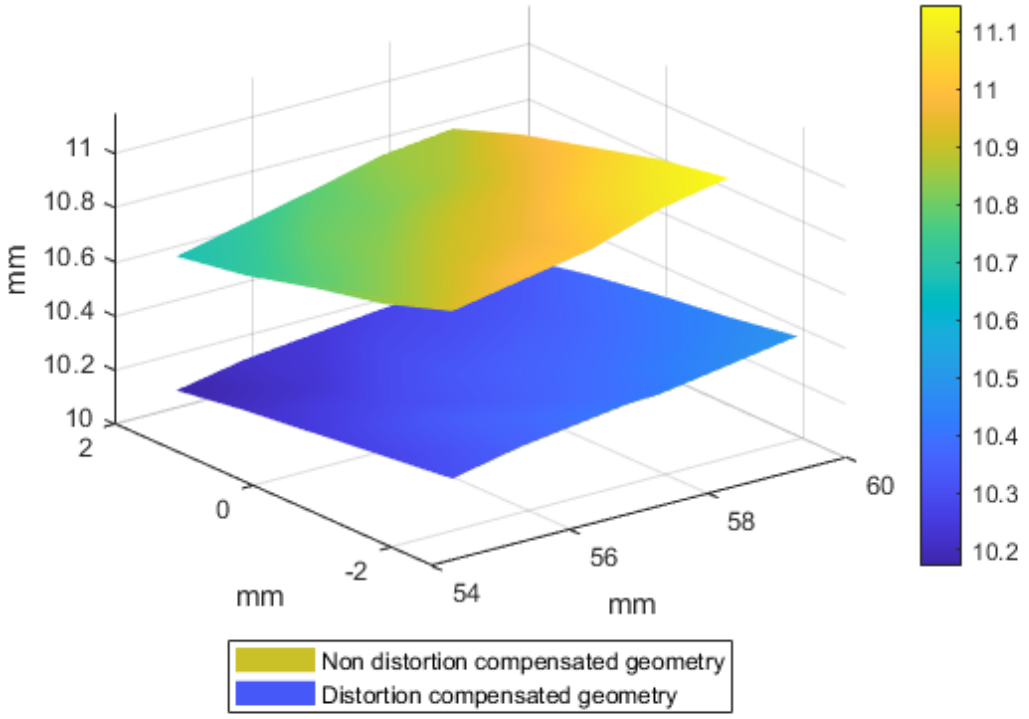

Figure 5-26- Comparison between measured results of the distortion compensated geometry and the non-distortion compensated geometry of section 2

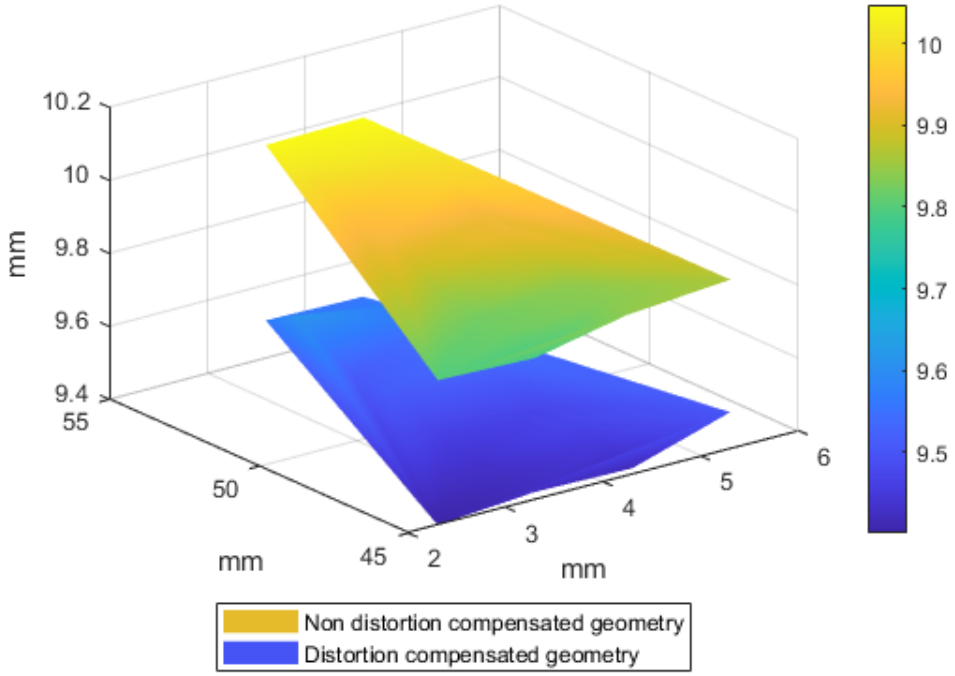

Figure 5-27- Comparison between measured results of the distortion compensated geometry and the non-distortion compensated geometry of section 3

Table 5-12 show the deformation decrease of each section in a percentage value relative to the initial deformation measurements.

Table 5-12- Sectional deformation decrease as a result of using deformation compensation

	Section 1	Section 2	Section 3
Average decrease	2,59%	5,67%	4,35%
Max decrease	3,21%	7,80%	5,14%
Min decrease	1,93%	4,06%	3,83%
Max micron difference	344,152	798,241	491,017
Min micron difference	204,609	422,558	363,595

Section two's theoretical decrease in deformation was estimated at 12.04%, but the actual decrease in deformation was equal to 5.67 %. This value was calculated by measuring the deformation of the complex geometry that did not undergo distortion compensation and

comparing the surface to that of the measured surface of the geometry that did undergo distortion compensation. Table 5-12 shows the decrease of deformation of the individual sections of the geometry. Where the total deformation with respect to the points on the geometry where the maximum deformation will occur was decreased between $1.93\% \; and \; 7.8\%$. This translates to a decrease in deformation of certain areas of over $790 \; \mu m$. The individual nodal point decrease values can be found in Appendix B Table B 3.

Table 5-13 and Table 5-14 shows a summary of the accuracy of the predicted simulated values compared to the actual deformation of the non-distortion compensated geometry and the distortion compensated geometry, respectively.

Table 5-13-Deformation accuracy of the non-distortion compensated geometry

	Section 1	**Section 2**	**Section 3**
Average deviation	0,80%	1,63%	2,52%
Max deviation	5,08%	3,94%	4,06%
Min deviation	1,97%	0,13%	0,88%
Max micron difference	563,905	437,8771	397,207
Min micron difference	212,327	14,32173	88,28

Table 5-14- Deformation accuracy of the distortion compensated geometry

	Section 1	**Section 2**	**Section 3**
Average deviation	9,63%	7,17%	1,21%
Max deviation	10,74%	8,73%	2,22%
Min deviation	8,30%	5,46%	0,16%
Max micron difference	1160,565	916,3982	208,6176
Min micron difference	875,268	554,9616	15,67753

CHAPTER 6

CONCLUSION

6.1 Introduction

As AM is fulfilling a vital role in the manufacturing and prototyping section during industry 4.0, the need arises for the quantification of tolerances and accuracy. Chapter 6 consists of a discussion and conclusion on this study that provides insight into the results and objectives.

6.2 Conclusion

The aim of this study was to investigate the accuracy of the deformation prediction of simulation package, Simufact additive and the viability of the method for distortion compensation for components manufactured with the use of a powder bed fusion SLM additive process.
The objective of this study can be summaries as follows:

- Calibration phase between the simulation software and the OC AM machine.
- The validation phase ensures that the calibration process is successful.
- Distortion compensation phase as investigation of this study.

6.2.1 Calibration phase

To achieve the desired objectives, each of the different phases had to be usefully executed to start with the calibration phase of the experiment. The calibration phase was divided into single and double cantilever calibrations, each with the isotropic and orthotropic calibration process. The isotropic calibration processes of the single and double cantilever experiments were not further investigated as the AM method induces orthotropic properties in the geometry. The fabrication of the cantilevers was completed by manufacturing one cantilever per build plate per manufacturing cycle. The calibration configuration that resulted in the most accurate Eigen strain tensors values was by using a single cantilever beam on a build plate and enabling the orthotropic calibration configuration in Simufact. The number of points used as inputs for the calibration process resulted in using the outermost points on the cantilever for the most accurate calibration.
The scanning pattern will have the most considerable effect on the twist and deformation of the top plane as the scanning pattern determines how the component is heated and cooled and how the thermal energy will interact with previously completed layers.
Another crucial part of the calibration was found to be that of the voxel mesh element size. As shown in section 4.4.6, as the voxel size increases, the accuracy of the calculated Eigen strain tensors values will decrease, leading to a decrease in deformation prediction accuracy. It is thus essential to perform an in-depth mesh independency test before using the calibration process of Simufact.

6.2.2 Validation phase

The validation process entailed predicting the deformation of the cantilever in a mechanical simulation and comparing the predicted values to that of the actual deformation values of the experiment. Each pair of Eigen strain tensor values that resulted from the calibration phase was then used as input parameters in a mechanical simulation in Simufact. The results of the simulation showed that using a minimum of two points and placing the measuring points from the outside boundary inwards will result in accurate deformation predictions. The accuracy of the simulation ranged between $0.1\ \%\ and\ 5\ \%$ depending on the Eigen strain tensor values that were used for the simulation. From the experiments using Eigen strain tensor values of $\epsilon_{xx} = -0.00336585$, $\epsilon_{yy} = -0.00169252$, and $\epsilon_{zz} = -0.03$ will result in adequate deformation prediction of components that are fabricated with CoCr as feedstock material.

6.2.3 Distortion compensation phase

The distortion compensation phase was implemented into the study to investigate the prediction accuracy of Simufact and the achievable decrease in distortion of the component. Without the calibration and validation phases, the distortion compensation phase will not result in any viable outputs. The distortion compensation phase starts by simulating the desired geometry and predicting the deformation. When the simulation has successfully been completed, Simufact used the output data from the simulation to alter the geometry of the component. The software does not change any input parameters such as laser speed, laser intensity, power, layer height, or laser speed. The Eigen strain tensor values used in the initial simulation will also be used in the distortion compensation optimisation cycle. The only variable will be the geometry that is altered during this optimisation. The deformation prediction accuracy of the initial simulation, which was the original geometry that was not subjected to the distortion compensation, was significantly more accurate compared to the deformation prediction of the geometry that was optimized. As the accuracy of the deformation prediction of the distortion compensated geometry was lower than the non-distortion compensated geometry, the total deformation of the geometry was still decreased.

The distortion compensation of SLM specimens shows promise in the field AM. As AM develops to fit the research and industrial needs of the manufacturing technologies, the implementation and utilization of software packages in conjunction with this fabrication technique will become an essential part of the successful manufacturing of components. This study has shown that with the use of competent software, the problems, and limitations, such as deformation arising during SLM fabrication, can be minimized without the need for hardware adjustment. The calibration phase

between the software and the hardware is an essential component to the successful simulation and fabrication of AM parts.

6.3 Future recommendations

From the findings present in this study, the following recommendations should be considered in future research:

- How the type of simulation namely, mechanical simulations, thermal simulations, and thermomechanical simulation will affect the accuracy of the predicted stress and deformation.
- What the influence of the scanning strategy will be on the stress concentration within the boundary of the component during fabrication.
- How the geometry of the support structures can be optimized to decrease the residual stress in the component.
- Investigation of how the position of the sectioning line used to cut the connection points between the calibration cantilever and the build plate will have on the calculated Eigen strain tensor values of the system.

REFERENCES

[1] Q. Wang *et al.*, *Additive manufacturing technologies*, vol. 9, no. 5. 2014.

[2] T. Wohlers and T. Gornet, “History of Additive Manufacturing,” 2016.

[3] S. Singh, S. Ramakrishna, and R. Singh, “Material issues in additive manufacturing: A review,” *J. Manuf. Process.*, vol. 25, pp. 185–200, Jan. 2017, doi: 10.1016/J.JMAPRO.2016.11.006.

[4] H. Bikas, A. K. Lianos, and P. Stavropoulos, “A design framework for additive manufacturing,” *Int. J. Adv. Manuf. Technol. 2019 1039*, vol. 103, no. 9, pp. 3769–3783, May 2019, doi: 10.1007/S00170-019-03627-Z.

[5] R. Ponche, O. Kerbrat, P. Mognol, and J. Y. Hascoet, “A novel methodology of design for Additive Manufacturing applied to Additive Laser Manufacturing process,” *Robot. Comput. Integr. Manuf.*, vol. 30, no. 4, pp. 389–398, Aug. 2014, doi: 10.1016/J.RCIM.2013.12.001.

[6] M. K. Thompson *et al.*, “Design for Additive Manufacturing: Trends, opportunities, considerations, and constraints,” *CIRP Ann.*, vol. 65, no. 2, pp. 737–760, Jan. 2016, doi: 10.1016/J.CIRP.2016.05.004.

[7] A. Wiberg, J. Persson, and J. Ölvander, “Design for additive manufacturing – a review of available design methods and software,” *Rapid Prototyp. J.*, vol. 25, no. 6, pp. 1080–1094, Aug. 2019, doi: 10.1108/RPJ-10-2018-0262.

[8] C. Li, Z. Y. Liu, X. Y. Fang, and Y. B. Guo, “Residual Stress in Metal Additive Manufacturing,” *Procedia CIRP*, vol. 71, pp. 348–353, 2018, doi: 10.1016/j.procir.2018.05.039.

[9] W. E. Frazier, “Metal additive manufacturing: A review,” *J. Mater. Eng. Perform.*, vol. 23, no. 6, pp. 1917–1928, 2014, doi: 10.1007/s11665-014-0958-z.

[10] S. Sun, M. Brandt, and M. Easton, “Powder bed fusion processes: An overview,” *Laser Addit. Manuf. Mater. Des. Technol. Appl.*, pp. 55–77, Jan. 2017, doi: 10.1016/B978-0-08-100433-3.00002-6.

[11] S. Vock, B. Klöden, A. Kirchner, T. Weißgärber, and B. Kieback, “Powders for powder bed fusion: a review,” *Prog. Addit. Manuf.*, vol. 4, no. 4, pp. 383–397, Dec. 2019, doi: 10.1007/S40964-019-00078-6/TABLES/3.

[12] C. Zhu *et al.*, “3D printed functional nanomaterials for electrochemical energy storage,” *Nano Today*, vol. 15. Elsevier B.V., pp. 107–120, Aug. 01, 2017, doi: 10.1016/j.nantod.2017.06.007.

[13] H. Liu, T. Sparks, F. Liou, and D. M. Dietrich, “Residual stress and deformation modelling for metal additive manufacturing processes,” *Proc. World Congr. Mech. Chem. Mater. Eng.*, no. 245, pp. 1–9, 2015.

[14] S. Brinckmann, “A framework for material calibration and deformation predictions applied to additive manufacturing of metals,” *Int. J. Fract.*, vol. 218, no. 1–2, pp. 85–95, Jul. 2019, doi: 10.1007/s10704-019-00375-9.

[15] A. Nassehi, S. Newman, V. Dhokia, Z. Zhu, and R. I. Asrai, “Using formal methods to model hybrid manufacturing processes,” in *Enabling Manufacturing Competitiveness and Economic Sustainability*, Springer Berlin Heidelberg, 2012, pp. 52–56.

[16] K. V. Wong and A. Hernandez, “A Review of Additive Manufacturing,” *ISRN Mech. Eng.*, vol. 2012, pp. 1–10, 2012, doi: 10.5402/2012/208760.

[17] J. Xu, X. Gu, D. Ding, Z. Pan, and K. Chen, “A review of slicing methods for directed energy deposition based additive manufacturing,” *Rapid Prototyp. J.*, vol. 24, no. 6, pp. 1012–1025, 2018, doi: 10.1108/RPJ-10-2017-0196.

[18] Z. Quan *et al.*, “Additive manufacturing of multi-directional preforms for composites: Opportunities and challenges,” *Materials Today*, vol. 18, no. 9. Elsevier, pp. 503–512, Nov. 01, 2015, doi: 10.1016/j.mattod.2015.05.001.

[19] D. Popescu *et al.*, “workflow for additive manufacturing of an individualized surgical template,” *OSF Glob. Serv.*, vol. 10, no. 3, 2015, Accessed: Sep. 20, 2021. [Online]. Available: https://www.researchgate.net/publication/327306483.

[20] S. Rosso, F. Uriati, L. Grigolato, R. Meneghello, G. Concheri, and G. Savio, “An Optimization Workflow in Design for Additive Manufacturing,” *Appl. Sci. 2021, Vol. 11, Page 2572*, vol. 11, no. 6, p. 2572, Mar. 2021, doi: 10.3390/APP11062572.

[21] S. Junk and C. Kuen, “Review of Open Source and Freeware CAD Systems for Use with 3D-Printing,” *Procedia CIRP*, vol. 50, pp. 430–435, Jan. 2016, doi: 10.1016/J.PROCIR.2016.04.174.

[22] M. Pagac *et al.*, “Prediction of Model Distortion by FEM in 3D Printing via the Selective

Laser Melting of Stainless Steel AISI 316L," *Appl. Sci. 2021, Vol. 11, Page 1656*, vol. 11, no. 4, p. 1656, Feb. 2021, doi: 10.3390/APP11041656.

[23] P. Singh and D. Dutta, "Multi-direction slicing for layered manufacturing," *J. Comput. Inf. Sci. Eng.*, vol. 1, no. 2, pp. 129–142, 2001, doi: 10.1115/1.1375816.

[24] Y. Yang, J. Y. H. Fuh, H. T. Loh, and Y. S. Wong, "Multi-orientational deposition to minimize support in the layered manufacturing process," *J. Manuf. Syst.*, vol. 22, no. 2, pp. 116–129, 2003, doi: 10.1016/S0278-6125(03)90009-4.

[25] D. Ding, Z. Pan, D. Cuiuri, H. Li, and S. van Duin, "Advanced Design for Additive Manufacturing: 3D Slicing and 2D Path Planning," *New Trends 3D Print.*, pp. 3–24, 2016, doi: 10.5772/63042.

[26] O. A. Mohamed, S. H. Masood, and J. L. Bhowmik, "Optimization of fused deposition modeling process parameters: a review of current research and future prospects," *Adv. Manuf.*, vol. 3, no. 1, pp. 42–53, 2015, doi: 10.1007/s40436-014-0097-7.

[27] B. Esmaeilian, S. Behdad, and B. Wang, "The evolution and future of manufacturing: A review," *J. Manuf. Syst.*, vol. 39, no. April, pp. 79–100, 2016, doi: 10.1016/j.jmsy.2016.03.001.

[28] F. P. W. Melchels, J. Feijen, and D. W. Grijpma, "A review on stereolithography and its applications in biomedical engineering," *Biomaterials*, vol. 31, no. 24. Elsevier, pp. 6121–6130, Aug. 01, 2010, doi: 10.1016/j.biomaterials.2010.04.050.

[29] G. B. Kim *et al.*, "Three-dimensional printing: Basic principles and applications in medicine and radiology," *Korean J. Radiol.*, vol. 17, no. 2, pp. 182–197, Mar. 2016, doi: 10.3348/KJR.2016.17.2.182.

[30] V. Bhavar, P. Kattire, V. Patil, S. Khot, K. Gujar, and R. Singh, "A review on powder bed fusion technology of metal additive manufacturing," *Addit. Manuf. Handb. Prod. Dev. Def. Ind.*, no. September, pp. 251–261, 2017, doi: 10.1201/9781315119106.

[31] S. L. Sing, J. An, W. Y. Yeong, and F. E. Wiria, "Laser and electron-beam powder-bed additive manufacturing of metallic implants: A review on processes, materials and designs," *J. Orthop. Res.*, vol. 34, no. 3, pp. 369–385, 2016, doi: 10.1002/jor.23075.

[32] C. L. A. Leung, S. Marussi, R. C. Atwood, M. Towrie, P. J. Withers, and P. D. Lee, "In situ X-ray imaging of defect and molten pool dynamics in laser additive manufacturing," *Nat.*

Commun., vol. 9, no. 1, pp. 1–9, Dec. 2018, doi: 10.1038/s41467-018-03734-7.

[33] A. Bhargav, V. Sanjairaj, V. Rosa, L. W. Feng, and J. Fuh YH, “Applications of additive manufacturing in dentistry: A review,” *J. Biomed. Mater. Res. - Part B Appl. Biomater.*, vol. 106, no. 5, pp. 2058–2064, 2018, doi: 10.1002/jbm.b.33961.

[34] C. Y. Yap *et al.*, “Review of selective laser melting: Materials and applications,” *Appl. Phys. Rev.*, vol. 2, no. 4, 2015, doi: 10.1063/1.4935926.

[35] I. Yadroitsev, P. Krakhmalev, and I. Yadroitsava, “Selective laser melting of Ti6Al4V alloy for biomedical applications: Temperature monitoring and microstructural evolution,” *J. Alloys Compd.*, vol. 583, pp. 404–409, Jan. 2014, doi: 10.1016/j.jallcom.2013.08.183.

[36] A. Razavykia, E. Brusa, C. Delprete, and R. Yavari, “An overview of additive manufacturing technologies-A review to technical synthesis in numerical study of selective laser melting,” *Materials (Basel).*, vol. 13, no. 17, 2020, doi: 10.3390/ma13173895.

[37] J. Deckers, J. Vleugels, and J.-P. Kruth, “Title Additive Manufacturing of Ceramics: A Review Author names and affiliations Jan Deckers*,” *Addit. Manuf. Ceram. A Rev. Author*, pp. 1–51, 2014.

[38] “Residual Stress | Definition of Residual Stress by Oxford Dictionary on Lexico.com also meaning of Residual Stress.” https://www.lexico.com/definition/residual_stress (accessed Jul. 28, 2020).

[39] D. Dutta *et al.*, “The Theory of moving sources of heat and its application to metal tretments,” *J. Mater. Process. Technol.*, vol. 68, no. 11–12, pp. 849–69, 2012, doi: 10.1007/s00170-007-1181-y.

[40] J. D. Lord and A. T. Fry, “A review of residual stress measurement methods-a guide to technical selection Metrosion View project Steam Oxidation View project,” 2001. Accessed: Jul. 17, 2020. [Online]. Available: https://www.researchgate.net/publication/236860729.

[41] O. Fergani, F. Berto, T. Welo, and S. Y. Liang, “Analytical modelling of residual stress in additive manufacturing,” *Fatigue Fract. Eng. Mater. Struct.*, vol. 40, no. 6, pp. 971–978, 2017, doi: 10.1111/ffe.12560.

[42] M. Megahed, H.-W. Mindt, N. N’Dri, H. Duan, and O. Desmaison, *Metal additive-manufacturing process and residual stress modeling*, vol. 5, no. 1. Integrating Materials and Manufacturing Innovation, 2016.

[43] Z. C. Fang, Z. L. Wu, C. G. Huang, and C. W. Wu, “Review on residual stress in selective laser melting additive manufacturing of alloy parts,” *Opt. Laser Technol.*, vol. 129, p. 106283, Sep. 2020, doi: 10.1016/J.OPTLASTEC.2020.106283.

[44] C. Li, J. F. Liu, and Y. B. Guo, “Prediction of Residual Stress and Part Distortion in Selective Laser Melting,” *Procedia CIRP*, vol. 45, pp. 171–174, Jan. 2016, doi: 10.1016/J.PROCIR.2016.02.058.

[45] C. A. Brice and W. H. Hofmeister, “Determination of bulk residual stresses in electron beam additive-manufactured aluminum,” *Metall. Mater. Trans. A Phys. Metall. Mater. Sci.*, vol. 44, no. 11, pp. 5147–5153, Nov. 2013, doi: 10.1007/s11661-013-1847-z.

[46] D. Morgan, E. Agba, and C. Hill, “Support Structure Development and Initial Results for Metal Powder Bed Fusion Additive Manufacturing,” *Procedia Manuf.*, vol. 10, pp. 819–830, Jan. 2017, doi: 10.1016/j.promfg.2017.07.083.

[47] R. Vaidya and S. Anand, “Optimum Support Structure Generation for Additive Manufacturing Using Unit Cell Structures and Support Removal Constraint,” *Procedia Manuf.*, vol. 5, pp. 1043–1059, Jan. 2016, doi: 10.1016/j.promfg.2016.08.072.

[48] J. P. Järvinen *et al.*, “Characterization of effect of support structures in laser additive manufacturing of stainless steel,” in *Physics Procedia*, Jan. 2014, vol. 56, no. C, pp. 72–81, doi: 10.1016/j.phpro.2014.08.099.

[49] J. Jiang, X. Xu, and J. Stringer, “Support Structures for Additive Manufacturing: A Review,” *J. Manuf. Mater. Process.*, vol. 2, no. 4, p. 64, 2018, doi: 10.3390/jmmp2040064.

[50] C. Teng *et al.*, “Simulating melt pool shape and lack of fusion porosity for selective laser melting of cobalt chromium components,” *J. Manuf. Sci. Eng. Trans. ASME*, vol. 139, no. 1, 2017, doi: 10.1115/1.4034137.

[51] P. Hanzl, M. Zetek, T. Bakša, and T. Kroupa, “The Influence of Processing Parameters on the Mechanical Properties of SLM Parts,” *Procedia Eng.*, vol. 100, no. January, pp. 1405–1413, Jan. 2015, doi: 10.1016/J.PROENG.2015.01.510.

[52] E. Louvis, P. Fox, and C. J. Sutcliffe, “Selective laser melting of aluminium components,” *J. Mater. Process. Technol.*, vol. 211, no. 2, pp. 275–284, Feb. 2011, doi: 10.1016/j.jmatprotec.2010.09.019.

[53] J. A. Slotwinski, E. J. Garboczi, P. E. Stutzman, C. F. Ferraris, S. S. Watson, and M. A.

Peltz, “Characterization of metal powders used for additive manufacturing,” *J. Res. Natl. Inst. Stand. Technol.*, vol. 119, pp. 460–493, 2014, doi: 10.6028/jres.119.018.

[54] Y. S. Al Jabbari, “Physico-mechanical properties and prosthodontic applications of Co-Cr dental alloys: A review of the literature,” *J. Adv. Prosthodont.*, vol. 6, no. 2, pp. 138–145, 2014, doi: 10.4047/jap.2014.6.2.138.

[55] “Introduction to Metal 3D printing | 3D Hubs.” https://www.3dhubs.com/knowledge-base/introduction-metal-3d-printing/ (accessed Jan. 29, 2020).

[56] A. Tasaka *et al.*, “Accuracy of removable partial denture framework fabricated by casting with a 3D printed pattern and selective laser sintering,” *J. Prosthodont. Res.*, Aug. 2019, doi: 10.1016/j.jpor.2019.07.009.

[57] T. Mayer, G. Brändle, A. Schönenberger, and R. Eberlein, “Simulation and validation of residual deformations in additive manufacturing of metal parts,” *Heliyon*, vol. 6, no. 5, p. e03987, May 2020, doi: 10.1016/J.HELIYON.2020.E03987.

[58] a. çelebi and e. z. appavuravther, “Analyzing the Effect of Voxel Mesh and Surface Mesh Application on Residual Stress by Simufact Additive Software,” *Duzce Univ. J. Sci. Technol.*, vol. 6, no. 4, pp. 930–940, Aug. 2018, doi: 10.29130/DUBITED.426063.

[59] M. S. Company, *Simufact_additive_Tutorial_en*. 2020.

[60] N. Ma *et al.*, “Inherent Strain Method for Residual Stress Measurement and Welding Distortion Prediction,” no. June, 2016, doi: 10.1115/omae2016-54184.

[61] X. Liang, Q. Chen, L. Cheng, Q. Yang, and A. To, “A modified inherent strain method for fast prediction of residual deformation in additive manufacturing of metal parts,” 2017.

[62] A. Ueda, Y. Chul, and M. Gang, “Title A Predicting Method of Welding Residual Stress Using Source of Residual Stress (Report I) : Characteristics of Inherent Strain (Source of Residual Stress)(Mechanics, Strength & Structural Design),” 1989. Accessed: May 11, 2021. [Online]. Available: https://ir.library.osaka-u.ac.jp/.

[63] A. M. Korsunsky, “The Journal of Strain Analysis for Engineering Design Residual elastic strain due to laser shock peening : modelling by eigenstrain distribution,” 2006, doi: 10.1243/03093247JSA141.

[64] T. Mura, “Mechanics of Elastic and Inelastic Solids,” vol. 3, pp. 324–387, 1982, doi: 10.1007/978-94-009-3489-4_6.

[65] T. S. Jun and A. M. Korsunsky, “Evaluation of residual stresses and strains using the Eigenstrain Reconstruction Method,” *Int. J. Solids Struct.*, vol. 47, no. 13, pp. 1678–1686, 2010, doi: 10.1016/j.ijsolstr.2010.03.002.

[66] J. Fish and T. Belytschko, “A First Course in Finite Elements,” *A First Course Finite Elem.*, pp. 1–319, 2007, doi: 10.1002/9780470510858.

[67] J. N. Reddy, *Introduction to the Finite Element Method, Third Edition*, 3rd editio. New York: McGraw-Hill Education, 2006.

[68] X. He, “Finite element analysis of laser welding: A state of art review,” *Materials and Manufacturing Processes*, vol. 27, no. 12. Taylor & Francis Group , pp. 1354–1365, Dec. 01, 2012, doi: 10.1080/10426914.2012.709345.

[69] M. Simeonnkeates, “Springer Tracts in Mechanical Engineering Finite Element Applications A Practical Guide to the FEM Process,” Accessed: Nov. 04, 2021. [Online]. Available: http://www.springer.

[70] K. Ravichandran, “Calibrating Inherent Strain for Additive Manufacturing An investigation of different subscale geometries.”

[71] X. Liang, Q. Chen, L. Cheng, D. Hayduke, and A. C. To, “Modified inherent strain method for efficient prediction of residual deformation in direct metal laser sintered components,” *Comput. Mech.*, vol. 64, no. 6, pp. 1719–1733, Dec. 2019, doi: 10.1007/s00466-019-01748-6.

[72] L. L. Hikmah, N. Almardhiyyah, N. A. Muzakki, N. A. Rahmi K, Q. Zannah, and W. R. Adawiyah, “ORLAS CREATOR DATA SHEET,” 2016. doi: 10.1017/CBO9781107415324.004.

[73] E. J. Garboczi and N. Hrabe, “Particle shape and size analysis for metal powders used for additive manufacturing: Technique description and application to two gas-atomized and plasma-atomized Ti64 powders,” *Addit. Manuf.*, vol. 31, Jan. 2020, doi: 10.1016/J.ADDMA.2019.100965.

[74] “Morphology and properties of CoCrMo parts fabricated by selective laser melting | Elsevier Enhanced Reader.” https://reader.elsevier.com/reader/sd/pii/S0921509317316337?token=0EB36575FCD35030A228AA84BE869788034765650E35F3EE2D4F23881BA36C26AE5DBA6D5B373EFAEF9A226F29C4F946&originRegion=eu-west-1&originCreation=20210831141146

(accessed Aug. 31, 2021).

[75] L. Hitzler *et al.*, “Additive manufacturing of cobalt-based dental alloys: Analysis of microstructure and physicomechanical properties,” *Adv. Mater. Sci. Eng.*, vol. 2018, 2018, doi: 10.1155/2018/8213023.

[76] S. Kurosu, H. Matsumoto, and A. Chiba, “Grain refinement of biomedical Co-27Cr-5Mo-0.16N alloy by reverse transformation,” *Mater. Lett.*, vol. 64, no. 1, pp. 49–52, Jan. 2010, doi: 10.1016/J.MATLET.2009.10.001.

[77] A. Metel, M. Stebulyanin, S. Fedorov, and A. Okunkova, “Power Density Distribution for Laser Additive Manufacturing (SLM): Potential, Fundamentals and Advanced Applications,” *Technologies*, vol. 7, no. 1, p. 5, Dec. 2018, doi: 10.3390/technologies7010005.

[78] H. Metrology, “Dea global silver.” Hexagon Metrology, pp. 8–15.

[79] A. Dutt, “Effect of Mesh Size on Finite Element Analysis of Beam,” *Int. J. Mech. Eng.*, vol. 2, no. 12, pp. 8–10, 2015, doi: 10.14445/23488360/ijme-v2i12p102.

[80] P. Bian, J. Shi, Y. Liu, and Y. Xie, “Influence of laser power and scanning strategy on residual stress distribution in additively manufactured 316L steel,” *Opt. Laser Technol.*, vol. 132, p. 106477, Dec. 2020, doi: 10.1016/J.OPTLASTEC.2020.106477.

[81] S. Ueng, H. Huang, and Z. Liu, “Image-based Contouring and G-code Generation for Additive Manufacturing Image-based Contouring and G-code Generation for Additive Manufacturing,” no. March, 2019.

APPENDICES

Table A 1 shows the calibration setup and results, such as the Eigen strain tensor values resulting from the different voxel meshes used during the calibration

Table A 1-Mesh independency results.

Voxel Mesh Size	1	0,9	0,8	0,7	0,6	0,5	0,4
Voxel mesh volume	1	0,729	0,512	0,343	0,216	0,125	0,064
Voxels	5532	10010	14460	20952	29640	44208	95700
Nodal points	9399	13260	18752	27379	40278	59125	119164
Estimation value	-0,03	-0,03	-0,03	-0,03	-0,03	-0,03	-0,03
	-0,00135	-0,00135	-0,00135	-0,00135	-0,00135	-0,00135	-0,00135
	-0,00302	-0,00302	-0,00302	-0,00302	-0,00302	-0,00302	-0,00302
Calibration result	-0,0299999	-0,0300000	-0,0300000	-0,0300000	-0,0299990	-0,0300000	-0,2970000
	-0,00169252	-0,00203583	-0,00185179	-0,00045890	-0,00174194	-0,00144023	-0,00139665
	-0,00336586	-0,00492592	-0,00439723	-0,00484350	-0,00343980	-0,00324916	-0,00312985
Error in predicted deformation and target	0,726932	0,27331	2,95308	0,945759	0,730461	0,745116	1,71215
	0,76731	1,77786	1,49778	0,54358	0,763433	2,2616	0,232708
	Point 2	Point 1					

0,875947	0,64494	-0,00347061	-0,00088592	-0,0299988	-0,00302	-0,00135	-0,03	261990	220760	0,027	0,3
0,11737	1,98276	-0,00352828	-0,00082866	-0,0300000	-0,00302	-0,00135	-0,03	781471	690300	0,015625	0,25

Table A 2-Influence of voxel mesh on deformation prediction

ε_xx	ε_yy	ε_zz
-0,00336586	-0,00169252	-0,0299999

Build plate average VM-1			
1			
Z Target	Z predicted	Micron difference	Percentage error
10,2130775	9,414214	798,8635	7,8%
10,4480755	9,447067	1001,0085	9,6%
10,658899	9,496741	1162,158	10,9%
10,8664185	9,555534	1310,8845	12,1%
11,122797	9,610991	1511,806	13,6%

ε_xx	ε_yy	ε_zz
-0,00324916	-0,00144023	-0,0300000

Build plate average VM-0,5			
1			
Z Target	Z predicted	Micron difference	Percentage error
10,2130775	9,371557	841,5205	8,2%
10,4480755	9,407999	1040,0765	10,0%
10,658899	9,4616905	1197,2085	11,2%
10,8664185	9,524162	1342,2565	12,4%
11,122797	9,582181	1540,616	13,9%

ε_xx	ε_yy	ε_zz	
-0,00378311	-0,00151926	-0,0300000	
Build plate average VM-0,25			
1			
Z Target	Z predicted	Micron difference	Percentage error
10,2130775	9,42272	790,3575	7,7%
10,4480755	9,468784	979,2915	9,4%
10,658899	9,535845	1123,054	10,5%
10,8664185	9,613102	1253,3165	11,5%
11,122797	9,684265	1438,532	12,9%

The Eigen strain values that were used in each of the simulations indicated by $\epsilon_{xx}, \epsilon_{yy}, and\ \epsilon_{zz}$.

Table A 3- OSC with Z calibration Eigen strain results

Single cantilever Orthotropic			
With Z calibration			
SCS1			
ε_xx	ε_yy	ε_zz	Delta Max (%)
-0,00349197	-0,00135488	-0,03	0,0694444
SCS2			
ε_xx	ε_yy	ε_zz	Delta Max (%)
-0,03365850	-0,00169252	-0,0299999	0,76731
			0,726932
SCS3			
ε_xx	ε_yy	ε_zz	Delta Max (%)
-0,00324916	-0,00144023	-0,0299999	2,26157
			0,745107
			2,17573
SCS4			
ε_xx	ε_yy	ε_zz	Delta Max (%)
-0,00322619	-0,00149092	-0,02999993	2,10834
			0,59412
			2,01436

			1,65881
			0,961746

The $\Delta Max\ \%$ value indicates the difference between the calibrated nodal point measurement and the nodal reference measurement

Table A 4-OSC without Z calibration Eigen strain results

Single cantilever Orthotropic		
Without Z calibration		
SCS1		
ε_xx	ε_yy	Delta Max (%)
-0,00349197	-0,00135488	0,0694445
SCS2		
ε_xx	ε_yy	Delta Max (%)
-0,00328818	-0,00189753	0,700035
		0,793145
SCS3		
ε_xx	ε_yy	Delta Max (%)
-0,00322302	-0,00149946	1,02371
		2,49097
		1,12416
SCS4		
ε_xx	ε_yy	Delta Max (%)
-0,003064	-0,0019292	1,86359
		0,353295
		1,7006
		1,36565
		0,670746

The $\Delta Max\ \%$ value indicates the difference between the calibrated nodal point measurement and the nodal reference measurement

Table A 5-ODC with Z calibration Eigen strain results

Double cantilever Orthotropic
With Z calibration
DCS1

ε_xx	ε_yy	ε_zz	Delta Max (%)
-0,00335932	-0,000884255	-0,03	0,768941
			0,438274
DCS2			
ε_xx	ε_yy	ε_zz	
-0,00339867	-0,000841	-0,03	0,632794
			0,860953
			2,53046
			2,57366
DCS3			
ε_xx	ε_yy	ε_zz	
-0,00340009	-0,000835946	-0,0297002	0,637251
			0,642777
			0,856568
			2,32589
			0,388922
			2,76802
DCS4			
ε_xx	ε_yy	ε_zz	
-0,00343789	-0,000858798	-0,045229	0,603322
			0,226826
			0,603928
			0,460771
			889941
			2,98095
			2,11808
			0,242354
			2,84211
			2,14568

Table A 6-ODC without Z calibration Eigen strain results

Double cantilever Orthotropic
Without Z calibration

DCS1		
ε_xx	ε_yy	Delta Max (%)
-0,00335931	-0,000884266	0,768928
		0,438292
DCS2		
ε_xx	ε_yy	Delta Max (%)
-0,00340409	-0,000839175	0,774394
		0,721469
		2,54244
		2,56224
DCS3		
ε_xx	ε_yy	Delta Max (%)
-0,0033921	-0,000846774	0,496855
		0,500495
		0,994864
		2,69148
		0,0273184
		2,42069
DCS4		
ε_xx	ε_yy	Delta Max (%)
-0,00341383	-0,000828814	0,957867
		0,584867
		0,964899
		0,105493
		0,540762
		2,21155
		1,35757
		0,505382
		3,56528
		2,8766

Tip deformation prediction of single cantilever calibration.

Table A 7- Single cantilever calibration predicted tip deformation (Voxel mesh-0.5mm with Z calibration)

Voxel mesh=0,5mm with Z calibration			
Average			
Z Target	Z predicted	Micron difference	Percentage error
11,1228	10,82861	294,187	2,6%
10,86642	10,73126	135,1585	1,2%
10,6589	10,60436	54,539	0,5%
10,44808	10,48228	-34,2045	0,3%
10,21308	10,39355	-180,472	1,8%

Voxel mesh=0,5mm with Z calibration			
2Point			
Z Target	Z predicted	Micron difference	Percentage error
11,1228	10,8482	274,597	2,5%
10,86642	10,77079	95,6285	0,9%
10,6589	10,67067	-11,771	0,1%
10,44808	10,57551	-127,435	1,2%
10,21308	10,50691	-293,832	2,9%

Voxel mesh=0,5mm with Z calibration			
3Point			
Z Target	Z predicted	Micron difference	Percentage error
11,1228	10,73896	383,837	3,5%
10,86642	10,656	210,4185	1,9%
10,6589	10,54814	110,759	1,0%
10,44808	10,44493	3,1455	0,0%
10,21308	10,37015	-157,073	1,5%

Voxel mesh=0,5mm with Z calibration
5Point

Z Target	Z predicted	Micron difference	Percentage error
11,1228	10,74007	382,727	3,4%
10,86642	10,66028	206,1385	1,9%
10,6589	10,55669	102,209	1,0%
10,44808	10,45775	-9,6745	0,1%
10,21308	10,38618	-173,102	1,7%

Table A 8-Single cantilever calibration predicted tip deformation (Voxel mesh-0.5mm without Z calibration)

Voxel mesh=0,5mm without Z calibration			
Average			
Z Target	Z predicted	Micron difference	Percentage error
11,1228	10,82681	295,987	2,7%
10,86642	10,73126	135,1585	1,2%
10,6589	10,60436	54,539	0,5%
10,44808	10,48228	-34,2045	0,3%
10,21308	10,39355	-180,472	1,8%

Voxel mesh=0,5mm without Z calibration			
2Point			
Z Target	Z predicted	Micron difference	Percentage error
11,1228	10,86022	262,577	2,4%
10,86642	10,79502	71,3985	0,7%
10,6589	10,71129	-52,391	0,5%
10,44808	10,63262	-184,544	1,8%
10,21308	10,57639	-363,312	3,6%

Voxel mesh=0,5mm without Z calibration
3Point

Z Target	Z predicted	Micron difference	Percentage error
11,1228	10,74057	382,227	3,4%
10,86642	10,66128	205,1385	1,9%
10,6589	10,55837	100,529	0,9%
10,44808	10,46011	-12,0345	0,1%
10,21308	10,38905	-175,972	1,7%

Voxel mesh=0,5mm without Z calibration			
5Point			
Z Target	Z predicted	Micron difference	Percentage error
11,1228	10,76701	355,787	3,2%
10,86642	10,71314	153,2785	1,4%
10,6589	10,64436	14,539	0,1%
10,44808	10,58046	-132,385	1,3%
10,21308	10,53514	-322,062	3,2%

Table A 9-Single cantilever calibration predicted tip deformation (Voxel mesh-0.25mm with Z calibration)

Voxel mesh=0,25mm with Z calibration			
Average			
Z Target	Z predicted	Micron difference	Percentage error
11,1228	10,92738	195,417	1,8%
10,86642	10,7951	71,3185	0,7%
10,6589	10,64598	12,919	0,1%
10,44808	10,51956	-71,4845	0,7%
10,21308	10,39637	-183,2925	1,8%

Voxel mesh=0,25mm with Z calibration
2Point

Z Target	Z predicted	Micron difference	Percentage error
11,1228	10,95133	171,467	1,5%
10,86642	10,84638	20,0385	0,2%
10,6589	10,72872	-69,821	0,7%
10,44808	10,62986	-181,7845	1,7%
10,21308	10,534	-320,9225	3,1%

Voxel mesh=0,25mm with Z calibration			
3Point			
Z Target	Z predicted	Micron difference	Percentage error
11,1228	10,78559	337,207	3,0%
10,86642	10,6728	193,6185	1,8%
10,6589	10,5459	112,999	1,1%
10,44808	10,43872	9,3555	0,1%
10,21308	10,33447	-121,3925	1,2%

Voxel mesh=0,25mm with Z calibration			
5Point			
Z Target	Z predicted	Micron difference	Percentage error
11,1228	10,76701	355,787	3,2%
10,86642	10,71314	153,2785	1,4%
10,6589	10,64436	14,539	0,1%
10,44808	10,58046	-132,3845	1,3%
10,21308	10,53514	-322,0625	3,2%

Table A 10-Single cantilever calibration predicted tip deformation (Voxel mesh-0.25mm without Z calibration)

Voxel mesh=0,25mm without Z calibration			
Average			
Z Target	Z predicted	Micron difference	Percentage error
11,1228	10,92738	195,417	1,8%
10,86642	10,7951	71,3185	0,7%
10,6589	10,64598	12,919	0,1%
10,44808	10,51956	-71,4845	0,7%
10,21308	10,39637	-183,292	1,8%

Voxel mesh=0,25mm without Z calibration			
2Point			
Z Target	Z predicted	Micron difference	Percentage error
11,1228	10,93783	184,967	1,7%
10,86642	10,84973	16,6885	0,2%
10,6589	10,75147	-92,571	0,9%
10,44808	10,66964	-221,564	2,1%
10,21308	10,59073	-377,653	3,7%

Voxel mesh=0,25mm without Z calibration			
3Point			
Z Target	Z predicted	Micron difference	Percentage error
11,1228	10,87018	252,617	2,3%
10,86642	10,76234	104,0785	1,0%
10,6589	10,64115	17,749	0,2%
10,44808	10,5897	-141,625	1,4%
10,21308	10,43968	-226,602	2,2%

Voxel mesh=0,25mm without Z calibration
5Point

Z Target	Z predicted	Micron difference	Percentage error
11,1228	10,8413	281,497	2,5%
10,86642	10,76858	97,8385	0,9%
10,6589	10,68769	-28,787	0,3%
10,44808	10,62124	-173,165	1,7%
10,21308	10,55732	-344,243	3,4%

Table A 11-Double cantilever calibration predicted tip deformation (Voxel mesh-0.5mm with Z calibration)

Voxel mesh=0,5mm with Z calibration			
Average			
Z_Target	Z_predicted	Micron difference	Percentage error
11,1228	10,66707	455,727	4,1%
10,86642	10,55564	310,7785	2,9%
10,6589	10,40953	249,369	2,3%
10,44808	10,26788	180,1955	1,7%
10,21308	10,16442	48,6575	0,5%

Voxel mesh=0,5mm with Z calibration			
2Point			
Z_Target	Z_predicted	Micron difference	Percentage error
11,1228	10,8482	274,597	2,5%
10,86642	10,77079	95,6285	0,9%
10,6589	10,67067	-11,771	0,1%
10,44808	10,57551	-127,435	1,2%
10,21308	10,50691	-293,832	2,9%

Voxel mesh=0,5mm with Z calibration
3Point

Z_Target	Z_predicted	Micron difference	Percentage error
11,1228	10,73896	383,837	3,5%
10,86642	10,656	210,4185	1,9%
10,6589	10,54814	110,759	1,0%
10,44808	10,44493	3,1455	0,0%
10,21308	10,37015	-157,073	1,5%

Voxel mesh=0,5mm with Z calibration			
5Point			
Z_Target	Z_predicted	Micron difference	Percentage error
11,1228	10,74007	382,727	3,4%
10,86642	10,66028	206,1385	1,9%
10,6589	10,55669	102,209	1,0%
10,44808	10,45775	-9,6745	0,1%
10,21308	10,38618	-173,102	1,7%

Table A 12-Double cantilever calibration predicted tip deformation (Voxel mesh-0.5mm without Z calibration)

Voxel mesh=0,5mm without Z calibration			
Average			
Z_Target	Z_predicted	Micron difference	Percentage error
11,1228	10,66707	455,727	4,1%
10,86642	10,55564	310,7785	2,9%
10,6589	10,40953	249,369	2,3%
10,44808	10,26788	180,1955	1,7%
10,21308	10,16442	48,6575	0,5%

Voxel mesh=0,5mm without Z calibration
2Point

Z_Target	Z_predicted	Micron difference	Percentage error
11,1228	10,67531	447,487	4,0%
10,86642	10,56033	306,0885	2,8%
10,6589	10,40949	249,409	2,3%
10,44808	10,26315	184,9255	1,8%
10,21308	10,15622	56,8575	0,6%

Voxel mesh=0,5mm without Z calibration			
3Point			
Z_Target	Z_predicted	Micron difference	Percentage error
11,1228	10,67298	449,817	4,0%
10,86642	10,5578	308,6185	2,8%
10,6589	10,40671	252,189	2,4%
10,44808	10,26007	188,0055	1,8%
10,21308	10,15292	60,1575	0,6%

Voxel mesh=0,5mm without Z calibration			
5Point			
Z_Target	Z_predicted	Micron difference	Percentage error
11,1228	10,6774	445,397	4,0%
10,86642	10,56131	305,1085	2,8%
10,6589	10,40902	249,879	2,3%
10,44808	10,2612	186,8755	1,8%
10,21308	10,15318	59,8975	0,6%

Table A 13-Double cantilever calibration predicted tip deformation (Voxel mesh-0.25mm with Z calibration)

Voxel mesh=0,25mm with Z calibration			
Average			
Z_Target	Z_predicted	Micron difference	Percentage error
11,1228	10,72813	394,667	3,5%
10,86642	10,57504	291,3785	2,7%
10,6589	10,4017	257,199	2,4%
10,44808	10,2541	193,9755	1,9%
10,21308	10,10993	103,1475	1,0%

Voxel mesh=0,25mm with Z calibration			
2Point			
Z_Target	Z_predicted	Micron difference	Percentage error
11,1228	10,76985	352,947	3,2%
10,86642	10,61164	254,7785	2,3%
10,6589	10,43256	226,339	2,1%
10,44808	10,27979	168,2855	1,6%
10,21308	10,13063	82,4475	0,8%

Voxel mesh=0,25mm with Z calibration			
3Point			
Z_Target	Z_predicted	Micron difference	Percentage error
11,1228	10,7317	391,097	3,5%
10,86642	10,57481	291,6085	2,7%
10,6589	10,39722	261,679	2,5%
10,44808	10,24568	202,3955	1,9%
10,21308	10,09768	115,3975	1,1%

Voxel mesh=0,25mm with Z calibration
5Point

Z_Target	Z_predicted	Micron difference	Percentage error
11,1228	10,74814	374,657	3,4%
10,86642	10,59039	276,0285	2,5%
10,6589	10,41186	247,039	2,3%
10,44808	10,25956	188,5155	1,8%
10,21308	10,11083	102,2475	1,0%

Table A 14-Double cantilever calibration predicted tip deformation (Voxel mesh-0.25mm without Z calibration)

Voxel mesh=0,25mm without Z calibration			
Average			
Z_Target	Z_predicted	Micron difference	Percentage error
11,1228	10,73197	390,827	3,5%
10,86642	10,57887	287,5485	2,6%
10,6589	10,4562	202,699	1,9%
10,44808	10,2579	190,1755	1,8%
10,21308	10,11371	99,3675	1,0%

Voxel mesh=0,25mm without Z calibration			
2Point			
Z_Target	Z_predicted	Micron difference	Percentage error
11,1228	10,77319	349,607	3,1%
10,86642	10,6145	251,9185	2,3%
10,6589	10,43488	224,019	2,1%
10,44808	10,28163	166,4455	1,6%
10,21308	10,13202	81,0575	0,8%

Voxel mesh=0,25mm without Z calibration
3Point

Z_Target	Z_predicted	Micron difference	Percentage error
11,1228	10,7293	393,497	3,5%
10,86642	10,57352	292,8985	2,7%
10,6589	10,39718	261,719	2,5%
10,44808	10,4672	-19,1245	0,2%
10,21308	10,09979	113,2875	1,1%

Voxel mesh=0,25mm without Z calibration			
5Point			
Z_Target	Z_predicted	Micron difference	Percentage error
11,1228	10,73782	384,977	3,5%
10,86642	10,57966	286,7585	2,6%
10,6589	10,4006	258,299	2,4%
10,44808	10,2478	200,2755	1,9%
10,21308	10,09857	114,5075	1,1%

Appendix B compromises the nodal point data of each section of the complex geometry that has undergone distortion compensation, and that has not undergone distortion compensation.

Table B 1 shows each sections tip deformation of the complex geometry. Z_{nonDC} shows the total tip deformation of the geometry that did not undergo distortion compensation and Z_{DC} shows the total deformation of geometries tip that did undergo the deformation compensation phase. The deformation values in Table B 1 were obtained through simulated calculation. The percentage difference shows the magnitude of deformation decrease as a percentage value.

Table B 1- Tip deformation of non-deformation compensated geometry and deformation compensated geometry. Z Non-DC-tip deformation of non-distortion compensated geometry, Z_DC tip deformation of distortion compensated geometry

Section 1 Tip deformation			
Z Non-DC	Z_DC	Micron difference	% Difference
10,5816	9,66705	914,55	9,46%
10,5832	9,66551	917,69	9,49%
10,5849	9,6642	920,7	9,53%
10,5868	9,66293	923,87	9,56%
10,5886	9,6617	926,9	9,59%
10,5906	9,66056	930,04	9,63%
10,5926	9,65942	933,18	9,66%
10,5946	9,65831	936,29	9,69%
10,5967	9,6572	939,5	9,73%
10,5989	9,65615	942,75	9,76%
10,6012	9,65519	946,01	9,80%
10,6036	9,65428	949,32	9,83%
10,606	9,65342	952,58	9,87%
10,6085	9,65261	955,89	9,90%
10,611	9,65183	959,17	9,94%
10,6136	9,65109	962,51	9,97%
10,6163	9,65039	965,91	10,01%
10,619	9,64974	969,26	10,04%
10,6218	9,64915	972,65	10,08%

Section 2 Tip deformation			
Z_Non-DC	Z_DC	Micron difference	% Difference
10,83457	9,670224	1164,349905	12,04%
10,82172	9,659183	1162,531958	12,04%
10,80923	9,648568	1160,663609	12,03%
10,79687	9,638056	1158,814751	12,02%
10,78461	9,627653	1156,958727	12,02%
10,77249	9,617354	1155,135128	12,01%
10,76055	9,607197	1153,352034	12,01%
10,74882	9,597217	1151,602918	12,00%
10,73734	9,587446	1149,891742	11,99%
10,72611	9,577899	1148,206374	11,99%
10,71514	9,56858	1146,555544	11,98%
10,70441	9,55951	1144,901465	11,98%
10,69391	9,548018	1145,893695	12,00%
10,6836	9,539349	1144,248391	12,00%
10,67342	9,530766	1142,651718	11,99%
10,66335	9,522473	1140,874871	11,98%
10,65353	9,514071	1139,454053	11,98%
Section 3 Tip deformation			
Z_Non-DC	Z_DC	Micron difference	% Difference
10,1899	9,609629	580,2713531	6,04%
10,1857	9,609486	576,2135259	6,00%
10,1819	9,609885	572,0146012	5,95%
10,1784	9,610582	567,8177183	5,91%
10,1753	9,61158	563,7197349	5,87%
10,1726	9,61293	559,6695714	5,82%
10,1702	9,614645	555,5548269	5,78%
10,1682	9,616719	551,4810777	5,73%
10,1665	9,61912	547,3803219	5,69%
10,1651	9,621789	543,3111484	5,65%

10,164	9,624716	539,2835195	5,60%

Table B 2 shows a nodal comparison of the geometry that did not undergo distortion compensation. The percentage error illustrates the magnitude of error between the measured values resulting from the experiment and the predicted values resulting from the simulations.

Table B 2-Nodal comparison of measured deformation and predicted deformation of non-distortion compensated geometry. Z_M- tip deformation of measured distortion, Z_P- tip deformation of predicted distortion.

Section 1			
Z_M	Z_P	Micron Difference	Percentage error
10,793927	10,5816	212,327	1,97%
10,896867	10,5832	313,667	2,88%
10,907186	10,5849	322,286	2,95%
11,01462	10,5868	427,82	3,88%
11,06892	10,5886	480,32	4,34%
10,813081	10,5906	222,481	2,06%
10,898819	10,5926	306,219	2,81%
10,959568	10,5946	364,968	3,33%
11,063908	10,5967	467,208	4,22%
11,104553	10,5989	505,653	4,55%
10,831357	10,6012	230,157	2,12%
10,894298	10,6036	290,698	2,67%
10,979903	10,606	373,903	3,41%
11,036494	10,6085	427,994	3,88%
11,104081	10,611	493,081	4,44%
10,830607	10,6136	217,007	2,00%
10,895772	10,6163	279,472	2,56%
10,98154	10,619	362,54	3,30%
11,077259	10,6218	455,459	4,11%
11,106205	10,5423	563,905	5,08%
Section 2			
Z_M	Z_P	Micron Difference	Percentage error

10,87235	10,83457	37,77353	0,35%
10,84342	10,82172	21,70571	0,20%
10,78191	10,80923	27,31835	0,25%
10,71754	10,79687	79,33259	0,74%
10,66844	10,78461	116,171	1,09%
10,96445	10,77249	191,9554	1,75%
10,87214	10,76055	111,5871	1,03%
10,82023	10,74882	71,41066	0,66%
10,79555	10,73734	58,21026	0,54%
10,71178	10,72611	14,32173	0,13%
11,02913	10,71514	313,9941	2,85%
10,95084	10,70441	246,4265	2,25%
10,90385	10,69391	209,9404	1,93%
10,83449	10,6836	150,8943	1,39%
10,77881	10,67342	105,3952	0,98%
11,10123	10,66335	437,8771	3,94%
11,04409	10,65353	390,5655	3,54%
10,95626	10,79244	163,8237	1,50%
10,91222	10,77979	132,4329	1,21%
10,83429	10,76751	66,78046	0,62%
11,14594	10,75537	390,5716	3,50%
11,09696	10,74335	353,6076	3,19%
11,01469	10,73147	283,2207	2,57%
10,99254	10,71978	272,7582	2,48%
10,92191	10,70831	213,601	1,96%
Section 2			
Z_M	Z_P	Micron Difference	Percentage error
9,797659	10,1899	392,241	4,00%
9,788493	10,1857	397,207	4,06%
9,843401	10,1819	338,499	3,44%
9,86261	10,1784	315,79	3,20%
9,818976	10,1753	356,324	3,63%
9,822331	10,1726	350,269	3,57%

9,850467	10,1702	319,733	3,25%
9,889636	10,1682	278,564	2,82%
9,93393	10,1665	232,57	2,34%
9,945987	10,1651	219,113	2,20%
9,977746	10,164	186,254	1,87%
10,01711	10,1648	147,689	1,47%
10,04217	10,1602	118,034	1,18%
9,835717	10,1562	320,483	3,26%
9,84166	10,1524	310,74	3,16%
9,8869	10,1489	262	2,65%
9,921152	10,1458	224,648	2,26%
9,92678	10,1431	216,32	2,18%
9,981519	10,1407	159,181	1,59%
10,00333	10,1387	135,375	1,35%
10,02639	10,137	110,61	1,10%
10,04732	10,1356	88,28	0,88%

Table B 3- Deformation decrease of each section of the complex geometry. Z_DC is the displacement of the geometry that was subjected to distortion compensation, and Z_NDC is the displacements of the geometry that was not subjected to distortion compensation

Section 1			
Z_DC	Z_NDC	Micron Difference	Percentage error
10,542318	10,79393	251,609	2,39%
10,602317	10,89687	294,55	2,78%
10,666762	10,90719	240,424	2,25%
10,691047	11,01462	323,573	3,03%
10,767367	11,06892	301,553	2,80%
10,582569	10,81308	230,512	2,18%
10,632451	10,89882	266,368	2,51%
10,671323	10,95957	288,245	2,70%
10,719756	11,06391	344,152	3,21%
10,768476	11,10455	336,077	3,12%

10,626748	10,83136	204,609	1,93%
10,656028	10,8943	238,27	2,24%
10,6914	10,9799	288,503	2,70%
10,71968	11,03649	316,814	2,96%
10,805474	11,10408	298,607	2,76%
10,611439	10,83061	219,168	2,07%
10,661954	10,89577	233,818	2,19%
10,725287	10,98154	256,253	2,39%
10,761734	11,07726	315,525	2,93%
10,809445	11,10621	296,76	2,75%
Section 2			
Z_DC	Z_NDC	Micron Difference	Percentage error
10,32557	10,87235	546,781	5,30%
10,2879	10,84342	555,519	5,40%
10,27468	10,78191	507,231	4,94%
10,23908	10,71754	478,462	4,67%
10,22057	10,66844	447,867	4,38%
10,17232	10,96445	792,129	7,79%
10,37726	10,87214	494,881	4,77%
10,32852	10,82023	491,712	4,76%
10,30195	10,79555	493,603	4,79%
10,28868	10,71178	423,1	4,11%
10,23089	11,02913	798,241	7,80%
10,21156	10,95084	739,275	7,24%
10,41643	10,90385	487,424	4,68%
10,37141	10,83449	463,078	4,46%
10,34836	10,77881	430,451	4,16%
10,32779	11,10123	773,434	7,49%
10,28654	11,04409	757,55	7,36%
10,2494	10,95626	706,869	6,90%
10,45013	10,91222	462,091	4,42%
10,41173	10,83429	422,558	4,06%

10,38112	11,14594	764,823	7,37%
10,34838	11,09696	748,574	7,23%
10,3414	11,01469	673,292	6,51%
10,27454	10,99254	718,001	6,99%
10,49297	10,92191	428,941	4,09%
Section 3			
Z_DC	Z_NDC	Micron Difference	Percentage error
9,401011	9,797659	396,648	4,22%
9,421283	9,788493	367,21	3,90%
9,415938	9,843401	427,463	4,54%
9,499015	9,86261	363,595	3,83%
9,423644	9,818976	395,332	4,20%
9,437259	9,822331	385,072	4,08%
9,455991	9,850467	394,476	4,17%
9,4886	9,889636	401,036	4,23%
9,512559	9,93393	421,371	4,43%
9,508622	9,945987	437,365	4,60%
9,56216	9,977746	415,586	4,35%
9,612203	10,01711	404,908	4,21%
9,561594	10,04217	480,572	5,03%
9,45227	9,835717	383,447	4,06%
9,474734	9,84166	366,926	3,87%
9,475415	9,8869	411,485	4,34%
9,506772	9,921152	414,38	4,36%
9,539657	9,92678	387,123	4,06%
9,550025	9,981519	431,494	4,52%
9,553763	10,00333	449,562	4,71%
9,569655	10,02639	456,735	4,77%
9,556303	10,04732	491,017	5,14%